

On the mechanics and stability of micro-plates in electrically loaded MEMS devices

Sajadi, Banafsheh

DOI

[10.4233/uuid:7ec08141-8ea9-4a7e-923c-b01d9a367b47](https://doi.org/10.4233/uuid:7ec08141-8ea9-4a7e-923c-b01d9a367b47)

Publication date

2017

Document Version

Final published version

Citation (APA)

Sajadi, B. (2017). *On the mechanics and stability of micro-plates in electrically loaded MEMS devices*. [Dissertation (TU Delft), Delft University of Technology]. <https://doi.org/10.4233/uuid:7ec08141-8ea9-4a7e-923c-b01d9a367b47>

Important note

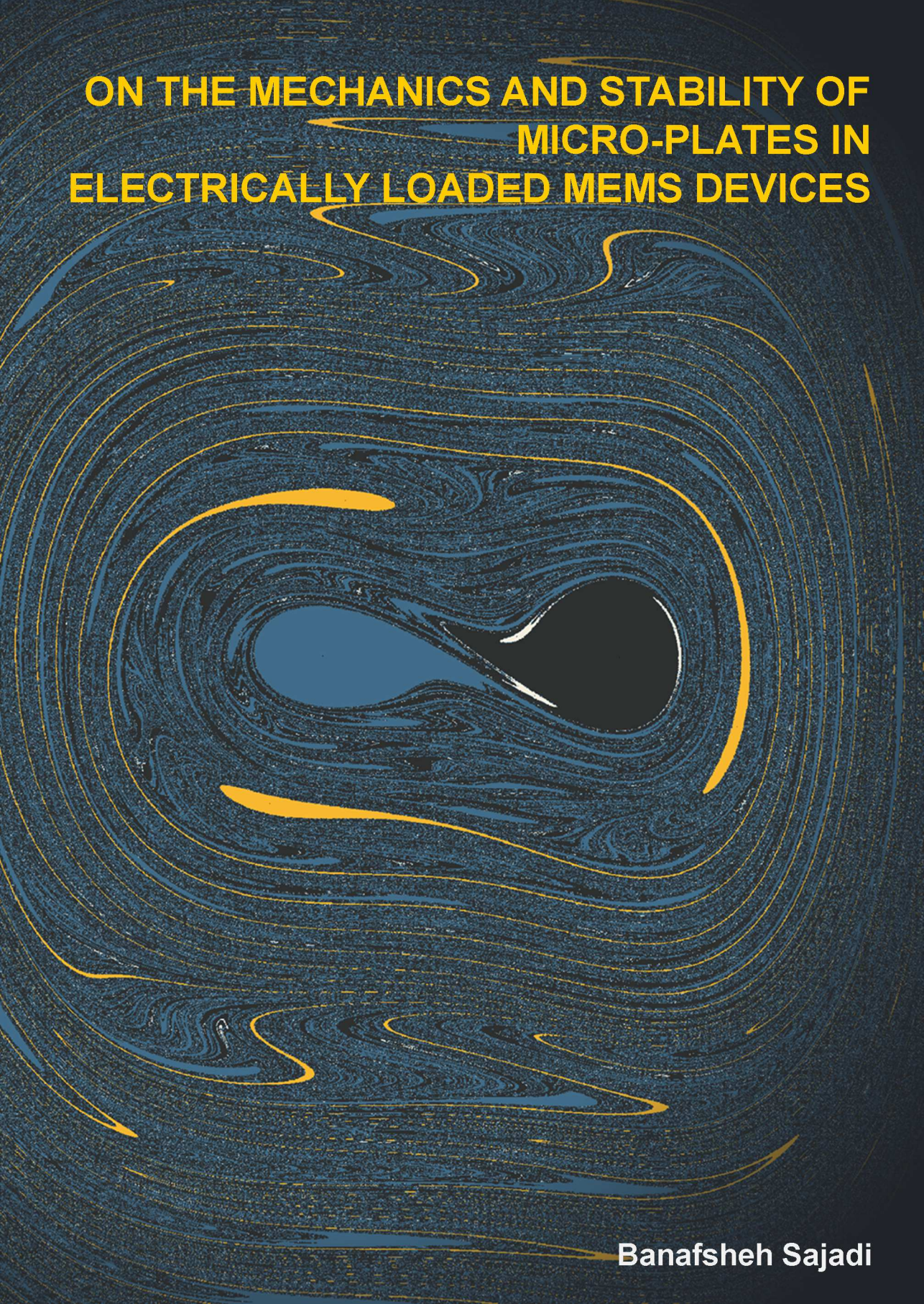
To cite this publication, please use the final published version (if applicable). Please check the document version above.

Copyright

Other than for strictly personal use, it is not permitted to download, forward or distribute the text or part of it, without the consent of the author(s) and/or copyright holder(s), unless the work is under an open content license such as Creative Commons.

Takedown policy

Please contact us and provide details if you believe this document breaches copyrights. We will remove access to the work immediately and investigate your claim.

The background of the cover is a complex, abstract pattern of swirling lines. The colors are primarily dark blue and black, with bright yellow and light blue highlights that create a sense of motion and depth. The lines are dense and intricate, resembling a microscopic view of a material or a complex fluid flow.

**ON THE MECHANICS AND STABILITY OF
MICRO-PLATES IN
ELECTRICALLY LOADED MEMS DEVICES**

Banafsheh Sajadi

**ON THE MECHANICS AND STABILITY OF
MICRO-PLATES IN
ELECTRICALLY LOADED MEMS DEVICES**

ON THE MECHANICS AND STABILITY OF MICRO-PLATES IN ELECTRICALLY LOADED MEMS DEVICES

Proefschrift

ter verkrijging van de graad van doctor
aan de Technische Universiteit Delft,
op gezag van de Rector Magnificus prof. ir. K.C.A.M. Luyben,
voorzitter van het College voor Promoties,
in het openbaar te verdedigen op maandag 11 december 2017 om 15:00 uur

door

Banafsheh SAJADI

Master of Science in Mechanical Engineering-Applied Design,
Sharif University of Technology, Tehran, Iran,
geboren te Tehran, Iran.

Dit proefschrift is goedgekeurd door de

promotor: Prof. dr. A. van Keulen

copromotor: Dr. J. F. L. Goosen

Samenstelling promotiecommissie:

Rector Magnificus,
Prof. dr. A. van Keulen,
Dr. J. F. L. Goosen,

voorzitter
Technische Universiteit Delft
Technische Universiteit Delft

Onafhankelijke leden:

Prof. dr. M. Amabili,
Prof. dr. F. J. Barthold,
Prof. dr. C. Bisagni,
Prof. dr. P. J. French,
Dr. F. Alijani,

McGill University
Technische Universität Dortmund
Technische Universiteit Delft
Technische Universiteit Delft
Technische Universiteit Delft



This thesis is part of NanoNextNL, a micro and nanotechnology innovation consortium of the Government of the Netherlands and 130 partners from academia and industry. More information on www.nanonextnl.nl.

Keywords: Stability, Micro-Plates, Nonlinear dynamics, Bifurcation, Electrostatic MEMS, Pull-in

Printed by: Gildeprint, The Netherlands.

Front & Back: The artwork on the cover is an illustration of the basins of the attractors of an electrically actuated micro-plate while subjected to a differential pressure.

Copyright © 2017 by B. Sajadi

ISBN 978-94-6233-844-9

An electronic version of this dissertation is available at

<http://repository.tudelft.nl/>.

*To my beloved husband, Mohammad,
and to my parents, Azar and Ali.*

CONTENTS

Summary (in English, Dutch and Persian)	ix
1 Introduction	1
1.1 Motivation	2
1.2 Research objectives	4
1.3 Approach of the research	5
1.4 Outline of the thesis.	6
References	8
2 Static stability of electrically loaded micro-plates	11
2.1 Introduction	12
2.2 Analytical formulation	14
2.3 Finite element analysis	17
2.4 Results and discussion	18
2.5 Conclusions.	27
References	28
3 Nonlinear dynamics of electrically actuated micro-plates	31
3.1 Introduction	32
3.2 Problem formulation	33
3.3 Numerical solution of the equation of motion	36
3.4 Results and discussion	37
3.5 Conclusion	41
References	43
4 Effects of pressure on stability of electrically actuated micro-plates	45
4.1 Introduction	46
4.2 Problem formulation	47
4.3 Solution methodology	52
4.4 Results and discussion	53
4.5 Conclusions.	62
References	64
5 Nonlinear vibrations of electrically actuated 2D nano-membranes	67
5.1 Introduction	68
5.2 Experiments and device fabrication.	69
5.3 Theoretical formulation.	71
5.4 Extracting the equivalent Young's modulus	75
5.5 Results and discussion	76
5.6 Conclusions.	82
References	85

6	Capturing size-dependent behavior of plates with nonlocal theory	89
6.1	Introduction	90
6.2	Nonlocal elasticity theory	92
6.3	Effects of thickness in nonlocal plate theory	97
6.4	Results and discussion	104
6.5	Conclusions	108
	References	110
7	Application of micro-plates for surface stress measurements	113
7.1	Introduction	114
7.2	Analytical formulation	115
7.3	Sensitivity of the capacitive membrane sensor	120
7.4	Finite element model	122
7.5	Precision of the sensor	122
7.6	Results and discussion	124
7.7	Conclusion	130
	References	131
8	Electrostatic instability: A mechanism for surface stress sensing	133
8.1	Introduction	134
8.2	Methodology	134
8.3	Results and discussion	135
8.4	Conclusions	138
	References	139
9	Overview, conclusions and recommendations	141
9.1	Overview and conclusions	142
9.2	Limitations and research outlook	145
	References	147
	Curriculum Vitæ	149
	List of Publications	151
	Acknowledgements	153

SUMMARY

In the last decades, Micro-Electro-Mechanical Systems (MEMS) have drawn immense attention due to their potential use in a wide variety of modern applications, including micro-mechanical sensors and actuators. MEMS are devices combining mechanical and electrical components between 1 and 100 micrometers, all integrated into a single chip. The performance of these devices hinges on the deflection and movement of these micro-mechanical components and clearly, improvement and innovation of MEMS require a comprehensive knowledge and in-depth understanding of the nonlinear mechanics of these components.

In spite of the simple geometry of common micro-mechanical components, modeling the mechanics of micro-mechanical sensors and actuators is rather complex. In particular, the mechanics of micro-plates in electrostatic MEMS is entangled with two influential sources of nonlinearity namely, geometrical nonlinearity and the nonlinearity due to the presence of the electric field. These sources of nonlinearity are often the origin of instability and failure in MEMS devices, but might also be exploited to achieve, for example, higher sensitivity in the device. In either way, such nonlinearities shall be incorporated in the modeling and design of these micro-mechanical components.

This thesis provides an investigation on nonlinear mechanics of micro-plates in electrostatic MEMS devices. Based on the proposed models, we are able to predict some phenomena in micro-plates that have not been noticed before and to study these aspects in a detailed level which was not possible previously. In particular, based on total potential energy and a Lagrangian approach, the nonlinear mechanics and stability of a clamped circular micro-plate in interaction with an electrostatic field is studied. The effects of different loading conditions (i.e. static and dynamic electric potential, and with or without presence of a differential pressure) on the stability of such a system are addressed.

The results of this study suggest that in presence of a differential pressure the steady state motion of an electrically actuated micro plate can be bi-stable or even multi-stable. In fact, a differential pressure can cause additional limit points and an unstable solution branch in the —static or dynamic— steady state solutions of the system. Saddle-node and period doubling bifurcations are repeatedly observed in the results and are recognized as main mechanisms of pull-in. Furthermore, one newly observed critical point in static loading is shown to be highly sensitive to the applied differential pressure suggesting the possibility of employing this limit point for sensing applications.

In addition, this thesis provides a study on analyzing *nano-plates* within the framework of continuum mechanics. In this regard, the nonlinear vibrations of an electrically actuated graphene resonator is modeled and a methodology is proposed for

characterization of its mechanical properties. In addition, the possibility of capturing the scaling effects in mechanical behavior of nano-plates by employing a *non-local* continuum theory is addressed. As a results, two modification factors for the extensional and bending stiffness of nano-plates are presented to account for the effect of thickness in the nonlocal elasticity formulations.

Finally, the mechanical performance and instability of a micro-plate as a transducer in surface stress sensing is investigated and an optimized design for such a sensor is proposed. It is shown that using the proposed optimized design, the sensitivity and overall reliability of such capacitive surface stress sensors can be significantly improved.

The proposed techniques for modeling the mechanics of micro-plates in MEMS devices, are simple and computationally efficient. They can provide in-depth insight into MEMS behavior and can be useful for designing MEMS with plate-like micromechanical components.

SAMENVATTING

De afgelopen decennia is er veel interesse voor Micro-Elektromechanische Systemen (MEMS) vanwege hun potentie in verscheidene moderne toepassingen, zoals micro-mechanische sensoren en actuatoren. MEMS integreren mechanische en elektrische componenten, variërend van 1 tot 100 micrometers, in één enkele chip. Het functioneren van deze systemen hangt sterk samen met de vervorming en beweging van de micro-mechanische componenten. Het moge duidelijk zijn dat een uitgebreide kennis en diepgaand inzicht in de niet-lineaire mechanica van deze componenten vereist is voor verbetering en innovatie van MEMS.

Het modelleren van het gedrag van micro-mechanische sensoren en actuatoren is, ondanks de eenvoudige geometrie van gangbare micro-mechanische componenten, tamelijk complex. Om precies te zijn is het mechanisch gedrag van microschaalen in elektrostatische MEMS gekoppeld aan twee bronnen van niet-lineariteit, te weten geometrische niet-lineariteit en niet-lineariteit veroorzaakt door de aanwezigheid van het elektrisch veld. Deze twee bronnen van niet-lineariteit zijn vaak de oorzaak van instabiliteit en falen in MEMS, maar kunnen ook worden ingezet om bijvoorbeeld hogere gevoeligheid te bereiken. In beide gevallen is het belangrijk dergelijke niet-lineariteiten op te nemen in het modelleren en ontwerpen van deze micro-mechanische componenten. In dit proefschrift wordt de niet-lineaire mechanica van microplaten in elektrostatische MEMS onderzocht. Op basis van de ontwikkelde modellen kunnen we enkele, tot noch toe niet eerder ontdekte verschijnselen in microplaten voorspellen, en deze aspecten bestuderen tot op een detailniveau dat niet eerder werd behaald. Op basis van de totale potentiële energie en een Lagrange benadering bestuderen we de niet-lineaire mechanica van een ingeklemde cirkelvormige microplaat die in interactie is met een elektrostatisch veld. Ook worden de effecten van verschillende belastingcondities (d.w.z. een statisch en dynamisch elektrische potentiaal, met of zonder aanwezigheid van een differentiële druk) op de stabiliteit van een dergelijk systeem behandeld. De resultaten van deze studie suggereren dat bij aanwezigheid van een differentiële druk het dynamisch evenwicht van een elektrisch geactueerde microplaat bi-stabiel of zelfs meervoudig stabiel kan zijn. Een differentiële druk kan extra limietpunten en een onstabiele oplossing in de — statische of dynamische — stabiele oplossingen van het systeem veroorzaken. Zadelpunt en periodeverdubbeling bifurcaties worden herhaaldelijk waargenomen in de resultaten en worden aangewezen als hoofdmechanismen van elektrostatische pull-in. Ook blijkt dat een niet eerder waargenomen kritisch punt bij statische belasting zeer gevoelig is voor de verschildruk, wat de mogelijkheid geeft om dit limietpunt te benutten in een sensor.

Daarnaast levert dit proefschrift een studie over het analyseren van nano-platen in het kader van continuümmechanica. De niet-lineaire trillingen van een elektrisch

geactiveerde grafeen-resonator worden gemodelleerd met behulp van continuüm-mechanica, en er wordt een methodologie voorgesteld voor de karakterisering van de mechanische eigenschappen. Tevens wordt de mogelijkheid behandeld om de schaal effecten in het mechanisch gedrag van nano-platen te omschrijven door middel van niet-lokale continuümtheorie. Als resultaat worden twee veranderingsfactoren voor de rek- en buigstijfheid van nano-platen voorgesteld om rekening te houden met het effect van dikte in de niet-lokale elasticiteitsformuleringen. Tot slot wordt de mechanische prestatie en de instabiliteit onderzocht van een microplaat als transducer in een oppervlaktespanningssensor. Een geoptimaliseerd ontwerp voor een dergelijke sensor wordt voorgesteld. Het wordt aangetoond dat de gevoeligheid en betrouwbaarheid van dergelijke capacitieve oppervlakspanningssensoren aanzienlijk kunnen worden verbeterd. De voorgestelde technieken voor het modelleren van de mechanica van microplaten in MEMS-apparaten zijn eenvoudig en snel in reken-tijd. Ze kunnen diepgaand inzicht geven in MEMS gedrag en kunnen nuttig zijn voor het ontwerpen van MEMS met plaatachtige micro-mechanische componenten.

چکیده

در دهه های گذشته، سیستم های میکرو الکترومکانیکی (MEMS) به دلیل کاربرشان در طیف وسیعی از سنسورها و کنترل کننده ها، موضوع بسیاری از پروژه های تحقیقاتی قرار گرفته اند. سیستم های میکروالکترومکانیکی ترکیبی هستند از اجزای مکانیکی و الکتریکی با اندازه ای بین 1 تا 10 میکرومتر که همه آنها در یک تراشه کوچک قرار می گیرند. عملکرد این سیستم ها وابسته به تغییر شکل و حرکت این قطعات میکرو مکانیکی می باشد و به وضوح، برای بهبود و نوآوری آن ها نیاز به دانش جامع و درک عمیق از مکانیک غیرخطی تغییر شکل و حرکت این اجزاء می باشد.

به رغم هندسه ساده اغلب اجزای مکانیکی، معمولاً مدل سازی مکانیک سنسور ها و کنترل کننده های الکترومکانیکی بسیار پیچیده است. به طور خاص، مکانیک میکرو ورق ها هنگامی که تحت بار الکترواستاتیک قرار می گیرند با رفتار غیرخطی (ناشی از غیرخطی هندسی و همچنین میدان الکتریکی) همراه می شود. این منابع غیرخطی اغلب می توانند منشا عدم پایداری و در نهایت خرابی در دستگاه های MEMS شوند. در عین حال، می توان از این رفتار غیرخطی برای ایجاد حساسیت بیشتر در سنسورها بهره برد. طبیعتاً این چنین رفتار غیرخطی می بایست در مدلسازی و طراحی اجزای میکرو مکانیکی در نظر گرفته شود.

این پایان نامه با عنوان "مکانیک و پایداری میکرو ورق ها در دستگاه های MEMS الکترواستاتیکی" تحقیق جامعی در مورد مدلسازی این میکرو ورق ها ارائه می دهد. در این مدل ها، بر اساس رویکرد لاگرانژی و اصل انرژی پتانسیل، مکانیک و پایداری یک میکرو ورق دایره ای در تعامل با میدان الکترواستاتیک مورد بررسی قرار گرفته است. اثرات شرایط بارگذاری مختلف (به عنوان مثال پتانسیل الکتریکی ایستا یا پویا و با حضور فشار) بر پایداری چنین سیستمی مطالعه شده است.

نتایج این مطالعه نشان می دهد که در حضور فشار مکانیکی، حرکت حالت پایدار میکرو ورق می تواند دو-پایدار (bi-stable) یا حتی چند-پایدار (multi-stable) باشد. در واقع، فشار می تواند باعث پدیدار شدن یک یا چند نقطه بحرانی جدید در حل معادلات حالت پایدار سیستم (ایستا یا پویا) شود. نقاط حدی و پریرود دابلینگ در نتایج به دست آمده به طور مکرر مشاهده و به عنوان مکانیسم اصلی عدم پایداری شناخته می شوند. شایان ذکر است که یکی از نقاط بحرانی جدید مشاهده شده در بارگذاری استاتیک به شدت به فشار حساس است و قابلیت استفاده در اندازه گیری فشار را دارد.

علاوه بر این، این پایان نامه مطالعاتی درباره تجزیه و تحلیل نانو ورق ها را در چارچوب مکانیک پیوسته ارائه می دهد. در این راستا، ارتعاش غیرخطی یک رزوناتور گرافینی مدل سازی شده و روشی برای توصیف خواص مکانیکی آن پیشنهاد شده است. علاوه بر این، رفتار مکانیکی نانو ورق ها با استفاده از یک نظریه الاستیسیته نانولوکال مدل شده و در نتیجه، دو عامل اصلاح برای سختی کششی و خمشی نانو ورق ها برای محاسبه وابستگی رفتار الاستیک این ورق ها به ضخامت آنها ارائه شده است.

در نهایت، عملکرد و پایداری یک میکرو ورق به عنوان یک سنسور در اندازه گیری استرس سطحی مورد بررسی قرار گرفته و یک طراحی بهینه برای چنین سنسوری پیشنهاد شده است. این تحقیق نشان می دهد که با استفاده از طراحی بهینه پیشنهاد شده، حساسیت و قابلیت اطمینان کلی چنین سنسورهایی به طور قابل توجهی بهبود می یابد.

مدل های پیشنهادی برای مدل سازی مکانیک میکرو ورق ها در دستگاه های MEMS ساده و کارآمد هستند. این مدل ها می توانند بینش عمیقی نسبت به رفتار MEMS ارائه دهند و می توانند برای طراحی MEMS با اجزای میکرومکانیکی مشابه ورق مفید قرار گیرند.

1

INTRODUCTION

1.1. MOTIVATION

Micro-Electro-Mechanical Systems (MEMS) play a key role in a wide variety of modern applications, including micro-mechanical sensors and actuators. Nowadays, commercial micro-actuators can be found in ink-jet printers, microphones, digital micro-projectors and many more devices. Micro-mechanical sensors, like pressure sensors, accelerometers and gyroscopes, started their successful advance in the late 1990's and now, hundreds of millions of these devices are sold annually, mainly for medical and automotive applications, of which many are invisible to the public [1]. Up till now, many industries have continued to invest in *research and development* to explore new designs and applications of MEMS.

MEMS are typically devices that range from a couple of micrometers to one millimeter in size. Generally, they combine mechanical and electrical components between 1 and 100 micrometers, all integrated into a single chip. Figure 1.1 shows an example of a micro-electro-mechanical sensor with a simple mechanical and electrical setup. In this device, for example, the mechanical component is a micro diaphragm, and the electrical components are the piezo-resistors, bond-pads, and the metal conductors. These components serve as miniaturized transducers that transform one form of energy (mechanical or electrical) into another.

The performance of MEMS devices is often based on the movement and deflection of their micro-mechanical components, such as cantilevers, double clamped beams, or plates. Among different types of micro-mechanical components, a thin plate, with a thickness of less than a micro meter, is a highly suitable candidate for many applications. For instance, a micro-plate can provide the required separation in differential pressure or acoustic sensors. Moreover, a micro-plate as the sensing component can provide an insulation between the electric setup on one side and the measurand on the other side. This insulation allows for application of these sensors in liquid environment which, otherwise, could hinder the electric performance of the device.

Improving the performance of MEMS requires a comprehensive knowledge and in-depth understanding of the mechanics of their micro-mechanical components (i.e. their compliance and sensitivity, the stability condition and the critical threshold for exhibiting instability, and their dynamic characteristics). In this regard, accurate mathematical models are valuable tools for obtaining this knowledge and theoretically characterizing the performance of these devices. Such models can provide insight into the energy transformation process, which sometimes cannot be comprehended in any other way.

In spite of the simple geometry of micro-mechanical components, the underlying physics of micro-mechanical sensors and actuators is rather complex. Aspects, such as surface stress, which are simply negligible on larger scales become significant on a micro-scale [3–5]. Gravity completely loses relevance and instead, electrostatic effects become influential [6, 7]. Insufficient attention to these aspects not only hinders the further development of these devices, but also diminishes their performance, reliability, and consequently, decelerates commercialization.

The underlying physics of MEMS devices is treated in numerous publications scattered throughout the literature. In particular, studies have concentrated on the-

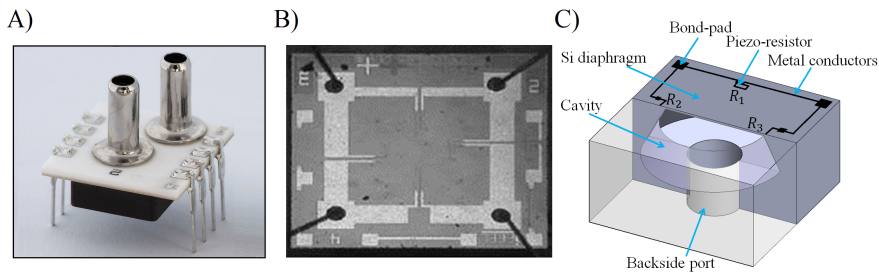


Figure 1.1: A) A commercial piezo-resistive differential pressure sensor, B) optical image of the chip in a piezo-resistive pressure sensor [2], and C) a simplified schematic of a pressure transducer in the pressure sensor. The Micro-Electro Mechanical System combines micro-electrical components (i.e. the piezoresistors and Bond-pads, metal conductors), and micro-mechanical components (i.e. the diaphragm) into a single chip.

oretically characterization and simulation the mechanical behavior of micro-mechanical components in interaction with electric fields. Some reviews of these studies can be found in References [6, 8, 9]. Likewise, the mechanics of clamped micro-plates in electrostatic MEMS devices has drawn great attention in recent years due to their potential for applications in MEMS sensors and actuators [10, 11]. It should be mentioned that this topic has remained a challenging topic due to the presence of different sources of nonlinearity in their physics.

In modeling deflections and movements of micro-plates in electrostatic MEMS, two sources of nonlinearity are most important: geometrical nonlinearity (often referred to as membrane effects) and the nonlinearity due to the presence of the electric field. The latter is a so-called “strong” source of nonlinearity and is the origin of the electrostatic instability (known as pull-in) in electrostatic MEMS devices [12–15]. For these nonlinear problems, exact analytical solutions do not exist and the models to simulate them are typically based on numerical methods. Several studies, therefore, have relied on these methods to study different aspects of mechanics and electrostatic instability of micro-plates in MEMS application [6, 16–19].

Numerical methods such as finite elements, however, are generally time consuming and computationally expensive. Moreover, in nonlinear analysis, numerical simulations with a large number of degrees of freedom present huge computational problems with possible divergence of the solution [20]. In addition, these methods generally present the unstable solution branches laboriously. Hence, in analysis of nonlinear dynamics of electrically actuated micro-plates for instance, they simply fail to present the solution in the entire loading range.

On the other hand, semi-analytical approaches, such as Rayleigh-Ritz variational method, have been shown to be suitable tools to analyze the nonlinear mechanics of beams and resonators with much less computational costs [7, 21]. In employing these methods in mechanics, for instance, the motion of the component is approximated with a minimum number of shape functions which satisfy the boundary conditions and are still capable of describing the correct nonlinear mechanics of the system. Then, a semi-analytical scheme based on the total potential energy can be

employed, and as a result, the nonlinear partial differential equations to be solved are simplified to a large extent.

Rayleigh-Ritz variational methods can be potentially used to model the highly nonlinear mechanics of clamped micro-plates in MEMS applications. Based on such a method, the performance and stability of these components can be characterized. In comparison to finite element method, it deals with very few degrees of freedom and due to its semi-analytical approach, it provides a better insight to the physics of the problem. However, although very promising, a comprehensive study on nonlinear mechanics and particularly stability of electrically driven micro-plates using these methods is not available in the literature.

1.2. RESEARCH OBJECTIVES

The main aims of this research are to investigate the mechanical performance and stability of micro-plates in electrostatic MEMS devices, to provide an in-depth understanding of their mechanical behavior, and to propose techniques to characterize them in a fast and robust manner. The objectives of this thesis which are seen as an approach on how to achieve the main goal are:

- *To explore the nonlinear mechanics and stability of a circular micro-plate in electrostatic MEMS devices*

For this purpose, the static deformation of a clamped micro-plate subjected to a DC electrostatic load is formulated. A stability analysis is performed to characterize the electrostatic instability and pull-in of such a system. Moreover, the effects of a differential pressure on the stability of the micro-plates are studied, and the possibility of employing the electrostatic instability as a sensing mechanism for pressure measurements is investigated.

- *To investigate the nonlinear dynamics of an electrically actuated circular micro-plate in electrostatic MEMS devices*

The nonlinear dynamic behavior of clamped micro-plate when subjected to DC and AC voltages is studied, and the steady state motion of the micro-plate and its stability are investigated. The instability mechanism in different loading conditions are explored and the effect of sequence of the loads (DC and AC voltage, as well as the excitation frequency) on the unstable configurations are studied. Moreover, the effects of a differential pressure on the nonlinear dynamics and stability of an electrically actuated micro-plate are investigated.

- *Exploring the mechanical behavior of plates with nano-scale thickness*

Considering that *Nano-Electro-Mechanical Systems* (NEMS) are basically the next miniaturization step from MEMS devices, the mechanical characterization of plates with nano-scale thickness is also discussed in this thesis. For this purpose, the nonlinear dynamics of an electrically actuated Graphene nano-resonator is studied both theoretically and experimentally. Moreover, the possibility of capturing the scaling effects of the mechanical behavior of plates within the scheme of continuum theories is explored.

- *To characterize the mechanical behavior and sensitivity of micro-plates in surface stress electromechanical sensors*

Surface stress based sensing is one of the current matters of interest in nano-mechanical sensing community [22]. In these sensors the deflection of the micro plate due to a change in its surface stress is detected either directly (by optical instruments) or via capacitive measurements. In this thesis, a methodology is presented to formulate and ultimately optimize the performance of such a sensor. Furthermore, the sensitivity of the electrostatic instability of the sensor to the surface stress changes, as a potential readout mechanism, is investigated.

To achieve the objectives, this thesis provides some novel techniques to model the behavior of micro-plates in MEMS applications. Using these techniques, we are able to predict some phenomena in micro-plates that have not been noticed before. In addition, the provided techniques allow us to study these aspects in detail which was previously not possible. Based on this study, the performance and stability of associated MEMS can be improved, and new MEMS devices can be developed.

1.3. APPROACH OF THE RESEARCH

In this thesis, *theoretical techniques* are employed to study the nonlinear mechanics of micro-plates in electrostatic MEMS devices. Rayleigh-Ritz variational method is employed to approximate the deflection/motion of the micro-plate and to model its nonlinear mechanics. Using this method, in fact, a given variational problem is projected to a limited subspace of shape functions. The crucial point in this method is that the selected subspace should still be able to describe, at least approximately, certain aspects of the real problem.

In the static analysis, this approximation converts the nonlinear partial differential equations to a system of nonlinear equations with unknown parameters which can be solved analytically. In dynamic problems, the nonlinear partial differential equations defining the mechanics of the component are reduced to a set of ordinary differential equations. Then, using a continuation method, the resulting equations are solved and the stability of the solution can be studied.

Next, to verify the accuracy of the proposed model for characterization of dynamics of *nano-membranes*, the nonlinear dynamics of an electrically actuated Graphene nano-resonator is obtained. The effects of DC and AC voltages on the nonlinear resonance of the membrane are investigated, and the results are compared to experimental data.

Since the effective elastic properties of nano-structures have been shown to be strongly size-dependent, as a part of this thesis, a nonlocal elasticity formulation has been employed to capture the scaling effect in plates with relatively small thickness. Using a strong nonlocal theory, a formulation is presented which can reflect these scaling effects in the stiffness matrices as a function of the thickness of the structure.

Finally, to study the sensitivity of a surface stress capacitive sensor, an analytical approximation and a finite element model are employed to describe its electromechanical behavior. Using this approach, we can optimize the design of the sensor to

obtain the maximum capacitive sensitivity. Using the finite element simulation, we study the effect of this optimization on accuracy and precision of the system in surface stress sensing. Moreover, the sensitivity of the electrostatic instability of such a sensor to surface stress changes is obtained using the finite element model.

1.4. OUTLINE OF THE THESIS

This thesis is a collection of articles either published or submitted to peer reviewed journals and conferences. Since the articles are related to each other to some extent, the reader might find some repetition in introduction and methodology sections. The chapters of this thesis are structured as follows.

Chapter 2 studies the mechanical behavior and the stability of a circular flexible electrode, while loaded with an electrostatic and a differential hydrostatic pressure. This analysis is based on both an approximate analytical solution using the principle of minimization of total potential energy, and a finite element simulation. As a result of this study, the critical voltages and deflections of the system can be detected and the possible post-instability behavior of the system are discussed.

Chapter 3 presents a simple method to model the *dynamic* behavior and instability of an electrically actuated circular micro-plate. This method is based on an energy approach and a pseudo arc-length continuation and collocation technique. Steady state motion of a micro-plate subjected to a DC and AC voltage and its instability mechanisms are investigated and discussed.

Chapter 4 presents a method to perform a stability analysis on an electrically actuated circular micro-plate, while it is loaded with a hydrostatic pressure. The methodology in this chapter is similar to that of Chapter 3. Based on the proposed method, we explore how the instability of the system is influenced by the load parameters, namely DC and AC driving voltages, the driving frequency, and the hydrostatic pressure. In the proposed method, the effect of an initial in-plane residual stress is also taken into account.

In Chapter 5, the nonlinear dynamics of an electrically actuated Graphene resonator is studied. The methodology in this chapter is similar to the method which was employed in Chapters 3 and 4, however, the Graphene is modeled using an equivalent *membrane* without any bending stiffness. The validity of the proposed solution is evaluated by comparing the theoretical results to experimental data.

In Chapter 6, using nonlocal elasticity theory, we aim to capture the size-dependent effects of plate structures within the framework of continuum theory. In this chapter, the fundamentals of Eringen's nonlocal elasticity theory, some important considerations and the basis of conventional nonlocal plate theory are reviewed. Furthermore, this chapter investigates how a strong three dimensional nonlocal formulation can incorporate the plate thickness in nonlocal plate theories.

Chapter 7 presents a design for a membrane-based capacitive sensor for surface stress measurements. In this chapter, using an analytical approximation, we formulate and optimize the design of such a sensor with a circular clamped plate /membrane as its sensing component. Moreover, using a finite element model, we study the effect of the shape and position of the agglomeration of target molecules on the ultimate response and accuracy of these types of sensors.

In Chapter 8, the electrostatic instability of the conceptual surface stress sensor, discussed in Chapter 7, is investigated. In particular, using a FEM model, the sensitivity of such instability to the surface stress is obtained and the effect of a differential pressure on this sensitivity is discussed.

In Chapter 9, the conclusions of this research are outlined and a discussion on the advantages and disadvantages of the employed methodology is presented. In addition, some limitations of this study, and recommendations for further research will be presented.

REFERENCES

- [1] M.-H. Bao, *Micro mechanical transducers: pressure sensors, accelerometers and gyroscopes*, Vol. 8 (Elsevier, 2000).
- [2] H. Zhang, H. Guo, Y. Wang, G. Zhang, and Z. Li, *Study on a pcvd sic-coated pressure sensor*, *Journal of Micromechanics and Microengineering* **17**, 426 (2007).
- [3] J. E. Sader, *Surface stress induced deflections of cantilever plates with applications to the atomic force microscope: Rectangular plates*, *Journal of Applied Physics* **89**, 2911 (2001).
- [4] H. Sadeghian, J. Goosen, A. Bossche, and F. Van Keulen, *Surface stress-induced change in overall elastic behavior and self-bending of ultrathin cantilever plates*, *Applied Physics Letters* **94**, 231908 (2009).
- [5] T. Delph, *Near-surface stresses in silicon (001)*, *Surface Science* **602**, 259 (2008).
- [6] W.-M. Zhang, H. Yan, Z.-K. Peng, and G. Meng, *Electrostatic pull-in instability in mems/nems: A review*, *Sensors and Actuators A: Physical* **214**, 187 (2014).
- [7] A. H. Nayfeh, M. I. Younis, and E. M. Abdel-Rahman, *Dynamic pull-in phenomenon in mems resonators*, *Nonlinear dynamics* **48**, 153 (2007).
- [8] W.-C. Chuang, H.-L. Lee, P.-Z. Chang, and Y.-C. Hu, *Review on the modeling of electrostatic mems*, *Sensors* **10**, 6149 (2010).
- [9] D. I. Caruntu and I. Alvarado, *On electrostatically actuated nems/mems circular plates*, in *SPIE Smart Structures and Materials+ Nondestructive Evaluation and Health Monitoring* (International Society for Optics and Photonics, 2011) pp. 79810Z–79810Z–10.
- [10] L.-D. Liao, P. C. Chao, C.-W. Huang, and C.-W. Chiu, *Dc dynamic and static pull-in predictions and analysis for electrostatically actuated clamped circular microplates based on a continuous model*, *Journal of Micromechanics and Microengineering* **20**, 025013 (2010).
- [11] G. W. Vogl and A. H. Nayfeh, *A reduced-order model for electrically actuated clamped circular plates*, in *ASME 2003 International Design Engineering Technical Conferences and Computers and Information in Engineering Conference* (American Society of Mechanical Engineers, 2003) pp. 1867–1874.
- [12] I. O. Wygant, M. Kupnik, and B. T. Khuri-Yakub, *Analytically calculating membrane displacement and the equivalent circuit model of a circular cmut cell*, in *Ultrasonics Symposium, 2008. IUS 2008. IEEE*, pp. 2111–2114.
- [13] K. Das and R. C. Batra, *Symmetry breaking, snap-through and pull-in instabilities under dynamic loading of microelectromechanical shallow arches*, *Smart Materials and Structures* **18**, 115008 (2009).
- [14] G. Duan and K.-t. Wan, *“pull-in” of a pre-stressed thin film by an electrostatic potential: A 1-d rectangular bridge and a 2-d circular diaphragm*, *International Journal of Mechanical Sciences* **52**, 1158 (2010).

- [15] S. Krylov and S. Seretensky, *Higher order correction of electrostatic pressure and its influence on the pull-in behavior of microstructures*, *Journal of Micromechanics and Microengineering* **16**, 1382 (2006).
- [16] P. M. Osterberg and S. D. Senturia, *M-test: A test chip for mems material property measurement using electrostatically actuated test structures*, *Microelectromechanical Systems, Journal of* **6**, 107 (1997).
- [17] A. Sharma and P. J. George, *A simple method for calculation of the pull-in voltage and touch-point pressure for the small deflection of square diaphragm in mems*, *Sensors and Actuators A: Physical* **141**, 376 (2008).
- [18] J. Cheng, J. Zhe, X. Wu, K. R. Farmer, V. Modi, and L. Frechette, *Analytical and fem simulation pull-in study on deformable electrostatic micro actuators*, in *Technical Proc. of the International Conf on Modeling and Simulation of Microsystems, MSM* (2002) pp. 298–301.
- [19] V. Tsouti and S. Chatzandroulis, *Sensitivity study of surface stress biosensors based on ultrathin si membranes*, *Microelectronic Engineering* **90**, 29 (2012).
- [20] S. Saghir and M. I. Younis, *An investigation of the static and dynamic behavior of electrically actuated rectangular microplates*, *International Journal of Non-Linear Mechanics* **85**, 81 (2016).
- [21] A. H. Nayfeh, M. I. Younis, and E. M. Abdel-Rahman, *Reduced-order models for mems applications*, *Nonlinear dynamics* **41**, 211 (2005).
- [22] in *13th International Workshop on Nanomechanical Sensing* (Delft University of Technology, 2016).

2

STATIC STABILITY OF ELECTRICALLY LOADED MICRO-PLATES

Electrostatic load is generally the main driving parameter in MEMS applications, and electrostatic instability is one of the main features of many electrostatic MEMS and NEMS devices. In this chapter, we aim to find an analytical approximation to formulate the micro-plate's static response when subjected to an electrostatic and a differential pressure. We investigate how the characteristics of the electrostatic instability of a micro-plate can be affected, due to presence the differential pressure. The results of this study indicate that the differential pressure can have a significant influence on the equilibrium path, the number and position of unstable points, and the post instability behavior of such a structure. As a result, while the system is loaded and unloaded with the electric potential, the electrostatic instability might coincide with a snapping behavior. This behavior makes the system very appealing for sensing and actuating applications. This analysis is based on both an analytical framework and finite element simulations.

2.1. INTRODUCTION

Electrostatic instability (and bi-stability) is an important feature of many electrostatic MEMS devices, sensors and actuators [2–4]. A solid understanding of the electrostatic instability is essential to improve the performance such MEMS/NEMS devices and to obtain new designs for new applications.

Electrostatic MEMS devices essentially consist of a simple parallel plate capacitor with at least one flexible electrode. When an electric potential is applied to the capacitor, an attractive electrostatic load is induced between its electrodes. This load depends on the applied electric potential, the local distance between the electrodes, and the dielectric constant of the medium separating them [5]. The electrostatic load leads to deformation of the flexible electrode(s) to maintain the balance between electrostatic and elastic potentials. Thus, any small change in the electric potential can generate mechanical movement of the flexible plate, which can be used for actuation [6].

Instability of an electrostatic MEMS device occurs mainly due to the nonlinearity in the electrostatic potential [7]. When the system becomes unstable, any perturbation could lead to failure or “pull-in” of the flexible electrode. This stability phenomenon appears as a ‘fold’ or a ‘limit point’ in the equilibrium curve of the system [8].

In certain electrostatic MEMS devices, e.g. microphones and pressure sensors or actuators, it is essential to avoid ‘pull-in’ effects, since the contact between the two electrodes induces failures, including short circuit, stick, wear, dielectric changing, and breakdown [7, 9]. On the other hand, pull-in is a feature of MEMS/NEMS devices [3] which can also provide information on the mechanical and physical characteristics of the system. Therefore, it has been introduced as a robust mechanism for measuring the mechanical properties of nano-structures [10], or sensing the adsorbate stiffness in nano-mechanical resonators [11].

In order to avoid or employ the pull-in effect, an in-depth knowledge of the stability behavior and an accurate determination of the pull-in voltage of the structure is critically required. In engineering applications, to approximate the critical deformation of the electrode and to predict the pull-in voltage, a simple 1-D spring-mass model is commonly used (see Figure 2.1). In such a model, the instability occurs when due to the deformation of the flexible electrode, the gap between the two electrodes becomes two thirds of the initial gap [8, 12, 13]. This simplified model is commonly referred to as the ‘1/3 air gap rule’.

In practice, however, a membrane/plate structure is different from a simple spring

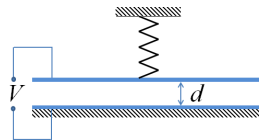


Figure 2.1: Simple 1-D model typically used to approximate the critical deformation of the electrode in order to predict the pull-in voltage.

mass model. It is a 2D structure which incorporates Poisson ratio effects, and membrane stiffening effects. In addition, if the plate-like electrode deforms, the electrostatic load is no longer uniform. The 1/3 air gap model inherently does not account for any of these effects. However, the critical gap being equal to two-thirds of the initial gap size, is proved as the most conservative critical gap in MEMS capacitors [12].

The pull-in of circular clamped plate-like electrodes has been investigated and formulated in many studies [9, 12, 14]. These studies are based on simplifying assumptions, such as small and one-dimensional deformation of the plate, or uniformity of the electrostatic load. Ultimately, finite-difference and finite-element methods have been applied to solve the resulted equations [9, 15, 16]. Different amounts of critical deformation were proposed for circular clamped electrodes, from 41.5% [9] or 41.6-45.6% [15] to 72-75% [16] depending on the thickness of their structures and their simplifying assumptions. However, a comprehensive *analytical* solution for pull-in voltage of a circular clamped plate considering the nonlinear membrane effects and non-uniformity of electrostatic load is missing in the literature.

The pull-in voltage and critical deflection of cantilever-, beam- or plate-like electrodes depend on the stiffness of the flexible component, as well as the initial distance between the electrodes. A mechanical load applied to the component can directly affect both parameters, and consequently, influences the electrostatic instability of the system. The sensitivity of electrostatic instability to a mechanical load is the concept behind using pull-in instability as a mechanism for sensing, for example, temperature [17], surface-stress [5], or residual stresses in clamped structures [8]. Furthermore, MEMS sensors and actuators are frequently designed to operate under a mechanical load, e.g., capacitive pressure sensors. Sometimes, the additional mechanical load in these devices is undesired, but also inevitable, e.g., thermal loads or residual stresses in clamped structures. Therefore, an in-depth knowledge about the effect of these mechanical loads on the stability of the micro mechanical component is paramount.

The dependency of the pull-in voltage of MEMS devices to external mechanical loads, such as a uniform transverse, or, in-plane load, has been investigated in the literature [8, 13, 18, 19]. The effect of a uniform differential pressure on the electrostatic instability of a circular micro plate has been studied as well [20]. The later, using a numerical continuation scheme, calculated the combination of pressure and voltage which can lead to the instability of the system. This study considers the differential and the electrostatic pressure to be in the same direction and it shows that the differential pressure always causes the system to be more prone to instability. It should be noticed that the proposed numerical method, even if highly accurate, is an expensive tools, and, for each new set of design parameters (radius or thickness) the simulation has to be repeated. An accurate analytical model –if available– could provide a closed form solution for approximating the pull-in voltage and the critical deformation almost without any time cost. In addition, it provides more insight to the problem which is favored for design purposes.

In this chapter, we propose an analytical approximate methodology to study the stability and pull-in behavior of a circular flexible electrode, while, loaded with electrostatic and differential pressure. In this analysis, the direction of the pressure is not predefined. Instead, it is considered to be a differential pressure positive when op-

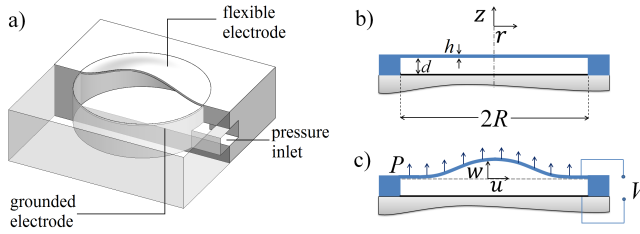


Figure 2.2: Schematic of (a) a capacitor with flexible, circular electrode subjected to a differential pressure, its cross section in (b) undeformed and (c) deformed configurations due to the electrostatic load and the differential pressure.

posing the electrostatic load, and negative otherwise. The non-linear stretching of the thin plate and the non-uniformity of electrostatic load due to deflection of the flexible plate, are incorporated in this solution. In addition, in order to verify the results of the analytical solution, a finite element model is employed [21].

Using the proposed solutions, first, the instability and pull-in behavior of the electrode and its dependency on the electrode's thickness and radius are discussed. The accuracy of the proposed analytical approximation is evaluated with a comparison to the finite element simulations. Next, we explore how a differential pressure and its direction would affect equilibrium, stability, and the critical voltages and deflections. In addition, the post-instability behavior of the system and possible snapping behavior will be discussed.

2.2. ANALYTICAL FORMULATION

The analytical model proposed here is based on a parallel plate capacitor with a very thin, circular, fully clamped plate as one electrode, while the other is fixed and rigid. The shape of the capacitor is chosen to be circular, since the MEMS devices with a circular plate generally yield better structural flexibility as compared to rectangular plates. In addition, they have no corners or sharp edges which may induce high residual stresses during fabrication process [15]. The schematic of the assumed model is shown in Figure 2.2.

The radius of the flexible electrode is R and its thickness is h . It is modeled with a linear elastic, homogeneous and isotropic material model. The Young's modulus and Poisson ratio of the plate are denoted E and ν , respectively. The plate is suspended over the grounded electrode with similar radius and the initial gap between the electrodes is d . The plate is loaded with a differential pressure P , and an electric potential V is applied to the electrodes.

The plate is modeled with von Kármán's plate theory, which accounts for finite deflection but moderate rotations and is adequate for thin plates [22]. The loads are conservative, which implies that first, to estimate the deflection in the equilibrium state, approximations based on minimizing the total potential energy can be applied, and second, no dynamic consideration is required to assess stability.

Minimizing the total potential energy is a variational problem and its solution can be estimated using Ritz's method. In this method a parametrized displacement field satisfying the clamping boundary condition is considered, whereas the unknown parameters are calculated by requiring the total potential energy to be stationary.

Due to the axisymmetric condition in the problem at hand, the only appearing displacement components are the radial (u) and transverse (w) components. Although, the nonlinearity might cause the symmetry to break up, we consider the symmetry to maintain during deformation. This assumption has been verified using a finite element model which will be described in the next section. The clamping boundary condition forces the displacement components and also the first derivative of the transverse displacement with respect to the radial coordinate to be equal to zero at the boundaries. We adopt Timoshenko's simple approximate displacement field for uniformly loaded circular plates [23], to approximate the radial (u) and transverse (w) displacements:

$$\begin{aligned} w &= C_1 d(1 - \rho^2)^2, \\ u &= R\rho(1 - \rho)(C_2 + C_3\rho), \end{aligned} \quad (2.1)$$

where $\rho = \frac{r}{R}$ is the non-dimensional radial coordinate and, C_i , ($i=1-3$,) are the parameters to be calculated. Next, the associated total potential energy is evaluated. The total potential energy consists of four terms namely, the electrostatic potential (U_e), the potentials associated with elastic deformation due to the bending (U_b) and the stretching (U_s) of the plate, and the potential associated with the mechanical pressure (W):

$$U = U_e + U_b + U_s - W. \quad (2.2)$$

Assuming the parallel-plate capacitor theory, the electrostatic potential follows as [3]:

$$U_e = -\pi\epsilon V^2 R^2 \int_0^1 \frac{\rho d\rho}{d + w}, \quad (2.3)$$

where ϵ is the electric permittivity of the dielectric between the electrodes. Notice that the local distance between the electrodes ($d + w$) is employed to calculate the electrostatic potential. Thus, the non-uniformity of the electrostatic load due to the deflection of the flexible electrode has been incorporated.

Next, considering von Karman's plate theory (moderate rotations), the potentials associated with elastic deformation due to the bending (U_b) and the stretching (U_s) of the plate are [22]:

$$U_b = \frac{\pi D}{R^2} \int_0^1 \left(\left(\frac{\partial^2 w}{\partial \rho^2} \right)^2 + \left(\frac{1}{\rho} \frac{\partial w}{\partial \rho} \right)^2 + \left(\frac{2\nu}{\rho} \frac{\partial w}{\partial \rho} \frac{\partial^2 w}{\partial \rho^2} \right) \right) \rho d\rho, \quad (2.4a)$$

$$U_s = \frac{\pi E h}{(1 - \nu^2)} \int_0^1 \left(\left(\frac{u}{\rho} \right)^2 \right. \quad (2.4b)$$

$$\left. + \left(\frac{\partial u}{\partial \rho} + \frac{1}{2R} \left(\frac{\partial w}{\partial \rho} \right)^2 \right)^2 \frac{2\nu u}{\rho} \left(\frac{\partial u}{\partial \rho} + \frac{1}{2R} \left(\frac{\partial w}{\partial \rho} \right)^2 \right) \right) \rho d\rho, \quad (2.4c)$$

where $D = \frac{Eh^3}{12(1-\nu^2)}$ is the bending stiffness of the flexible plate. Notice that nonlinear membrane effects have been incorporated in the elastic potential.

As the rotations in the plate due to mechanical and electrostatic loads are small, the pressure is assumed to be always perpendicular to the undeformed surface. Therefore, the potential associated with the pressure can be calculated as:

$$W = 2\pi PR^2 \int_0^1 w\rho d\rho. \quad (2.5)$$

By substituting Equation 2.1 into Equations 2.3–2.5, an approximation for the total potential energy can be derived analytically. The analytical expression of the integral in Equation 2.3, depends on the sign of the parameter C_1 . We calculate the total potential energy and solve the problem for $C_1 < 0$ and $C_1 > 0$, separately:

$$\begin{aligned} U = & -\epsilon V^2 \frac{\pi R^2}{2d} (F(C_1)) - P \frac{\pi R^2 d}{3} C_1 \\ & + \frac{32\pi d^2}{3R^2} DC_1^2 + \frac{EhR^2\pi}{(1-\nu^2)} \left(\alpha_1 C_2^2 \right. \\ & + \alpha_2 C_3^2 + \alpha_3 C_2 C_3 - \alpha_4 C_1^2 C_2 \frac{d^2}{R^2} \\ & \left. + \alpha_5 C_3 C_1^2 \frac{d^2}{R^2} + \alpha_6 C_1^4 \frac{d^4}{R^4} \right), \end{aligned} \quad (2.6)$$

where, α_i is introduced for compactness, with $\alpha_1 = 0.250$, $\alpha_2 = 0.117$, $\alpha_3 = 0.300$, $\alpha_4 = 0.068$, $\alpha_5 = 0.055$, $\alpha_6 = 0.305$. These parameters are determined by the selected basis-functions, and represent the linear and nonlinear stretching stiffness components in the strain energy. Moreover,

$$F(C_1) = \frac{\operatorname{atanh}\sqrt{-C_1}}{\sqrt{-C_1}} \quad \text{if } C_1 < 0, \quad (2.7a)$$

$$F(C_1) = 1 \quad \text{if } C_1 = 0, \quad (2.7b)$$

$$F(C_1) = \frac{\operatorname{atan}\sqrt{C_1}}{\sqrt{C_1}} \quad \text{if } C_1 > 0. \quad (2.7c)$$

Notice that $F(x)$ is a continuous and smooth function around zero.

Next, the stationary points of total potential energy (U) can be found by equating its derivative to the unknown parameters (C_i) to zero,

$$\frac{\partial U}{\partial C_1} = \frac{\partial U}{\partial C_2} = \frac{\partial U}{\partial C_3} = 0. \quad (2.8)$$

Solving Equation 2.8 for parameters C_2 and C_3 , leads to a relation between the stretching of the electrode and its transverse deflection, independent of the applied loads, V and P . As a matter of fact, C_2 and C_3 can be calculated as a function of C_1 and substituted into Equation 2.6. Hence, the degrees of freedom can be reduced to C_1 only, while incorporating the in-plane deformation, as well. Then, equilibrium requires:

$$\frac{\partial U}{\partial C_1} = 0, \quad (2.9)$$

which leads to:

$$\begin{aligned}
 & -\epsilon V^2 \frac{\pi R^2}{2d} \left(\frac{1}{2C_1(1+C_1)} - \frac{F(C_1)}{2C_1} \right) \\
 & + \frac{64\pi}{3} \left(\frac{d}{R} \right)^2 D \left(C_1 + 0.488 \left(\frac{d}{h} \right)^2 C_1^3 \right) \\
 & - P \frac{\pi R^3}{3} \frac{d}{R} = 0.
 \end{aligned} \tag{2.10}$$

It is worth to note that in Equation 2.10, two sources of nonlinearity are incorporated: (1) the cubic term due to the geometrical nonlinearity and, (2) the nonlinearity of electrostatic load. Due to the presence of nonlinearity, multiple equilibrium states might be found for one load case (P and V). Therefore, the equilibrium path might exhibit one or even more bifurcations, at which solution branches meet. The stability of the solution can be defined by the sign of the second derivative of the total potential energy with respect to the only degree of freedom left (C_1). In fact, the system is stable, when the second derivative is positive, and unstable, if it is negative.

The critical point(s) can be calculated by equating the second derivative of the total potential energy with respect to the only degree of freedom to zero. This, from a physics point of view, means that the system would have no stiffness in the direction of the subjected degree of freedom. Therefore, the second derivative of the total potential energy at the critical points can be calculated as:

$$\begin{aligned}
 \frac{\partial^2 U}{\partial C_1^2} = & \\
 & -\epsilon V^2 \frac{\pi R^2}{2d} \left(-\frac{5C_1+3}{4(C_1+1)^2 C_1^2} + \frac{3F(C_1)}{4C_1^2} \right) \\
 & + \frac{64\pi d^2}{3R^2} D \left(1 + \alpha_7 \left(\frac{d}{h} \right)^2 C_1^2 \right) = 0.
 \end{aligned} \tag{2.11}$$

where $\alpha_7 = 1.464$.

Recall that at the critical points, the system is still in equilibrium. Thus, Equations 2.10 and 2.11 should be solved simultaneously in order to calculate the critical deflection(s) and voltage(s). The critical value of voltage and deflection are denoted with superscribe cr . With such an analytical solution, one can accurately approximate the voltage level(s) at which instability occurs as a function of the material properties, the geometrical parameters, and the applied differential pressure. It is worth noting that since Equations (2.10) and (2.11) are both highly nonlinear in C_1 , solving these equations numerically is relatively difficult. Therefore, as an alternative, one can simply solve these equations for P and V for a feasible range of critical C_1^{cr} (e.g. -0.99 to +1). This approach will result in obtaining C_1^{cr} as a numeric function of P and V .

2.3. FINITE ELEMENT ANALYSIS

To verify the results of the analytical estimation, a 3D capacitor with circular electrodes was modeled using finite elements (COMSOL Multiphysics [21]). In the model,

one electrode is considered to be flexible, clamped on the edge, and suspended over the grounded electrode. The medium was discretized with solid elements using free tetrahedral meshing. The material properties and specifications of the model, that are used for the test case for this solution, are: $E = 80\text{Pa}$, $\nu = 0.2$, $d = 2\mu\text{m}$, and $\epsilon = 8.854 \times 10^{-12} \text{m}^{-3}\text{kg}^{-1}\text{s}^4\text{A}^2$. To study the effect of the dimensions of the electrode, different combinations of thickness and radius have been studied.

In order to calculate the equilibrium path for this structure, the differential pressure and *average* deflections of the plate are prescribed. Then, the required electric potential to maintain the equilibrium of the plate in such a configuration is calculated. To solve the highly nonlinear equations, the Newton method was employed. This calculation is repeated over a range of average deflections and as a result, the equilibrium path of the system is achieved. The critical voltage(s) is then found by tracing the limits of electric potential.

It should be noticed that in the finite element model the displacement field and its symmetry is not imposed to the system. However, the displacement field appear to be completely symmetric for both the resulting stable and unstable solution branches. The results from this model is compared with the proposed analytical solution in the “Results and Discussion” section.

2.4. RESULTS AND DISCUSSION

In this section, the influence of a uniform pressure on the critical deflection and voltage of a parallel plate capacitor with a circular flexible electrode, will be studied. The results of the proposed analytical approximation will be discussed and compared with finite element simulations. For this purpose, normalized load parameters are introduced as:

$$\begin{aligned} \text{normalized voltage: } V' &= V \sqrt{\frac{12\epsilon R^4(1-\nu^2)}{d^6 E}}, \\ \text{normalized pressure: } P' &= P \frac{1-\nu^2}{E}. \end{aligned} \quad (2.12)$$

In addition, the maximum deflection of the plate is normalized with the initial gap size d .

First, consider the case with no pressure ($P' = 0$). The corresponding deflection deformation is modeled as expressed by Equation 2.1. The maximum deflection occurs at the midpoint ($\rho = 0$), and is equal to $C_1 d$.

Figure 2.3 shows how the midpoint deflection varies with the applied voltage. The presented curves are determined analytically for different thicknesses of the flexible electrode. The results of the finite element simulations are also shown, and as can be observed, they confirm the accuracy of the approximate analytical solution. The error between these two solutions in worst case ($h/d = 0.1$) occurs at the limit point and is less than 8%. In fact, the accuracy of the analytical solution is better for thicker electrodes.

As Figure 2.3 indicates, the deflection of the midpoint of the flexible electrode increases monotonically with the applied voltage until the system reaches a limit point

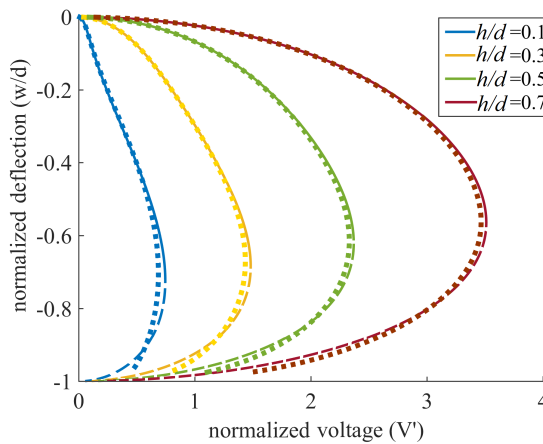


Figure 2.3: The equilibrium path of the midpoint of the circular flexible electrode for different thicknesses, and radius $R = 100\mu\text{m}$. — stable equilibrium, - - - unstable equilibrium, and ■■■ finite element simulations (COMSOL Multiphysics).

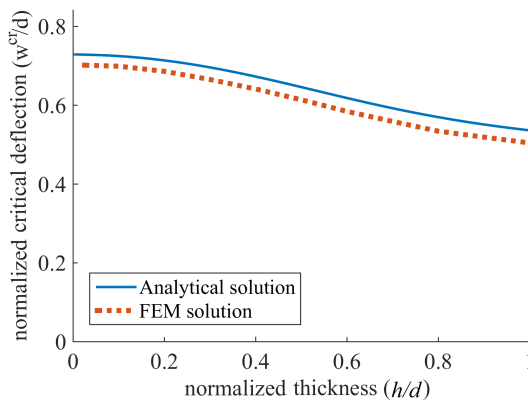


Figure 2.4: The normalized critical deflection at the midpoint of a circular plate with radius $R = 100\mu\text{m}$, as a function of its normalized thickness h/d .

or saddle-node bifurcation. At this critical point, the system becomes unstable, and if the voltage is increased, it leads to pull-in.

It can be observed from Figure 2.3 that the critical deflection depends on the thickness of the structure. In fact, solving Equations 2.10 and 2.11 for $P = 0$, results in a critical deflection ($\frac{w^{cr}}{d} = C_1^{cr}$) which is only a function of h/d . This function is shown in Figure 2.4. The critical deflection calculated with the proposed method varies between 51-71% of the initial gap between the electrodes and is always higher than 1/3 of the initial gap which is calculated with a simple 1D spring model. This, as mentioned before, is because modeling the elastic restoring forces with a linear spring does not account for the non-uniform electrostatic force on the plate after deflection, and, the nonlinear stiffening effect of the flexible electrode. The latter effect is

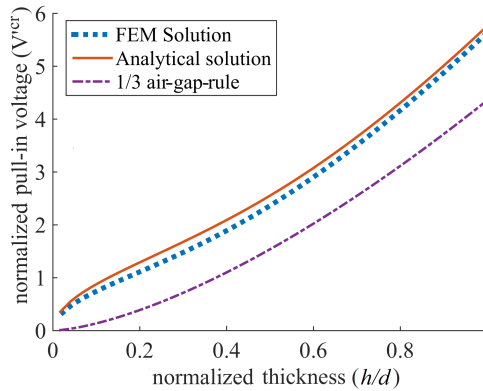


Figure 2.5: The normalized pull-in voltage of a circular plate with radius $R = 100\mu\text{m}$, as a function of its normalized thickness h/d calculated with different methods.

more pronounced for thinner plates, causing $\frac{w^{cr}}{d}$ to be larger.

The critical voltage of the system, depends on the material properties and the dimensions of the capacitor. Solving Equations (2.10) and (2.11) for $P = 0$ shows that the pull-in voltage is proportional to $1/R^2$, which is in agreement with the experimental results presented by Osterberg [24]. The *normalized* critical voltage as defined using Equation (2.12), only depends on the normalized thickness, see Figure 2.5. For comparison, the finite element results and the results of a simple solution based on 1/3-air-gap theory with uniform electrostatic load (as explained in [12]), are also shown. It is worth to note that the results presented in this graph are closely similar (5% different) to the classical limit provided by Ansari *et al.* [25]. In the latter, the authors have employed couple stress and strain gradient elasticity theory to obtain the size dependent pull-in characteristics for a micro-plate with $h/d = 0.83$. However, since the geometric nonlinearity is not considered in the mentioned article, the obtained critical deflections are significantly different.

For thinner plates where the nonlinear stiffening effect is more significant, the simple 1D linear spring model (1/3-air-gap rule) predicts a significantly lower critical voltage as compared to the finite element solution; while, the approximate analytical solution presented here can predict very precise results. However, although the critical voltage calculated with the 1D linear spring model is inaccurate for the circular membranes, it provides a conservative approximation for the critical deflection.

Next, consider the case where a differential pressure, positive in opposing direction of the electrostatic load, is applied ($P' \neq 0$). This time, two load parameters, i.e. pressure and electrostatic load are involved in the stability analysis. In order to calculate the limit voltage we preserved the pressure and consider the voltage as the varying load parameter. The midpoint deflection of the electrode as a function of applied voltage is shown for three different differential pressures in Figure 2.6.

In fact, pressurizing the flexible electrode can significantly affect the shape of the equilibrium path: first of all, a mechanical pressure leads to an initial deflection in the plate when $V = 0$. This initial deflection depends on the amount and direction of the applied pressure. Second, a differential pressure might influence the position

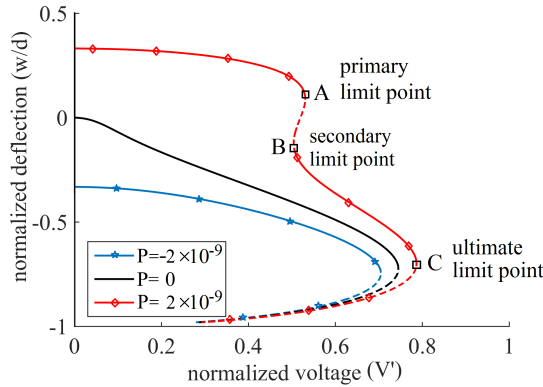


Figure 2.6: The midpoint deflection of the circular flexible electrode with thickness $h = 0.2\mu\text{m}$ and radius $R = 100\mu\text{m}$ as a function of applied voltage, for differential pressures in different directions. — stable equilibrium, - - - unstable equilibrium.

and/or number of limit points.

As Figure 2.6 shows, when a negative (downward in Figure 2.2) pressure is applied, the pull-in voltage drops and the critical deflection slightly increases. This is because a negative differential pressure decreases the average initial distance between the electrodes. Though, the overall shape of the equilibrium path remains the same.

For positive pressures, however, the shape of the equilibrium path might differ significantly (see $P' = 2 \times 10^{-9}$ in Figure 2.6). In such a case, the system exhibits one or three saddle-node bifurcations in its equilibrium path [22]. One limit point (Point C in Figure 2.6) is close to the limit point in an unloaded system, i.e. $P' = 0$. Only, due to the initial deflection of the plate and the associated additional geometrical stiffness, this limit point occurs at a slightly different voltage and deflection. We refer to this critical point as the “ultimate” limit point. Another limit point occurs earlier when the deflection of the plate is still in the positive direction (Point A in Figure 2.6). We shall refer to this point as the “primary” limit point. The other limit point is a local minimum in the applied voltage (Point B). If we ramp up the voltage on the upper stable branch around Point A, or, ramp down the voltage on the lower stable branch around Point B, the system might jump from one stable configuration to the other.

Similar bi-stability behavior has been observed for shallow arched structures [26]. These structures may exhibit two different stable configurations under the same applied electrostatic load and they can snap from one to the other. For the problem at hand, the pressure is causing the initially flat flexible electrode to behave like an arched structure.

In order to verify the analytical approximate, the equilibrium path calculated by the finite element model is provided in Figure 2.7. The results of the numerical solution confirm the accuracy of the approximate analytical solution. The error between these two solutions appears to be the most at the ultimate limit point (less than 4%). Similar to the case of no pressure, the accuracy of the analytical solution is better for

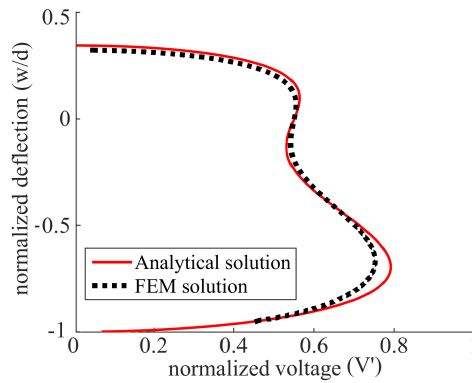


Figure 2.7: The midpoint deflection of the circular flexible electrode with thickness $h = 0.2\mu\text{m}$ and radius $R = 100\mu\text{m}$ as a function of applied voltage, when $P' = 2 \times 10^{-9}$.

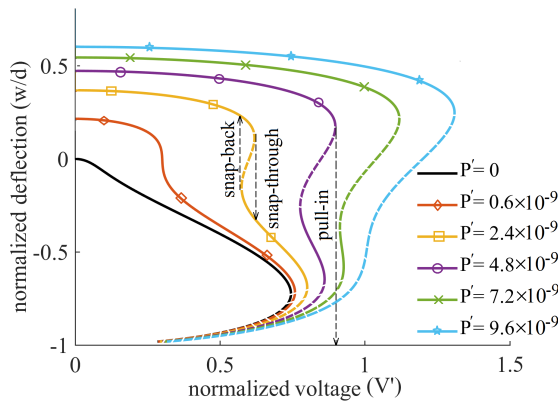


Figure 2.8: The midpoint deflection of the circular flexible electrode with thickness $h = 0.2\mu\text{m}$ and radius $R = 100\mu\text{m}$ as a function of applied voltage, for different positive pressures. — stable equilibrium, - - - unstable equilibrium

thicker electrodes.

After the system passes the primary limit point, the post-instability behavior depends on the applied pressure. Figure 2.8 shows the midpoint deflection as a function of applied voltage, for different positive pressures. It can be observed that the primary limit point can only be noticed if the pressure is higher than a certain threshold. If the applied pressure is too small (see $P' = 0.6 \times 10^{-9}$ in Figure 2.8), then, the shape of the equilibrium path changes slightly, and the primary instability is not observed. For higher pressure, though, the primary limit point exists.

For moderate pressures, the primary limit voltage is lower than the ultimate limit voltage. Therefore, the instability leads to the snapping behavior discussed before (see $P' = 2.4 \times 10^{-9}$ in Figure 2.8). For larger pressures, the primary critical voltage exceeds the ultimate pull-in voltage and thus, a small perturbation may lead to pull-

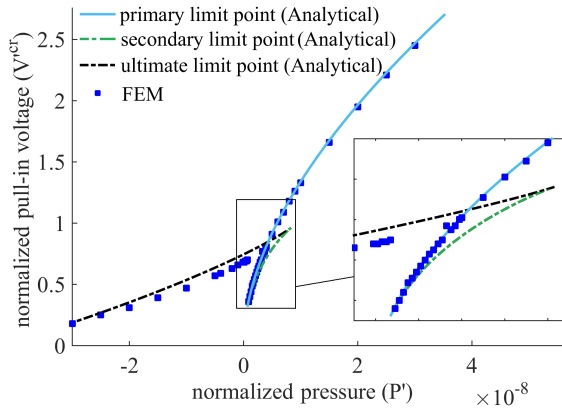


Figure 2.9: The critical voltages for a test case with thickness $h = 0.2\mu\text{m}$ and radius $R = 100\mu\text{m}$, as a function of the applied mechanical pressure.

in of the flexible electrode (see $P' = 4.8 \times 10^{-9}$). For larger pressures, the so-called secondary and ultimate limit points totally vanish.

If during the electrostatic loading, a snap-trough occurs from the upper stable branch to the lower branch (e.g. for $P' = 2.4 \times 10^{-9}$ in Figure 2.8), the unloading of the system can also lead to a snap-back from the lower stable branch to the upper one. However, the snap back occurs at a lower voltage at the secondary limit point. This limit point is only observed for the pressure range that both primary and ultimate limit points are present.

Clearly, the critical voltage(s) and limit deflection(s) depend on the applied mechanical pressure. The variation of the limit voltage(s) versus the applied mechanical pressure is shown in Figure 2.9. As can be seen, the results of analytical and finite element simulations are in good agreement, which again demonstrates the accuracy of the approximate solution.

In Figure 2.9, for negative pressures, only one limit point is observed which is associated with the ultimate limit point or the pull-in of the flexible electrode. In this region ($P' < 0$), there is a near-linear relation between the pull-in voltage and the applied pressure. The pull-in voltage monotonically decreases with increasing the amplitude of the pressure in negative (downward) direction.

For positive pressures, three different regions can be observed. First, for very small pressures, only the ultimate limit point is observed. This is associated with the limit point for $P' = 0.6 \times 10^{-9}$ in Figure 2.8. Then, there is a region in which the system exhibits all three limit points. The examples of $P' = 2.4 \times 10^{-9}$, 4.8×10^{-9} and 7.2×10^{-9} in Figure 2.8 belong to this region. Depending on the value of the applied pressure, the primary limit voltage might be less or more than the ultimate limit voltage. This defines the post-instability behavior of the system. The final region in Figure 2.9 is the pressure range at which again the system exhibits only one limit point, which is associated with the so-called primary limit point. The example of $P' = 9.6 \times 10^{-9}$ in Figure 2.8 belongs to this region.

Figure 2.10 shows how the critical deflections vary with the applied mechanical

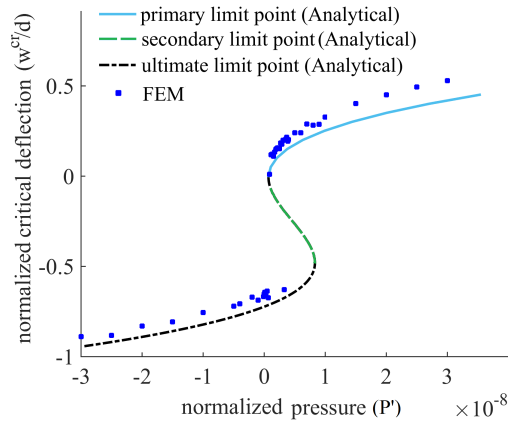


Figure 2.10: The critical deflections of the test case with thickness $h = 0.2\mu\text{m}$ and radius $R = 100\mu\text{m}$, as a function of the applied mechanical pressure.

pressure. It can be observed that the primary critical deflection varies between 0-50% of the initial gap size in the positive direction. At the ultimate pull-in point, the deflection of the plate is 65-73% of the initial gap size.

The snapping of the flat flexible electrode, when sweeping the applied voltage up and down, is an interesting phenomenon that could be used in electrostatically driven switches, sensors and actuators. However, as explained, only a certain range of pressure allows for existence of this behavior. The range of pressures allowing for snapping mainly depends on the mechanical properties of the flexible electrode and its dimensions (thickness and radius).

It should be noticed that snap-through is a dynamic process and when the flexible plate is snapping from an unstable to a stable state, it has nonzero velocity. However, since the load system is conservative, no dynamic consideration is required to assess stability. Instead, the total potential energy is a good criteria to ensure that the dynamic process does or does not lead to failure: *If the total potential energy at the primary limit point exceeds the potential at the ultimate limit point, the exceeding energy appears as kinetic energy causing an overshoot to occur.*

Figure 2.11 illustrates the required combination of differential pressure and thickness of the plate, in order to observe the snap-through phenomena. This graph is determined using both analytical and FEM solutions for the test case at hand. The good agreement between the solutions again demonstrates the accuracy of the analytical approximate.

As Figure 2.11 shows, if the pressure is too low, the primary limit point is not observed; and if the pressure is too high, then the primary limit voltage exceeds the ultimate limit voltage and the system would fail after reaching the first instability.

If the pressure is high enough, the ultimate and secondary limit points vanish and snap-back behavior will not be observed either. However, one can conclude from Figures 2.8 and 2.9 that the pressure range for having snap-through in loading is a subset of the range for having the snap-back in unloading. In fact, if the snapping in loading is observed, the occurrence of snap-back in unloading is certain.

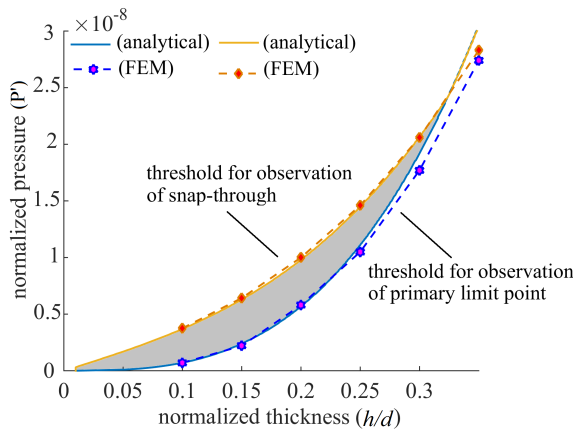


Figure 2.11: The pressure range in order to trigger the primary limit point and the snap-through, as a function of thickness of the flexible electrode, with $R = 100\mu\text{m}$.

Figure 2.12 shows the admissible combinations of the applied pressure and thickness for existence of snapping, for different radii of the electrode. As can be observed for smaller radii of the electrode (for example, $R/d = 40$ in Figure 2.12) a wide range of pressures might result in snap-through behavior. However, for larger electrodes the range of admissible pressures drops. It is interesting that the required thickness, resulting in snap-through, is always less than 33% of the gap size. For a thicker electrode, the primary instability, if observed, leads to direct pull-in.

Although the snap-through has been illustrated for constant pressures and a varying voltage, a similar behavior will be observed if the voltage is preserved and the pressure is varied. The midpoint deflection of the electrode as a function of the applied pressure, for different voltages, is provided in Figure 2.13. It can be observed from Figure 2.13 that for any voltage larger than zero, at least one limit point exists in

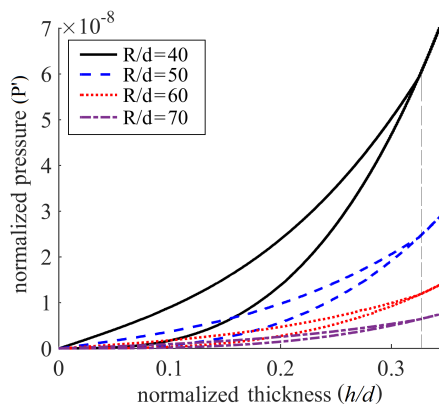


Figure 2.12: The pressure range in order to trigger the primary limit point and the snap-through, as a function of thickness of the flexible electrode, for different radii.

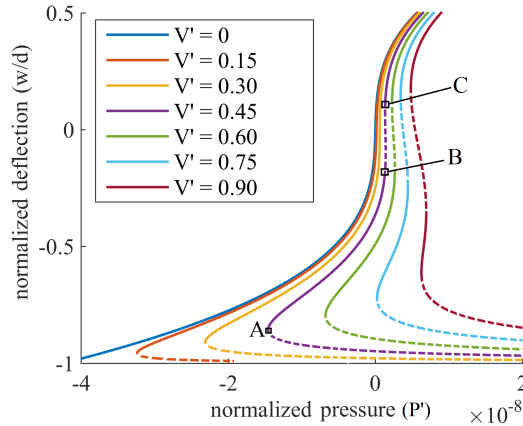


Figure 2.13: The midpoint deflection of the circular flexible electrode with thickness $h = 0.2\mu\text{m}$ and radius $R = 100\mu\text{m}$ as a function of the applied pressure. — stable equilibrium, - - - unstable equilibrium

the equilibrium path (e.g. Point A for $V'=0.45$). However, for larger voltages, two other limit points might appear. For example, in Figure 2.13, in the curve corresponding to $V'=0.45$, if we vary the pressure around Point B or C, the system snaps from a positive to a negative deflection, or *vice versa*. For very large voltages, on the other hand, varying the pressure over the limit points leads to pull-in of the system.

It is worth to point out that the compliance of the system to a differential pressure is minimum in case no voltage is applied to the capacitor. With a voltage increase the stiffness of the system drops, and finally at a critical voltage, the system allows for snap-through behavior. When snap-through occurs, the system has zero stiffness.

The snap-through and bi-stable behavior noticed for pressurized clamped electrodes, can be employed in sensing and actuation applications. This phenomenon can benefit from high sensitivity due to low compliance, and robustness and simplicity of pull-in voltage measurements.

Finally, we would like to note that the effective elastic properties of structures at nano scales are known to be strongly size-dependent. The classical continuum theory is inherently size in-dependent and hence, it cannot provide a good prediction for very small scales. For such length scales, size-dependent continuum theories that account for these scale effects should be utilized [27–31]. In this study, however, the hypothetical properties that are utilized for illustrating the results of the model are close to those of gold or aluminum thin films. For these two materials, scale effects are not significant at the thicknesses used in the present study [32–35]. Therefore, provided that we restrict the material to aluminum and gold or other similarly behaving materials, the classical continuum theory still can be employed. In order to use this formulation for design purposes for other materials, one should consider a thickness range at which the elastic coefficients for bulk materials can still be employed.

2.5. CONCLUSIONS

In this chapter, an analytical model was proposed for a circular flexible electrode in a parallel plate capacitor, while it is loaded with a differential pressure. Using this approximate solution, a stability analysis was performed on the effect of pressure on the critical voltage and deflection. In the proposed model, the geometrical non-linearity of the flexible electrode was taken into account.

The results suggest that a pressure can trigger additional limit points and an unstable solution branch to occur. The post-instability behavior after reaching the first limit point, depends on load parameters, thickness and radius of the electrode and the air gap. After the primary limit point, the system might snap to a new stable configuration, or, exhibit pull-in.

It is worth to mention here that when snap-through occurs, the system has very small stiffness, and is mechanically very compliant. This condition makes the system very suitable for sensing applications. In particular, the sensitivity of the limit voltages to the pressure can be employed to measure the pressure. To employ the primary limit point in sensing pressure, two techniques can be envisaged. The first is to subject the sensor to the measurand pressure and then ramp up the voltage to the primary limit voltage. This voltage can be detected by the sudden change in capacitance, and then the corresponding pressure can be calculated. The second possible method would be a binary mechanism for detecting a certain differential pressure. In this method, the voltage is kept *close* to the primary (or secondary) limit voltage of the target pressure. Then, if the pressure drops (or inclines) to less (or more) than the target pressure the system snaps. In this way, a very precise binary mechanism for pressure measurement will be achieved.

However, we stress here that even without observation of instability, the combination of positive pressure and electrostatic load on the flexible electrode results in a high compliance of the system, which may be very appealing for sensing applications.

Using the primary instability of pressurized electrodes in sensing or actuation can benefit from the robustness and simplicity of pull-in, and in addition, it can benefit from the snap-through behavior which prevents the system from failure.

It is emphasized, that the present study was based on the assumption of static loading of the capacitor. In actuation applications, however, an AC voltage might be applied to the system. Then, the frequency and amplitude of this AC voltage will also influence the bifurcation parameters. The effect of pressure on the dynamics of a circular micro electrode and instability analysis of such a structure will be studied in our future work.

REFERENCES

- [1] B. Sajadi, J. Goosen, and F. van Keulen, *Bi-stability of micro-plates: A sensitive mechanism for differential pressure measurements*, [Applied Physics Letters](#) **111**, 124101 (2017).
- [2] S. Krylov, B. R. Ilic, D. Schreiber, S. Seretensky, and H. Craighead, *The pull-in behavior of electrostatically actuated bistable microstructures*, [Journal of Micromechanics and Microengineering](#) **18**, 055026 (2008).
- [3] W.-M. Zhang, H. Yan, Z.-K. Peng, and G. Meng, *Electrostatic pull-in instability in mems/nems: A review*, [Sensors and Actuators A: Physical](#) **214**, 187 (2014).
- [4] G. W. Vogl and A. H. Nayfeh, *A reduced-order model for electrically actuated clamped circular plates*, in *ASME 2003 International Design Engineering Technical Conferences and Computers and Information in Engineering Conference* (American Society of Mechanical Engineers, 2003) pp. 1867–1874.
- [5] M. Khater, *Use of instabilities in electrostatic micro-electro-mechanical systems for actuation and sensing*, Thesis (2011).
- [6] K. M. Smyth, *Design and modeling of a PZT thin film based piezoelectric micro-machined ultrasonic transducer (PMUT)*, Thesis (2012).
- [7] W.-C. Chuang, H.-L. Lee, P.-Z. Chang, and Y.-C. Hu, *Review on the modeling of electrostatic mems*, [Sensors](#) **10**, 6149 (2010).
- [8] D. Elata and S. Abu-Salih, *Analysis of a novel method for measuring residual stress in micro-systems*, [Journal of Micromechanics and Microengineering](#) **15**, 921 (2005).
- [9] L.-D. Liao, P. C. Chao, C.-W. Huang, and C.-W. Chiu, *Dc dynamic and static pull-in predictions and analysis for electrostatically actuated clamped circular micro-plates based on a continuous model*, [Journal of Micromechanics and Microengineering](#) **20**, 025013 (2010).
- [10] H. Sadeghian, C.-K. Yang, H. Goosen, P. J. F. Van Der Drift, A. Bossche, P. J. F. French, and F. Van Keulen, *Characterizing size-dependent effective elastic modulus of silicon nanocantilevers using electrostatic pull-in instability*, [Applied Physics Letters](#) **94**, 221903 (2009).
- [11] H. Sadeghian, H. Goosen, A. Bossche, and F. van Keulen, *Application of electrostatic pull-in instability on sensing adsorbate stiffness in nanomechanical resonators*, [Thin Solid Films](#) **518**, 5018 (2010).
- [12] J. Lardiès, M. Berthillier, and M. L. Bellaredj, *Analytical investigation of the pull-in voltage in capacitive mechanical sensors*, in *SPIE Microtechnologies* (International Society for Optics and Photonics, 2011) pp. 80661N–80661N–10.
- [13] A. Sharma and P. J. George, *A simple method for calculation of the pull-in voltage and touch-point pressure for the small deflection of square diaphragm in mems*, [Sensors and Actuators A: Physical](#) **141**, 376 (2008).

- [14] P. M. Osterberg and S. D. Senturia, *M-test: A test chip for mems material property measurement using electrostatically actuated test structures*, *Microelectromechanical Systems, Journal of* **6**, 107 (1997).
- [15] J. Cheng, J. Zhe, X. Wu, K. R. Farmer, V. Modi, and L. Frechette, *Analytical and fem simulation pull-in study on deformable electrostatic micro actuators*, in *Technical Proc. of the International Conf on Modeling and Simulation of Microsystems, MSM* (2002) pp. 298–301.
- [16] G. Duan and K.-t. Wan, “pull-in” of a pre-stressed thin film by an electrostatic potential: A 1-d rectangular bridge and a 2-d circular diaphragm, *International Journal of Mechanical Sciences* **52**, 1158 (2010).
- [17] H. Sadeghian, C.-K. Yang, H. Goosen, A. Bossche, P. J. F. French, and F. Van Keulen, *Temperature sensitivity of silicon cantilevers’ elasticity with the electrostatic pull-in instability*, *Sensors and Actuators A: Physical* **162**, 220 (2010).
- [18] J. Sharma and A. Dasgupta, *Effect of stress on the pull-in voltage of membranes for mems application*, *Journal of Micromechanics and Microengineering* **19**, 115021 (2009).
- [19] S. Krylov and S. Seretensky, *Higher order correction of electrostatic pressure and its influence on the pull-in behavior of microstructures*, *Journal of Micromechanics and Microengineering* **16**, 1382 (2006).
- [20] A. Nabian, G. Rezazadeh, M. Haddad-derafshi, and A. Tahmasebi, *Mechanical behavior of a circular micro plate subjected to uniform hydrostatic and non-uniform electrostatic pressure*, *Microsystem Technologies* **14**, 235 (2008).
- [21] *Comsol multiphysics user guide (version 4.3 a)*, (2012).
- [22] M. Amabili, *Nonlinear vibrations and stability of shells and plates* (Cambridge University Press, 2008).
- [23] S. Timoshenko, S. Woinowsky-Krieger, and S. Woinowsky, *Theory of plates and shells*, Vol. 2 (McGraw-hill New York, 1959).
- [24] P. M. Osterberg, *Electrostatically actuated microelectromechanical test structures for material property measurement*, *Thesis* (1995).
- [25] R. Ansari, R. Gholami, V. Mohammadi, and M. F. Shojaei, *Size-dependent pull-in instability of hydrostatically and electrostatically actuated circular microplates*, *Journal of Computational and Nonlinear Dynamics* **8**, 021015 (2013).
- [26] K. Das and R. C. Batra, *Symmetry breaking, snap-through and pull-in instabilities under dynamic loading of microelectromechanical shallow arches*, *Smart Materials and Structures* **18**, 115008 (2009).
- [27] M. Asghari, *Geometrically nonlinear micro-plate formulation based on the modified couple stress theory*, *International Journal of Engineering Science* **51**, 292 (2012).

- [28] M. Rahaeifard, M. Kahrobaiyan, M. Asghari, and M. Ahmadian, *Static pull-in analysis of microcantilevers based on the modified couple stress theory*, *Sensors and Actuators A: Physical* **171**, 370 (2011).
- [29] M. Asghari, M. Kahrobaiyan, and M. Ahmadian, *A nonlinear timoshenko beam formulation based on the modified couple stress theory*, *International Journal of Engineering Science* **48**, 1749 (2010).
- [30] M. Asghari, M. Rahaeifard, M. Kahrobaiyan, and M. Ahmadian, *The modified couple stress functionally graded timoshenko beam formulation*, *Materials and Design* **32**, 1435 (2011).
- [31] B. Sajadi, H. Goosen, and F. van Keulen, *Capturing the effect of thickness on size-dependent behavior of plates with nonlocal theory*, *International Journal of Solids and Structures* (2017), [10.1016/j.ijsolstr.2017.03.010](https://doi.org/10.1016/j.ijsolstr.2017.03.010).
- [32] H. Espinosa and B. Prorok, *Size effects on the mechanical behavior of gold thin films*, *Journal of Materials Science* **38**, 4125 (2003).
- [33] H.-J. Oh, S. Kawase, I. Hanasaki, and Y. Isono, *Mechanical characterization of sub-100-nm-thick Au thin films by electrostatically actuated tensile testing with several strain rates*, *Japanese Journal of Applied Physics* **53**, 027201 (2014).
- [34] M. Haque and M. Saif, *Deformation mechanisms in free-standing nanoscale thin films: A quantitative in situ transmission electron microscope study*, *Proceedings of the National Academy of Sciences of the United States of America* **101**, 6335 (2004).
- [35] M. Haque and M. A. Saif, *Mechanical behavior of 30–50 nm thick aluminum films under uniaxial tension*, *Scripta Materialia* **47**, 863 (2002).

3

NONLINEAR DYNAMICS OF ELECTRICALLY ACTUATED MICRO-PLATES

Characterization of nonlinear behavior of the micro-mechanical components in MEMS plays an important role in their design process. Static deflection and stability of a micro-plate subjected to an electrostatic load was studied in the previous chapter. In this chapter, the nonlinear dynamic behavior and pull-in mechanisms, of an electrically actuated circular micro-plate are investigated. In order to study the periodic solutions, detect bifurcations and follow branches of the solution, the non-linear equation of motion is derived using a Lagrangian approach, and solved by a pseudo arc-length continuation and collocation technique. It is shown that, in the frequency response of the an electrically actuated micro-plate, both hardening and/or softening nonlinear responses could emerge depending on the applied DC voltage. The results indicate that the critical load parameters, namely DC and AC voltages and the excitation frequency, have a major influence on the pull-in characteristics of the micro-plate. In addition, they accurately show the decrease of the pull-in voltage due to dynamic loading.

Parts of this chapter have been published in the proceeding of ASME 2016 International Mechanical Engineering Congress and Exposition [1].

3.1. INTRODUCTION

In recent years, Micro-Electro-Mechanical Systems (MEMS) have received significant attention in diverse engineering applications due to their light weight, low production cost, and low energy consumption [2, 3]. Electrically actuated MEMS devices, typically employ a parallel-plate capacitor, in which one plate is actuated electrically and its motion is detected by capacitive changes [4, 5]. When an electric potential is applied to the capacitor, an attractive electrostatic load is induced between the two conductive electrodes, leading to deformation of the flexible electrode. When the potential fluctuates with time, a forced dynamic motion is induced in the system.

In the analysis of the motion of the flexible electrode, the electrostatic force is nonlinearly dependent on the deformation of the electrode. In addition, due to the deflection and rotation which might occur in the electrode, geometrical nonlinearity is also present in the elastic response of the structure. Therefore, the system might exhibit nonlinear global or local softening in its amplitude-frequency response curves. Particularly, at a critical combination of load parameters, i.e. DC and AC voltages and excitation frequency, the motion of the flexible electrode becomes unstable and it collapses on the stationary one. This phenomenon is known as *pull-in* [6, 7].

In most electrostatic MEMS devices, e.g. microphones or actuators, it is essential to avoid pull-in, since the contact between the two plates may cause failure [2, 7]. However, in sensing applications, pull-in is a unique characteristic of the sensor that can provide information on the mechanical and physical characteristics of the system [8–10]. In either way, in order to avoid or use the pull-in effect, an in-depth knowledge of the instability behavior and an accurate determination of the pull-in voltage of the structure is critically required.

Many studies have addressed the pull-in phenomenon and presented analytical or numerical estimation to predict the critical voltage at which this phenomenon occurs [6, 7, 11]. In static loading, this stability phenomenon appears as a ‘fold’ or a ‘limit point’ in the equilibrium curve of the system [10]. For dynamic loading, for example for micro-beam resonators, it has been shown that the dynamic pull-in can be triggered with dynamic instabilities due to nonlinear resonance. Therefore, it might occur at much smaller voltages as compared to static pull-in [12]. The dynamic pull-in instability of the micro-beam resonators might result from different mechanisms. For example, a cyclic fold in the frequency response function due to nonlinearities of the system, or, a transient jump between two or more coexisting stable branches of solutions due to a disturbance in the AC voltage can lead to pull-in [6].

A plate resonator, on the other hand, is a 2D structure which incorporates Poisson ratio effects and membrane stiffening effects. The static pull-in phenomenon of circular clamped plate-like electrodes has been investigated and formulated in many studies [7, 13, 14]. These studies are based on simplifying assumptions, such as small and one-dimensional deformation of the plate, or uniformity of the electrostatic load. However, to the best of our knowledge, there is no comprehensive solution which can model the static and dynamic pull-in of a circular plate with any thickness or radius.

In this chapter, the pull-in behavior of an electrically actuated circular micro-plate is studied. A simple shape function with three degrees of freedom is assumed

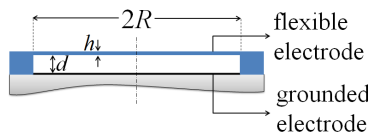


Figure 3.1: Schematic of the cross section of the capacitor with flexible, circular electrode.

for the forced vibration of the plate, and an energy approach based on Rayleigh-Ritz method is used to derive the approximate equation of motion. The obtained equation of motion accounts for geometrically nonlinear membrane effects of the flexible electrode. The non-uniformity of the electrostatic load due to the deformation of the electrode is another source of nonlinearity which is considered in this analysis.

In order to investigate the branches of periodic solutions and detect instabilities, a pseudo arc-length continuation and collocation technique are utilized. The results of this study show that both hardening and/or softening nonlinear responses could emerge, depending on the applied DC voltage. Also, the results indicate that the applied load parameters can significantly affect the pull-in characteristics of the micro-plate.

3.2. PROBLEM FORMULATION

A parallel plate capacitor with a very thin, circular, fully clamped plate as the flexible electrode is considered. The schematic model of this system is shown in Fig. 3.1. The radius of the plate is R and its thickness is h . The Young's modulus, Poisson ratio and the density of the plate are denoted to be E , ν and μ , respectively. The plate is suspended over a grounded electrode with similar radius and the initial gap between the two electrodes is d . An electric potential V consisting of a DC bias voltage V_{DC} , and an alternating AC voltage V_{AC} is applied to the electrodes:

$$V = V_{DC} + V_{AC} \sin(\Omega t), \quad (3.1)$$

where Ω is the excitation frequency.

Due to the alternating electrostatic field caused by the AC voltage, a forced dynamic motion is induced in the flexible electrode. The equations of motion for such a system can be obtained by using Hamilton's principle. In order to introduce the suitable global modes, the following simplifying assumptions are considered: First of all, the plate is modeled using von Kármán nonlinear plate theory which can account for moderate rotations and small deformations. Consequently, the displacement field is only derived for the mid-plane of the flexible plate, and, extended for other points. Second, due to radial symmetry in the geometry and the loads, the problem is assumed to be axisymmetric, i.e. displacement field and therefore, the global modes are only functions of radial coordinate r . In addition, we assume that the plate is excited around its fundamental frequency and therefore, the higher modes (including in-plane modes and the modes which would violate the axisymmetry) are not excited. Thus, the only appearing displacement components are radial (u) and trans-

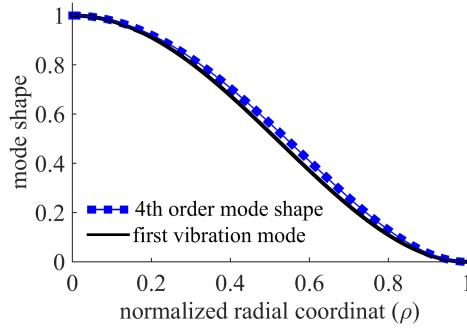


Figure 3.2: The normalized proposed global mode in comparison with the first mode shape of the clamped circular plate calculated with classical plate theory ($J_0(\kappa\rho) - \frac{J_0(\kappa)}{I_0(\kappa)}I_0(\kappa\rho)$, $\kappa = 3.19625$).

verse (w) components.

The clamping boundary condition forces these displacement components, and, also the first derivative of transverse displacement in the radial direction, to be equal to zero at the boundary. With these assumptions, the Timoshenko's approximate displacement field for uniformly loaded circular plates [15], is proposed to present radial (u) and transverse (w) displacement fields:

$$\begin{aligned} w &= q(t)d(1-\rho^2)^2, \\ u &= \xi_1(t)R\rho(1-\rho) + \xi_2(t)R\rho^2(1-\rho), \end{aligned} \quad (3.2)$$

where $\rho = r/R$ is the normalized radial coordinate, and, $q(t)$, $\xi_1(t)$ and $\xi_2(t)$ are dimensionless generalized coordinates, and unknown functions of time.

Notice that these shape functions can only mimic the first mode shape of a circular clamped plate (see Figure 3.2). Therefore, the proposed solution can only be applied if the system is excited around its fundamental frequency, and if that mode is not involved in an internal resonance with other modes of vibration. If such condition preserves, then other modes accidentally excited will decay with time due to the presence of damping [16].

Next, the total potential energy of the system can be calculated. The potential energy of the system consists of three terms concerned with the electrostatic potential (U_e), the potential associated with elastic deformation due to the bending (U_b) and the stretch (U_s) of the plate:

$$U = U_e + U_b + U_s. \quad (3.3)$$

Assuming the parallel-plate capacitor theory, the electrostatic potential can be formulated as [4]:

$$U_e = -\pi\epsilon V^2 R^2 \int_0^1 \frac{\rho d\rho}{d+w}. \quad (3.4)$$

where ϵ is the electric permittivity of the dielectric between the electrodes. Notice that in formulating the electrostatic potential (U_e), the local distance between two

electrodes ($d + w$) is employed and therefore, the formulation incorporates the non-uniformity of the electrostatic field due to the deflection of the flexible electrode.

Next, considering von Kármán's plate theory (moderate rotations), the potential associated with elastic deformation due to the bending (U_b) and the stretch (U_s) of the plate can be approximated [17]:

$$U_b = \frac{\pi D}{R^2} \int_0^1 \left(\left(\frac{\partial^2 w}{\partial \rho^2} \right)^2 + \left(\frac{1}{\rho} \frac{\partial w}{\partial \rho} \right)^2 + \left(\frac{2\nu}{\rho} \frac{\partial w}{\partial \rho} \frac{\partial^2 w}{\partial \rho^2} \right) \right) \rho d\rho, \quad (3.5a)$$

$$U_s = \frac{\pi E h}{(1-\nu^2)} \int_0^1 \left(\left(\frac{u}{\rho} \right)^2 + \left(\frac{\partial u}{\partial \rho} + \frac{1}{2R} \left(\frac{\partial w}{\partial \rho} \right)^2 \right)^2 + \frac{2\nu u}{\rho} \left(\frac{\partial u}{\partial \rho} + \frac{1}{2R} \left(\frac{\partial w}{\partial \rho} \right)^2 \right) \right) \rho d\rho. \quad (3.5b)$$

where $D = \frac{Eh^3}{12(1-\nu^2)}$ is the bending stiffness of the flexible plate. Notice that nonlinear membrane effects have been incorporated in the elastic potential. The kinetic energy of the system, neglecting in-plane inertia effects, is expressed as:

$$T = \pi \mu R^2 h \int_0^1 \dot{w}^2 \rho d\rho. \quad (3.6)$$

Hence, by substituting the displacement field from Eqn. 3.2 into Eqn. 3.4 - 3.6, the Lagrangian of the system, $L = T - U$, can be expressed in terms of generalized coordinates $L(q, \xi_1, \xi_2, \dot{q}, t)$:

$$L = \frac{1}{10} \pi \mu R^2 h d^2 (\dot{q}(t))^2 + \frac{\pi R^2}{2d} \epsilon(V(t))^2 F(q(t)) - \frac{32\pi d^2}{3R^2} D(q(t))^2 - \frac{12\pi R^2}{h^2} D(\alpha_1 \xi_1^2 + \alpha_2 \xi_2^2 + \alpha_3 \xi_1 \xi_2 - \alpha_4 \xi_1 (q(t))^2 \frac{d^2}{R^2} + \alpha_5 \xi_2 (q(t))^2 \frac{d^2}{R^2} + \alpha_6 (q(t))^4 \frac{d^4}{R^4}), \quad (3.7)$$

where, $\alpha_1 = 0.25$, $\alpha_2 = 0.1167$, $\alpha_3 = 0.3$, $\alpha_4 = 0.0677$, $\alpha_5 = 0.0546$, $\alpha_6 = 0.3053$, and,

$$F(q(t)) = \frac{\operatorname{atanh} \sqrt{-q(t)}}{\sqrt{-q(t)}} \quad \text{if } q(t) < 0, \quad (3.8a)$$

$$F(q(t)) = \frac{\operatorname{atan} \sqrt{q(t)}}{\sqrt{q(t)}} \quad \text{if } q(t) > 0. \quad (3.8b)$$

It is worth to notice that although $F(q)$ has a discontinuous definition, it is mathematically continuous and smooth around zero. Next, Hamilton's principle, can be reduced to Lagrange equations and can be written as:

$$\frac{\partial L}{\partial q} = \frac{d}{dt} \left(\frac{\partial L}{\partial \dot{q}} \right), \quad (3.9a)$$

$$\frac{\partial L}{\partial \xi_1} = \frac{\partial L}{\partial \xi_2} = 0. \quad (3.9b)$$

By solving Eqn. (3.9b) for ξ_1 and ξ_2 , one can find the following expressions analytically:

$$\begin{aligned}\xi_1(t) &= 1.185 \frac{d^2}{R^2} q(t)^2, \\ \xi_2(t) &= -1.750 \frac{d^2}{R^2} q(t)^2.\end{aligned}\quad (3.10)$$

3

In fact, Eqn. (3.10) describes the relation between the stretch of the plate and its transverse deflection, independent of the applied load. As a matter of fact, $\xi_1(t)$ and $\xi_2(t)$ from Eqn. 3.10 can be substituted into Eqn. 3.2. Hence, the degrees of freedom can be reduced to $q(t)$ only, while incorporating the in-plane deformation, as well. Next, the equation governing the transverse motion of the micro-plate can be obtained from Eqn. (3.9a):

$$\begin{aligned}\frac{1}{5} \mu R^2 h \ddot{q}(t) + \frac{64}{3} \left(\frac{1}{R}\right)^2 D \left(q(t) + \alpha_7 \left(\frac{d}{h}\right)^2 q(t)^3 \right) \\ - \epsilon (V(t))^2 \frac{R^2}{2d^3} \left(\frac{1}{2q(t)(1+q(t))} - \frac{F(q(t))}{2q(t)} \right) = 0,\end{aligned}\quad (3.11)$$

where, $\alpha_7 = 0.488$. Equation 3.11, as a matter of fact, describes the undamped motion of a circular clamped plate, electrically actuated around its fundamental frequency. In practice, however, the systems possesses some kind of energy dissipation mechanism or damping. By assuming a modal damping in the system, equation of motion can be augmented as:

$$\begin{aligned}\ddot{q}(t) + 2\zeta \omega_0 \dot{q}(t) + \omega_0^2 q(t) = \\ - \alpha_8 \left(\frac{d}{R}\right)^4 \frac{E}{\mu(1-\nu^2)} q(t)^3 + \alpha_9 \frac{\epsilon (V(t))^2}{\mu d h} \left(\frac{1}{2q(t)(1+q(t))} - \frac{F(q(t))}{2q(t)} \right).\end{aligned}\quad (3.12)$$

where, $\alpha_8 = 4.337$ and $\alpha_9 = 2.5$. The parameter $\omega_0 = \frac{10.328}{R^2} \sqrt{\frac{D}{\mu h}}$ is the natural frequency of the plate, and ζ is the assumed damping ratio. It is worth to note that the natural frequency ω_0 calculated with the proposed mode shape has only 1.1% error with respect to exact natural frequency of the plate calculated with classical plate theory, which shows the suitability of the proposed 4th global modes.

Equation 3.12, describes the damped motion of a circular clamped plate, electrically actuated around its fundamental frequency. In the right-hand side of this equation, two sources of nonlinearity are incorporated: (1) the cubic term due to the geometrical nonlinearity and, (2) the nonlinearity of electrostatic load.

Finally, Eqn. (3.12) will be solved for steady state periodic solutions. The numerical technique to solve this equation will be briefly described in the next section.

3.3. NUMERICAL SOLUTION OF THE EQUATION OF MOTION

In this section the numerical techniques to solve the equation of motion are outlined.

First, the highly nonlinear term in Equation 3.12, which appears due to the non-linearity of electrostatic field, is approximated with a polynomial. This approximation is performed with a method of polynomial regression:

$$\left(\frac{1}{2q(t)(1+q(t))} - \frac{F(q(t))}{2q(t)} \right) \approx \mathcal{O}(q(t)^n). \quad (3.13)$$

If the admissible region of $(-0.95, 0.5)$ is considered for $q(t)$, the results converge when $n > 11$. Using this fit, the discontinuity in the definition of $F(q(t))$ is eliminated from the equations.

Then, in order to obtain the periodic solutions and perform bifurcation analysis, a pseudo arc-length continuation and collocation scheme have been utilized [18]. In particular, a bifurcation analysis is carried out in three steps: (i) the continuation starts at zero AC and DC voltage, and considers the DC voltage as the first continuation parameter; (ii) Once the desired DC voltage is reached, the AC voltage is introduced as the second continuation parameter. The frequency is fixed far from the resonance. The AC voltage is incremented from the statically deflected configuration (due to the DC voltage) to a chosen AC voltage level. (iii) Finally, the bifurcation continues by considering the excitation frequency as the third continuation parameter to obtain frequency-amplitude responses.

The stability of the solution branches is determined using the Floquet multipliers. Floquet multipliers (λ_i) are analogous to the eigenvalues of Jacobian matrices of equilibrium points in static analysis and provide all the necessary information on the stability of the periodic solution. In fact, the periodic solution is stable only if all Floquet multipliers $|\lambda_i| < 1$, and unstable otherwise [17].

It is worth noting that in the absence of V_{AC} , there would be no dynamic load applied to the system and therefore, the static pull-in could be analyzed simply by taking the second derivative of the total potential energy with respect to q , and equating it to zero.

3.4. RESULTS AND DISCUSSION

The procedure outlined in the previous section has been applied to a micro-plate with the following properties: $E = 169 \text{ GPa}$, $\nu = 0.17$, $\mu = 2.328 \text{ gcm}^{-3}$, $h = 0.6 \mu\text{m}$, $R = 100 \mu\text{m}$ and $d = 2 \mu\text{m}$. Moreover, a damping ratio of $\zeta = 0.004$ is considered in the numerical simulation.

Here, three different test cases are studied: First, only a DC bias voltage is applied, i.e. $V_{AC} = 0$. As a result, the static pull-in is detected. In the second case, the flexible electrode is excited with a very small AC voltage, e.g. $V_{AC} = 0.01 \text{ V}$, together with a DC bias voltage. Third, a relatively small DC bias voltage and a large AC voltage are applied. As a result, the dynamic pull-in mechanisms in last two cases can be investigated and compared.

3.4.1. STATIC PULL-IN ($V_{AC} = 0$)

First, assume that the electric potential V only consists of a DC bias voltage. For this case, the equilibrium path of the midpoint of the flexible electrode is shown in Fig.

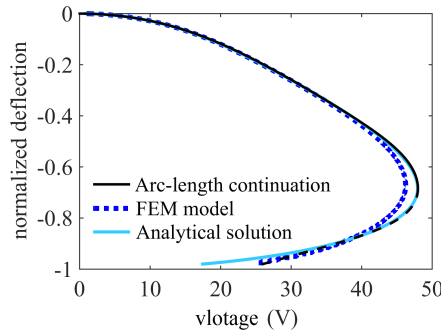


Figure 3.3: The deflection of the midpoint of the flexible electrode normalized with initial gap size (d) as a function of DC voltage, — stable solution, - - - unstable solution.

3.3. The presented curves are obtained by using three different methods: analytical solution of Eqn. (3.12), the numerical solution described in Section 3.3 considering $V_{AC} = 0$, and discretization of the full 3D problem using the commercial finite element software COMSOL. As can be seen, the axisymmetric 3 DOF solution presented in this chapter is in a good agreement with the detailed FEM analysis of the problem.

It can be observed that the midpoint deflection of the flexible electrode monotonically increases with the applied DC voltage until the system reaches a saddle-node bifurcation. At this point, the system becomes unstable, and a small perturbation leads to total failure or pull-in. The static pull-in voltage of this test case is $V_p^S = 47.93$ V and the critical deflection of the mid-point is 0.68 of the gap size. Consequently, to ensure the stability, the circular micro-plate should be designed to operate below this voltage. It is worth noting that the proposed solution allows for calculation of the critical displacement as a function of the specifications of the capacitor.

3.4.2. DYNAMIC PULL-IN ($V_{AC} \ll V_{DC}$)

Next, a fixed AC voltage of 0.01 V is applied and the effect of different DC voltages is studied. The frequency response curves of the forced vibrations of the electrode around its first resonant frequency are shown in Fig. 3.4. These curves are obtained for different applied DC voltages. As it can be observed in Fig. 3.4-a, for relatively small DC voltages (i.e. $V_{DC} < 40$ V) the vibrations are almost linear, i.e. no nonlinear hardening or softening is observed in the resonance and the frequency response function of the system. However, the resonance frequency of the system has a shift (global hardening) due to the geometrical stiffness caused by the static deflection of the electrode.

For larger DC Voltages, on the other hand, the frequency response curves exhibit a nonlinear behavior (see Fig. 3.4-b). When approaching the static pull-in voltage ($V \rightarrow 47.93$ V), both global and local nonlinear softening behaviors are observed in the system and finally, the resonance frequency of the system tends to zero. At this situation, the system becomes unstable and pull-in occurs.

The change of the frequency associated with the peak in nonlinear resonance

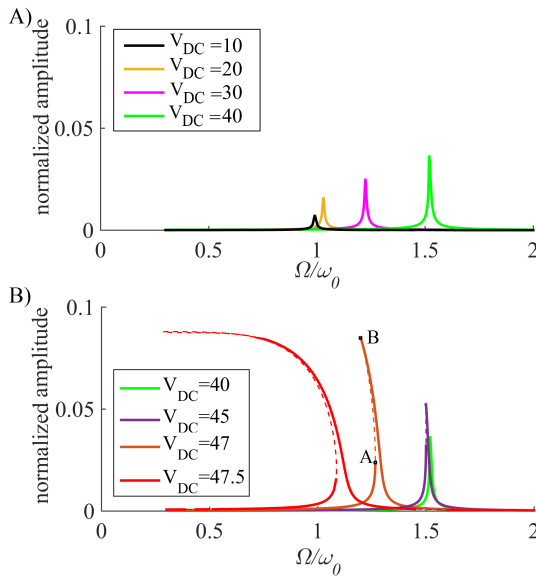


Figure 3.4: The amplitude of vibrations normalized with initial gap size (d) for $V_{AC} = 0.01$ V, and DC voltage of A) below the static pull-in voltage and B) close to static pull-in voltage, — stable solution, - - - unstable solution.

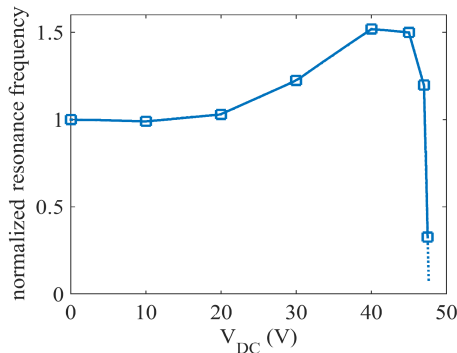


Figure 3.5: The frequency associated with the peak in nonlinear resonance normalized with the fundamental frequency as a function of DC voltage for $V_{AC} = 0.01$ V. — stable solution, - - - unstable solution.

versus the applied DC voltage is shown in Fig. 3.5. This figure indicates initially a hardening which changes to softening, down to complete failure (i.e. zero resonance frequency at critical DC voltage).

It is worth remarking that, when a relatively high DC voltage is applied to the system, an unstable solution branch emerges in its frequency response curve. Therefore, at points where the stable and unstable solution branches coincide (e.g. points A and B for $V_{DC} = 47$ V in Fig. 3.4-b), a saddle point bifurcation is noticed. If we sweep

the frequency over the saddle points, the system will most probably jump from one stable branch to the other one. However, it might also become unstable, leading to pull-in [6]. Indeed in such cases, the transient dynamics of the system would determine whether the system settles at a stable orbit, or it fails, i.e. pulls in.

3.4.3. DYNAMIC PULL-IN ($V_{DC} \ll V_p^S$)

3

In this case, a fixed and relatively small DC voltage of 30 V is applied, and the dynamic behavior of the system with different AC voltages is studied. The frequency response curves of the flexible electrode around its first resonance are shown in Fig. 3.6.

Notice that the applied DC voltage leads to a static deflection of the plate, and this induces a geometrical stiffness. Therefore, even when actuating with a small AC voltage, a shift or a global hardening is noticed in the frequency response curves of the system (see $V_{AC} = 0.01$ V in Fig. 3.6-a).

Exciting this system with a small AC force leads to a stable periodic motion around the static configuration. However, when the AC voltage is increased, the vibration of the electrode allows for lower geometrical stiffness and therefore, a local nonlinear softening is observed (see $V_{AC} = 0.10$ V in Fig. 3.6-a). If the AC voltage is increased further, both nonlinear softening and hardening can emerge in the system (see $V_{AC} = 0.25$ V in Fig. 3.6-a). In the case of nonlinear softening or hardening, one or more unstable solution branches are observed in the frequency response curve of the system. Similar to the previous case, sweeping the actuation frequency over the saddle points where the stable and unstable solution branches coincide, might result in an instability leading to pull-in.

If the AC voltage is increased further (see $V_{AC} = 0.35$ V in Fig. 3.6-b), in addition to critical saddle-node bifurcations (e.g. A, B, C, D and E), the solution goes through a period-doubling bifurcation (e.g. point F). This bifurcation is detected using the Floquet multipliers. When any of the Floquet multipliers has only a real value of -1 , a period doubling bifurcation takes place. In such a bifurcation, a new limit cycle emerges from an existing limit cycle, and the period of the new limit cycle is twice that of the old one. This phenomenon usually leads to a transition to chaos and at the end, failure of the system. In Fig. 3.6-b, if we sweep over point F from right to left, the system loses stability upon continuously passing through bifurcation points and, finally, fails.

The change of the frequency associated with the peak in nonlinear resonance as a function of the applied AC voltage is shown in Fig. 3.7. As can be seen in Fig. 3.7, for very small AC voltages, the resonance frequency of the system is shifted with respect to the natural frequency of the system. This shift, as mentioned before, is due to the geometric stiffness caused by the static deflection. At higher AC voltages, the resonance frequency changes due to large amplitudes and the nonlinear vibration around the static deflection. Finally, at higher AC voltages ($V_{AC} > 0.35$ V), after the occurrence of the period doubling, the resonance frequency suddenly drops. The resonance of the system after period doubling is located in an unstable solution branch, and therefore, is physically unreachable.

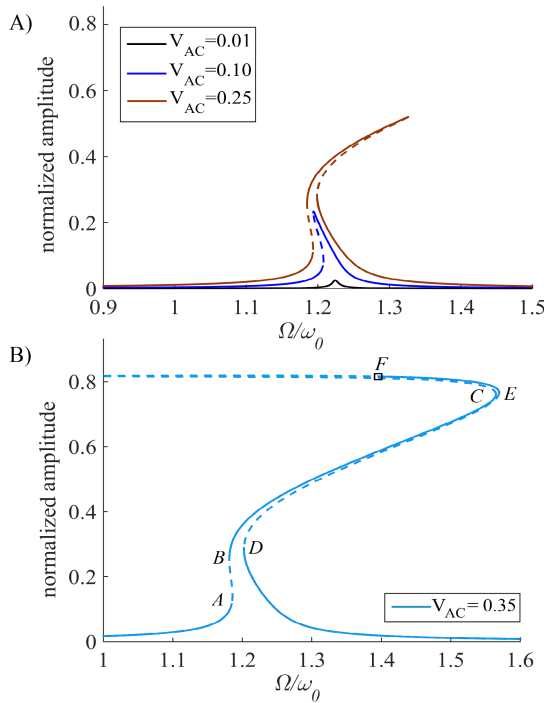


Figure 3.6: The amplitude of vibrations normalized with initial gap size (d) for $V_{DC} = 30$ V, A) relatively low AND B) relatively high AC voltages. — stable solution, - - - unstable solution.

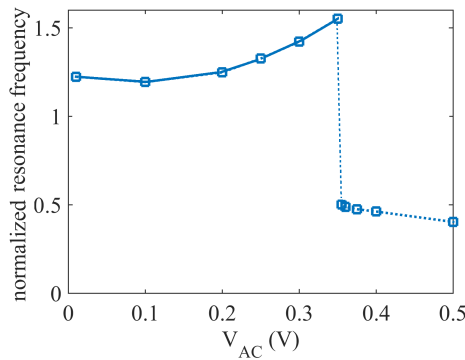


Figure 3.7: The frequency associated with the peak in nonlinear resonance normalized with the fundamental frequency, as a function of AC voltage for $V_{DC} = 30$ V. — stable solution, - - - unstable solution. — stable solution, - - - unstable solution.

3.5. CONCLUSION

In this study, the dynamic pull-in behavior of an electrically actuated circular micro-plate has been studied. To describes the dynamic motion of the device, using an

energy approach, a one DOF equation of motion in the transverse direction has been established. It should be reminded that the proposed method incorporates shape functions which can only mimic the first mode shape in the clamped plate. Therefore, this solution can only be applied if the system is excited around its fundamental frequency.

Moreover, three different examples of electrostatic loading of a circular micro-plate were studied. The results revealed distinct mechanisms of electrostatic instability which should be taken into account in the design of MEMS actuators and switches. The critical load parameters, DC and AC voltages and also the excitation frequency, have a major influence on the pull-in characteristics of the micro-plate.

The first mechanism, or static pull-in, is a saddle point bifurcation in equilibrium path of the system. After this point, the system loses stability and static pull-in occurs. The second mechanism of pull-in occurs when a system is excited with a small AC load. In such case, the pull-in occurs at a critical combination of load parameters, namely when the summation of DC and AC voltages approaches the static pull-in voltage. Then the resonance frequency of the system, due to global and local softening, tends to zero, and, the system fails.

The third mechanism of pull-in occurs when a system is excited with a relatively low AC and DC. In that case, nonlinear softening and hardening might emerge in frequency response curves of the system which lead to the presence of unstable solution branches. When the system approaches saddle points, where the stable and unstable solution branches coincide, it might lose stability leading to pull-in. Finally, the last mechanism occurs when a system is excited with a relatively high AC. In that case, the system might exhibit a period doubling bifurcation, which leads to symmetry breaking (which cannot be detected by the proposed method) and failure.

In conclusion, all different mechanisms of dynamic pull-in phenomenon, which might be noticed in circular MEMS devices and resonators, should be taken into account in their design. The proposed approximate solution can be used to predict the unstable voltages or frequencies prone to pull-in. Although the proposed global modes have a limitation in describing the displacement of the plate, this solution is simple, computationally fast and very robust for detecting the instabilities.

REFERENCES

- [1] B. Sajadi, F. Alijani, H. Goosen, and F. van Keulen, *Static and dynamic pull-in of electrically actuated circular micro-membranes*, in *ASME 2016 International Mechanical Engineering Congress and Exposition* (American Society of Mechanical Engineers) pp. V04AT05A030–V04AT05A030.
- [2] W.-C. Chuang, H.-L. Lee, P.-Z. Chang, and Y.-C. Hu, *Review on the modeling of electrostatic mems*, *Sensors* **10**, 6149 (2010).
- [3] J. Sharma and A. Dasgupta, *Effect of stress on the pull-in voltage of membranes for mems application*, *Journal of Micromechanics and Microengineering* **19**, 115021 (2009).
- [4] W.-M. Zhang, H. Yan, Z.-K. Peng, and G. Meng, *Electrostatic pull-in instability in mems/nems: A review*, *Sensors and Actuators A: Physical* **214**, 187 (2014).
- [5] S. Chowdhury, M. A. Ahmadi, and W. C. Miller, *Pull-in voltage calculations for mems sensors with cantilevered beams*, in *IEEE-NEWCAS Conference, 2005. The 3rd International* (IEEE, 2005) pp. 143–146.
- [6] A. H. Nayfeh, M. I. Younis, and E. M. Abdel-Rahman, *Dynamic pull-in phenomenon in mems resonators*, *Nonlinear dynamics* **48**, 153 (2007).
- [7] L.-D. Liao, P. C. Chao, C.-W. Huang, and C.-W. Chiu, *Dc dynamic and static pull-in predictions and analysis for electrostatically actuated clamped circular micro-plates based on a continuous model*, *Journal of Micromechanics and Microengineering* **20**, 025013 (2010).
- [8] H. Sadeghian, C.-K. Yang, H. Goosen, P. J. F. Van Der Drift, A. Bossche, P. J. F. French, and F. Van Keulen, *Characterizing size-dependent effective elastic modulus of silicon nanocantilevers using electrostatic pull-in instability*, *Applied Physics Letters* **94**, 221903 (2009).
- [9] H. Sadeghian, C.-K. Yang, H. Goosen, A. Bossche, P. J. F. French, and F. Van Keulen, *Temperature sensitivity of silicon cantilevers' elasticity with the electrostatic pull-in instability*, *Sensors and Actuators A: Physical* **162**, 220 (2010).
- [10] D. Elata and S. Abu-Salih, *Analysis of a novel method for measuring residual stress in micro-systems*, *Journal of Micromechanics and Microengineering* **15**, 921 (2005).
- [11] K. Das and R. C. Batra, *Symmetry breaking, snap-through and pull-in instabilities under dynamic loading of microelectromechanical shallow arches*, *Smart Materials and Structures* **18**, 115008 (2009).
- [12] J. Seeger and B. E. Boser, *Charge control of parallel-plate, electrostatic actuators and the tip-in instability*, *Microelectromechanical Systems, Journal of* **12**, 656 (2003).

- [13] P. M. Osterberg and S. D. Senturia, *M-test: A test chip for mems material property measurement using electrostatically actuated test structures*, *Microelectromechanical Systems, Journal of* **6**, 107 (1997).
- [14] J. Lardiès, M. Berthillier, and M. L. Bellaredj, *Analytical investigation of the pull-in voltage in capacitive mechanical sensors*, in *SPIE Microtechnologies* (International Society for Optics and Photonics, 2011) pp. 80661N–80661N–10.
- [15] S. Timoshenko, S. Woinowsky-Krieger, and S. Woinowsky, *Theory of plates and shells*, Vol. 2 (McGraw-hill New York, 1959).
- [16] A. H. Nayfeh and D. T. Mook, *Nonlinear oscillations* (John Wiley & Sons, 2008).
- [17] M. Amabili, *Nonlinear vibrations and stability of shells and plates* (Cambridge University Press, 2008).
- [18] E. J. Doedel, A. R. Champneys, T. F. Fairgrieve, Y. A. Kuznetsov, B. Sandstede, and X. Wang, *Auto97*, (1998).

4

EFFECTS OF PRESSURE ON STABILITY OF ELECTRICALLY ACTUATED MICRO-PLATES

In previous chapters, the nonlinear static and dynamic response of an electrically actuated micro plate was addressed. Moreover, the effects of a differential pressure on this nonlinear response was studied in Chapter 2. In this Chapter, the effect of a differential pressure on nonlinear dynamics and the stability of an electrically actuated circular micro-plate is studied. For this purpose a reduced order model based on an energy approach is employed to analyze the motion of the micro-plate. The results of this study indicate that dynamics of an electrically actuated micro-plate, in the presence of differential pressure, significantly differ from those under purely electrostatic loads. In addition, it is shown that the presence of a differential pressure can have a major influence on the stability of the micro-plate which should be taken into account in the design process.

4.1. INTRODUCTION

Electrically actuated Micro-Electro-Mechanical Systems (i.e. MEMS) are increasingly being used in diverse engineering applications, such as sensors and actuators [1, 2]. Electrostatic instability is one of the main features of these devices, which for many applications is considered as a failure, and thus, avoided. Though, in electrostatic switches and sensors, for example, electrostatic instability is often employed as the main driving mechanism and therefore, it is intentionally triggered [3–5]. In either way, in order to avoid or to exploit the electrostatic instability, a good understanding of this phenomena is essential to obtain a high performance MEMS device.

Electrically actuated micro devices typically employ a parallel-plate capacitor, in which at least one electrode is flexible. When an electric potential is applied to the capacitor, an attractive electrostatic load is induced between the two electrodes, leading to the deformation of the flexible one. When the potential fluctuates with time, a forced dynamic motion is induced in the system, which can be detected by capacitive changes of the system [6, 7].

The electrostatic load driving the motion of the flexible electrode is a function of the applied bias (DC) and alternating (AC) voltages, and the distance between the two electrodes. Consequently, it also depends nonlinearly on the electrode deflection. In case of finite defections of the electrode, geometrical nonlinearity also appears in the elastic potential of the structure. As a result, the system might exhibit nonlinear softening or hardening. Particularly, at a critical combination of DC and AC voltages and also the excitation frequency, the motion of the flexible electrode becomes unstable, and then, the micro-plate fall on to the stationary one. This phenomenon is known as *pull-in* [8, 9].

If the applied electric potential is a static DC voltage, the deformation of the electrode is static as well. In that case, the only load parameter in assessment of stability is the applied DC voltage, and the critical stability appears as a ‘fold’ or a ‘limit point’ in the response of the system. Many studies have addressed the static pull-in phenomenon, and proposed analytical or numerical methods to estimate the pull-in voltage [7, 9–13]. A literature survey on this topic has been carried out in Ref. [6]. It has been shown that the critical voltage and deflection of the flexible electrode depend on the material properties, geometry and dimensions of the flexible electrode, and the initial gap size between the two electrodes. Particularly, for circular plate-like electrodes, the critical deflection in static pull-in varies between 51-71% of the initial gap between the electrodes, depending only on the thickness of the structure [14].

In electrostatic actuators, in which the applied electric potential includes a dynamic AC component, the deflection of the electrode will be dynamic as well. In studying the stability of such a system, in addition to the DC voltage, the frequency and the amplitude of the AC voltage play influential roles. Many studies have addressed the dynamic pull-in phenomenon, and proposed analytical or numerical methods to estimate the pull-in voltage [8, 9, 15]. It has been reported that for micro resonators, the dynamic pull-in can be triggered by dynamic instabilities, and therefore, it might occur at much lower voltages compared to the static pull-in voltage [16]. The dynamic pull-in can be triggered by different mechanisms [8]: (i) a cyclic fold in the frequency response function due to nonlinearities of the system, (ii)

a transient jump between two or more coexisting stable solution branches due to a disturbance in the AC voltage or, (iii) a period-doubling bifurcation.

The dynamic pull-in threshold (i.e. the critical deflection, and the critical combination of DC and AC voltages) are shown to be highly influenced by any mechanical load applied to the micro-mechanical component. For example, the effects of van der Waals or Casimir forces between the electrodes on the dynamic behavior and stability of the micro/nano plates have been reported [17–20]. Moreover, the effect of a uniform differential pressure on the linear resonance frequency of an electrically actuated circular micro-plate has been observed [21]. In practice, the additional mechanical loads, such as a differential pressure, are very common in MEMS applications, and insufficient attention for the effect of these factors on pull-in threshold can result in decreasing the reliability of the MEMS device. Therefore, in this chapter, we investigate nonlinear vibrations and stability of an electrically actuated circular micro-plate when subjected to a differential pressure. The pressure is considered to be positive when opposing the electrostatic load, and negative otherwise.

A Lagrangian approach is used to obtain a reduced-order model and to derive the approximate equations of motion. In the proposed model, nonlinear stretching, and non-uniformity and nonlinearity of the electrostatic load due to finite deflection of the flexible plate are considered. It shall be mentioned that reduced-order modeling of electrically actuated micro-plates has been performed in the literature following different approaches [22–26]. However, the distinguishing feature of the present model is its simplicity while maintaining the accuracy. In this study, as a consequence of using a proper set of polynomials as the basis functions, a simple and yet accurate equation of motion is obtained which is more versatile for performing bifurcation analysis as compared to the alternative available models.

In order to investigate the branches of periodic solutions and detect instabilities, a pseudo arc-length continuation and collocation technique are utilized. Based on the proposed solution, the effects of load parameters, namely DC and AC driving voltages, the excitation frequency, and particularly the differential pressure on the stability of the system are explored. The results of this study show that the applied load parameters, can significantly affect the dynamic characteristics, resonance frequency, and the pull-in mechanisms of a micro-plate. The method presented in this chapter is shown to be simple, easy to use, fast, and accurate enough to be used as a design tool for MEMS devices.

4.2. PROBLEM FORMULATION

In this section we propose a model for the harmonic motion of a parallel plate capacitor with a very thin, circular, fully clamped plate as the flexible electrode. The schematic model is shown in Figure 4.1. The radius of the plate is R and its thickness is h . The plate is isotropic and homogeneous and its Young's modulus, Poisson's ratio and density are E , ν and μ , respectively. The plate is suspended over a grounded electrode having the same radius, and the initial gap between the two electrodes is d . An electric potential V consisting of a DC bias voltage and an alternating AC voltage is applied to the electrodes. The flexible electrode is loaded with a differential pressure P , positive outward (in the opposing direction the electrostatic load).

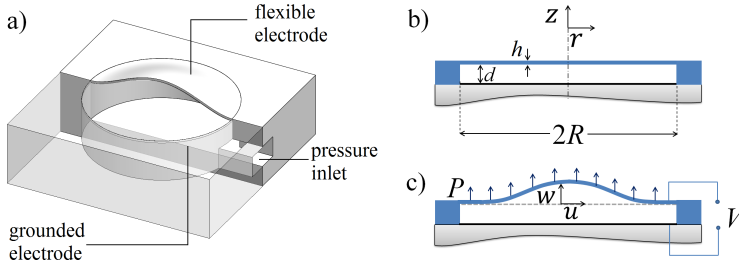


Figure 4.1: Schematic of (a) a capacitor with flexible, circular electrode subjected to a differential pressure, its cross section in (b) undeformed and (c) deformed configurations due to the electrostatic load and the differential pressure.

4

Due to the alternating electrostatic field induced by the AC voltage, a forced dynamic motion is induced in the system. We use a reduced-order model and a Lagrangian approach to obtain the equations of motion for such a system. In order to introduce suitable global modes, the following simplifying assumptions are considered: first, the plate is modeled by nonlinear von Kármán plate theory for thin plates, which accounts for finite deflections and moderate rotations [27]. Second, due to radial symmetry in the geometry and the loads, the problem is assumed axisymmetric [28]. In fact, we assume that the plate is excited around its fundamental frequency, and the first mode is not involved in an internal resonance with other modes of vibration. Hence, other modes (including the anti-symmetric modes), even if accidentally excited, will decay with time due to the presence of damping [29]. Therefore, the only existing displacement components are radial (u) and transverse (w) components, which are functions of the radial coordinate (r), only.

Considering that the plate is clamped around its circumference, the following approximate displacement field is used to present the radial (u) and the transverse (w) displacements:

$$w = q(t)d\Phi_0(\rho), \quad (4.1)$$

$$u = \sum_{i=1}^N \xi_i(t)R\Phi_i(\rho), \quad (4.2)$$

where $\rho = r/R$ is the normalized radial coordinate, and, the functions $\Phi_0(\rho)$ and $\Phi_i(\rho)$ are the global modes and are defined as follows:

$$\Phi_0(\rho) = (1 - \rho^2)^2, \quad (4.3)$$

$$\Phi_i(\rho) = \rho^i(1 - \rho), \quad (i = 1, \dots, N). \quad (4.4)$$

The function $\Phi_0(\rho)$ is a 4th order polynomial representation of the first linear mode shape of the plate (see Figure 4.2), and $\Phi_i(\rho)$ are capable of reflecting the associated

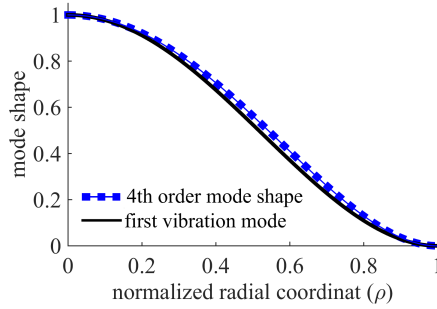


Figure 4.2: The normalized proposed global mode in comparison with the first linear mode shape of a clamped circular plate calculated with classical plate theory ($J_0(\kappa\rho) - (\frac{J_0(\kappa)}{J_0(\kappa)})I_0(\kappa\rho)$, $\kappa = 3.19625$).

in-plane displacement [30]. The functions $q(t)$ and $\xi_i(t)$ are dimensionless, time-dependent generalized coordinates, and $q(t)$ is physically restricted to $-1 < q(t)$. The proposed displacements are admissible functions satisfying the geometric boundary conditions:

$$w = u = \frac{\partial w}{\partial \rho} = 0 \quad \text{at} \quad \rho = 1, \quad (4.5)$$

the continuity condition of $\Phi_i = 0$ at $\rho = 0$, and the finitude of the resulted Cauchy strain components at $\rho = 0$. The validity and accuracy of the chosen mode shapes will be discussed in Section 4.4.

The total potential energy of the system consists of four terms: the potential associated with elastic deformation due to bending (U_b) and stretching (U_s) of the plate, the electrostatic potential (U_e), and finally, the potential associated with the mechanical pressure (W);

$$U = U_b + U_s + U_e - W. \quad (4.6)$$

The potential associated with elastic deformation can be approximated by ($U_b + U_s$) [27]:

$$U_b = \frac{\pi D}{R^2} \int_0^1 \left(\left(\frac{\partial^2 w}{\partial \rho^2} \right)^2 + \left(\frac{1}{\rho} \frac{\partial w}{\partial \rho} \right)^2 + \left(\frac{2\nu}{\rho} \frac{\partial w}{\partial \rho} \frac{\partial^2 w}{\partial \rho^2} \right) \right) \rho d\rho, \quad (4.7)$$

$$U_s = \frac{\pi E h}{(1-\nu^2)} \int_0^1 \left(\left(\frac{u}{\rho} \right)^2 + \left(\frac{\partial u}{\partial \rho} + \frac{1}{2R} \left(\frac{\partial w}{\partial \rho} \right)^2 \right)^2 + \frac{2\nu u}{\rho} \left(\frac{\partial u}{\partial \rho} + \frac{1}{2R} \left(\frac{\partial w}{\partial \rho} \right)^2 \right) \right) \rho d\rho,$$

where $D = \frac{Eh^3}{12(1-\nu^2)}$ is the bending stiffness of the flexible plate.

Since the deflection of the plate due to mechanical and electrostatic loads is very small compared to its lateral dimensions, the loads on the plate are assumed to be

always perpendicular to its un-deformed surface [31]. This is, in fact, consistent with the moderate rotation assumption. Therefore, the parallel-plate capacitor theory can be employed and the electrostatic potential can be formulated as [6]:

$$U_e = -\pi\epsilon V^2 R^2 \int_0^1 \frac{\rho d\rho}{d+w}, \quad (4.8)$$

where ϵ is the electric permittivity of the dielectric between the electrodes. Notice that in formulating the electrostatic potential (U_e), the local distance between the electrodes ($d+w$) is employed to calculate the electrostatic potential. Finally, the potential associated with the pressure can be calculated as follows:

$$W = 2\pi P R^2 \int_0^1 w \rho d\rho. \quad (4.9)$$

Recall that the in-plane displacement and its time derivative are much smaller than the transverse displacement and velocity. Hence, in calculating the kinetic energy, the contribution of the in-plane velocity is in orders of magnitude lower than the transverse velocity ($\dot{\xi}_i(t)^2 \ll \dot{q}(t)^2$) and thus, it can be neglected. Consequently, the kinetic energy of the system can be expressed as:

$$T = \pi\mu R^2 h \int_0^1 \dot{w}^2 \rho d\rho. \quad (4.10)$$

By substituting Equations (4.1) and (4.2) into (4.8)–(4.10), the Lagrangian of the system can be obtained analytically and expressed in terms of the generalized coordinates $L(q, \xi_i, \dot{q}, t)$.

$$L = T - (U_e + U_b + U_s - W) \quad (4.11)$$

Next, Lagrange equations can be employed:

$$\frac{d}{dt} \left(\frac{\partial L}{\partial \dot{q}} \right) - \frac{\partial L}{\partial q} = 0, \quad (4.12)$$

$$\frac{\partial L}{\partial \xi_i} = 0 \quad i = 1, \dots, N. \quad (4.13)$$

Equation (4.13) yields a set of N nonlinear algebraic equations in terms of ξ_i ($i = 1, \dots, N$) and q . By solving this set of equations for ξ_i , one can find all ξ_i analytically as:

$$\xi_i(t) = \xi_i(q(t)) \quad i = 1, \dots, N. \quad (4.14)$$

In fact, Equation (4.14) would describe the relation between the plate stretching and its transverse deflection, independent of the applied loads. Hence, the degrees of freedom can be reduced to $q(t)$ only, while incorporating the in-plane displacement and its associated stiffness which is a major contributor to nonlinearity. This simple form appears as a result of neglecting the contribution of $\dot{\xi}_i(t)$ in the inertia. Next, the

equation governing the transverse motion of the micro-plate can be obtained from Equation (4.12):

$$\begin{aligned} \ddot{q}(t) + 2\zeta\omega_0\dot{q}(t) + \omega_0^2q(t) = & \\ & - \alpha_1 Dq(t)^3 \\ & + \alpha_2 V(t)^2 \left(\frac{1}{2q(t)(1+q(t))} - \frac{F(q(t))}{2q(t)} \right) \\ & - \alpha_3 P, \end{aligned} \quad (4.15)$$

It should be reminded here that in practice, the system will have energy dissipation, and ζ is the modal damping that has been added to the equation of motion to account for this dissipation. Furthermore,

$$\begin{aligned} F(q(t)) &= \frac{\operatorname{atanh}\sqrt{-q(t)}}{\sqrt{-q(t)}} & \text{if } q(t) < 0, \\ F(q(t)) &= 1 & \text{if } q(t) = 0, \\ F(q(t)) &= \frac{\operatorname{atan}\sqrt{q(t)}}{\sqrt{q(t)}} & \text{if } q(t) > 0. \end{aligned} \quad (4.16)$$

Note that at $q(t) = 0$, the function $F(q(t))$ is described as unity to maintain the *continuity* and *smoothness* of this function at zero. The parameter α_1 is the coefficient of geometric nonlinearity, and its convergence and accuracy is determined by in-plane degrees of freedom N in Equation (4.2). The parameter α_2 is the coefficient of the nonlinear electrostatic force, and parameter α_3 is the projection of the pressure to the assumed mode shape in transverse direction:

$$\begin{aligned} \alpha_2 &= 2.50 \frac{\epsilon}{\mu h d^3}, \\ \alpha_3 &= 1.67 \frac{1}{\mu h d}. \end{aligned} \quad (4.17)$$

The parameter ω_0 is the natural frequency of the circular clamped plate and is equal to $\frac{10.32}{R^2} \sqrt{\frac{D}{\mu h}}$. It is worth noting that this amount is less than 1% different from the natural frequency of the plate calculated with classical plate theory.

The electric potential $V(t)$ in Equation (4.15) consists of a DC bias voltage V_{DC} , and an alternating AC voltage V_{AC} with the excitation frequency Ω :

$$V = V_{DC} + V_{AC} \sin(\Omega t). \quad (4.18)$$

Thus, equation (4.15) describes the nonlinear axi-symmetric motion of a circular clamped plate, loaded with a uniform differential pressure and electrically actuated by its fundamental mode.

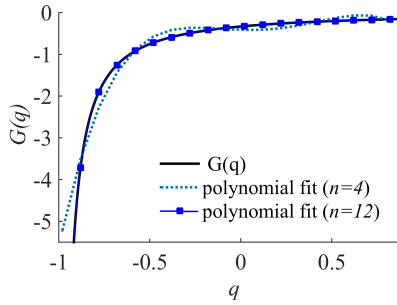


Figure 4.3: Approximation of the nonlinear electrostatic load ($G(q)$). A polynomial of order 12 has a good match with the exact function.

4.3. SOLUTION METHODOLOGY

In order to solve Equation (4.15), first, the nonlinear term associated with the electrostatic field is approximated by a polynomial function:

$$\begin{aligned}
 G(q) &= \frac{1 - (q+1)F(q)}{2q(1+q)} \\
 &\simeq \sum_{i=0}^n A_i q^i + \mathcal{O}(q^{n+1}), \quad \text{if } q \neq 0, \\
 G(q) &= -\frac{1}{3} \quad \text{if } q = 0,
 \end{aligned} \tag{4.19}$$

where coefficients A_i are obtained by using the least squares technique (polynomial regression) for $-1 < q < 1$. Similar to $F(q)$, $G(q)$ is described at $q = 0$ in a manner to maintain its continuity. Figure 4.3 shows the comparison between the exact function and approximate ones (for $n = 4$ and $n = 12$). It can be seen that with a polynomial of order 12 the exact function could be very well approximated.

Next, in order to investigate the periodic solutions and perform bifurcation analysis, a pseudo arc-length continuation and collocation scheme have been used [32, 33]. In this analysis in particular, a bifurcation analysis is carried out in two essential steps: (i) The continuation starts at a trivial steady state solution, zero AC and DC voltages, and zero pressure. In turn, three out of the four parameters (V_{AC} , V_{DC} , Ω and P) are taken as the continuation parameters. The unstable solution branches are avoided in this step. (ii) Bifurcation analysis is performed by using the remaining parameter, whereas the other three parameters are fixed. In this step, the continuation is performed over the entire physical range. The stability of the solution branches is determined using Floquet theory. The obtained solution is stable only if all Floquet multipliers are inside the unit circle [27].

4.4. RESULTS AND DISCUSSION

The procedure outlined in previous the sections has been applied to a Silicon micro-plate with the following properties: $E = 169 \text{ GPa}$, $\nu = 0.17$, $\mu = 2328 \text{ kgm}^{-3}$, $h = 0.6 \mu\text{m}$, $R = 100 \mu\text{m}$ and $d = 2 \mu\text{m}$. The electric permittivity of $\epsilon = 8.854 \times 10^{-12} \text{ F/m}$ has been considered for the gap between the electrodes. Hence, the coefficients in Equation (4.15) are obtained as: $\alpha_1 = 4.139 \times 10^{21}$, $\alpha_2 = 1.981 \times 10^9$, $\alpha_3 = 5.978 \times 10^8$, $\omega_0 = 1.545 \times 10^6 \text{ rad/sec}$, $D = 3.132 \times 10^{-9} \text{ Nm}$. Moreover, a damping ratio of $\zeta = 0.004$ is used in the simulations. In the graphs provided in this section, the amplitudes of vibrations and the deflections are normalized with the initial gap between the electrodes (d).

A convergence analysis has been performed to find the minimum number of in-plane degrees of freedom able to capture the nonlinear motion of the plate accurately. Figure 4.4 shows the frequency response curves of the micro-plate while subjected to a relatively large load equivalent to $V_{AC} = 8 \text{ V}$, while $V_{DC} = 0$ and $P = 0$, and by using different numbers of degrees of freedom for the in-plane displacement. It should be noticed that in Equation (4.15), if $V_{DC} = 0$, the actuation load is proportional to $(V_{AC} \sin(\omega t))^2$, which means the actual excitation frequency is equal to (2Ω) . Therefore, resonance is observed at $\Omega/\omega_0 = 0.5$. Figure 4.4 shows that convergence of the solution can be obtained by only three degrees of freedom (one transverse and two in-plane), and therefore, considering two in-plane degrees of freedom is sufficiently accurate to be used in the reduced-order model. Moreover, the parameter α_1 (the coefficient of geometric nonlinearity in Equation (4.15)) converges to $\alpha_1 = 52.04 \frac{d^2}{\mu h^3 R^4}$ for two in-plane degrees of freedom.

It is worth to note that a convergence study is only reliable if the shape of the displacement field is representative of the motion. Therefore, in order to verify the accuracy of the proposed 4th order mode shape, we compare the hardening effects—as a result of the differential pressure and the high AC voltage—to two other methods. First, the frequency associated with the maximum amplitude in the nonlinear resonance peak is calculated using the proposed model and compared to those ob-

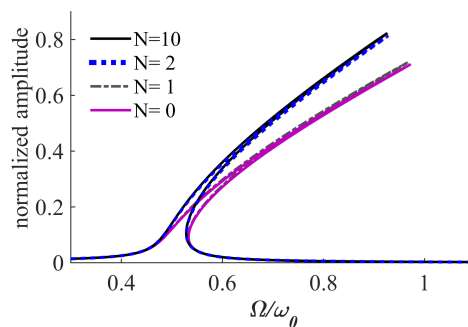


Figure 4.4: Normalized amplitude of vibrations of the system ($\frac{w_{max}-w_{min}}{2d}$) with an electrostatic load equivalent to $V_{AC} = 8 \text{ V}$, as a function of excitation frequency, while $V_{DC} = 0$ and $P = 0$. The graphs are obtained with one transverse degree of freedom and different numbers of in-plane degrees of freedom.

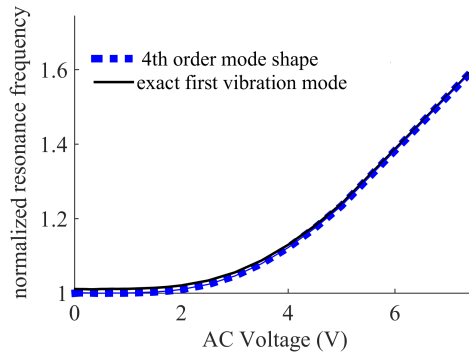


Figure 4.5: Normalized nonlinear resonance frequency as a function of the AC voltage using the propose mode shape and the first linear mode shape of a clamped circular plate calculated with classical plate theory ($J_0(\kappa\rho) - \frac{J_0(\kappa)}{I_0(\kappa)}I_0(\kappa\rho)$, $\kappa = 3.19625$).

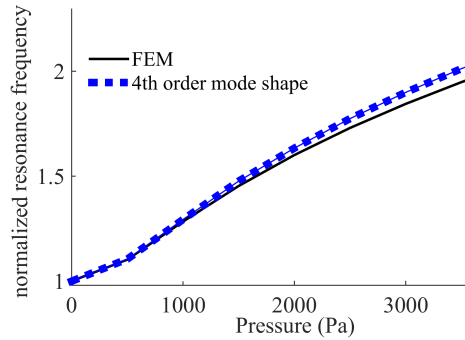


Figure 4.6: Normalized resonance frequency as a function of the differential pressure, while $V_{DC} = 0V$.

tained using the exact linear mode shape of a circular plate (both previously shown in Figure 4.2) as Φ_0 . Figure 4.5 shows the obtained frequency of the peak amplitude normalized with respect to the natural frequency (ω_0), as a function of the applied AC voltage. The graphs in this figure are both derived using two in-plane degrees of freedom ($N = 2$). The proposed 4th order mode shape is capable of predicting the change in resonance frequency with less than 1.5% difference from the model with the exact linear mode shape of a circular plate.

Then, to verify the efficiency of the proposed model for capturing the geometrical stiffness, an eigen-frequency analysis has been performed in a 3D finite element model built in COMSOL Multiphysics and discretized with fine tetrahedral solid elements. To perform this analysis, the plate is subjected to a differential pressure, and the eigen-frequency of the deflected system is obtained while incorporating the geometrical stiffness in the stiffness matrix.

Figure 4.6 shows the linear resonance frequency (normalized with the natural frequency ω_0), as a function of the applied differential pressure, obtained by the proposed 4th order mode shape, and the finite element model. As shown in Figure 4.6,

the proposed model is capable of predicting the change in resonance frequency and is in good agreement with the finite element solution (with less than 3.6% difference). This verifies the suitability of the global modes, for expressing the displacements of the plate, and for capturing the eigenfrequency of the deflected system linearized around its static equilibrium point.

Next, in order to perform a thorough bifurcation analysis, four different sequences of loading have been applied. In each case, three out of four load parameters (V_{DC} , V_{AC} , ω and P) are preserved and one is varied. The associated dynamic pull-in mechanisms of different sequences of loading are investigated.

4.4.1. SWEEP OVER DC VOLTAGE

In this section, the solution branches over the full possible range of DC voltage are investigated while the differential pressure, AC voltage, and its frequency are kept constant. In order to investigate the nonlinear dynamic behavior of the micro-plate in the bi-stable regime discussed in Chapter 2, we set the differential pressure to $P = 3300$ Pa. Moreover, the excitation frequency is set at the natural frequency of the non-pressurized plate ($\Omega/\omega_0 = 1$).

Figure 4.7 shows the variation of the average deflection of the center of the plate (i.e. static deflection) as a function of the applied DC voltage. The graphs are obtained for different AC voltages. When no AC voltage is applied (see $V_{AC} = 0$ V in Figure 4.7), three saddle-node bifurcations (P_1 , P_2 , and P_3) appear which we refer to as the primary, secondary and ultimate limit points. These limit points are equivalent to static instabilities discussed in Chapter 2. Sweeping the DC voltage over these limit points leads to a snap-through behavior or failure of the system.

The primary and secondary limit points only appear if the differential pressure is in opposite direction of the electrostatic pressure. The snap-through which occurs while loading the plate over Point P_1 (or the snap-back which will be observed while unloading the system over Point P_2) is only observed in a limited pressure range. This pressure range is a function of the thickness, radius, and material properties of the plate.

When the plate is dynamically actuated, it goes through a nonlinear resonance for a certain combinations of load parameters (see $V_{AC} = 0.1$ V in Figure 4.7). Therefore, unstable branches emerge in the solution and at the points where the stable and unstable solution branches coincide, a saddle node bifurcation is noticed (see points P_4 and P_5). Increasing the DC voltage around P_4 (or similarly decreasing the DC voltage around P_5) would result in jump from a stable solution to a second stable branch.

When a relatively large AC voltage is applied (see $V_{AC} = 0.3$ V in Figure 4.7), the resonance occurs with a highly nonlinear behavior. In that case, in addition to critical saddle-node bifurcations, a period-doubling (PD) bifurcation appears in the solution. This type of bifurcation is a consequence of one of the Floquet multipliers leaving the unit circle through -1. As a result, a new limit cycle with a period twice the period of the excitation frequency will be generated. This phenomenon usually leads to a transition to chaos and at ultimately, failure of the system [33, 34].

It is worth to note that although the period doubling bifurcation is in the solution of the system, the prominent form of instability is still the saddle node (i.e. the static

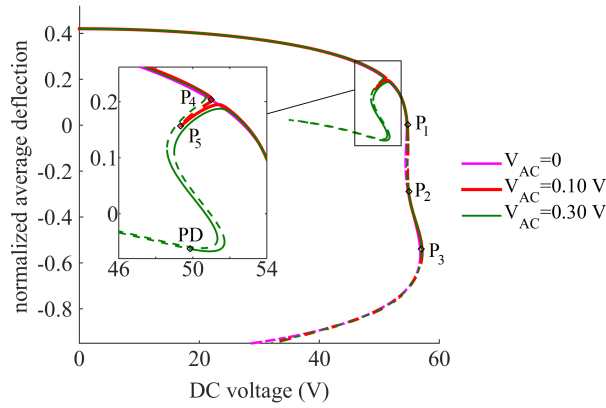


Figure 4.7: The normalized average (static) deflection of the micro-plate as a function of applied DC voltage, while $P = 3300 \text{ Pa}$, $\Omega/\omega_0 = 1$. — stable solution, - - - unstable solution. P_1, P_2 and P_3 indicate primary, secondary and ultimate limit points, while PD demonstrates period-doubling bifurcation.

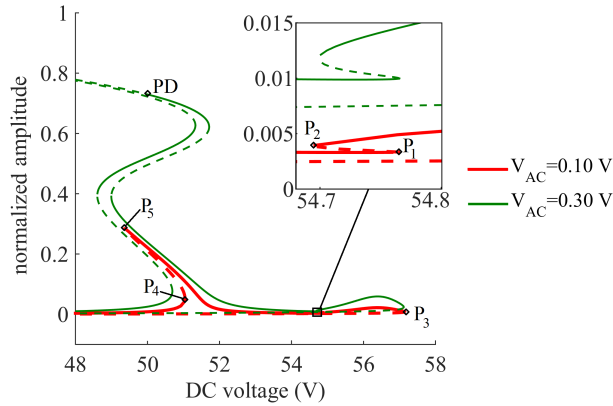


Figure 4.8: The normalized amplitude of vibrations of the micro-plate ($\frac{w_{max} - w_{min}}{2d}$) as a function of applied DC voltage, while $P = 3300 \text{ Pa}$, $\Omega/\omega_0 = 1$. — stable solution, - - - unstable solution. P_1, P_2 and P_3 indicate primary, secondary and ultimate limit points, while PD demonstrates period-doubling bifurcation.

pull-in). In fact, the period doubling bifurcation can be only reached through several loadings and unloadings.

Figure 4.8 shows the amplitude of vibration (i.e. around the static deflection) as a function of the applied DC voltage. The critical points marked in Figure 4.7 are illustrated in this figure, as well. As it can be observed, the vibration has the highest amplitude just before the period doubling bifurcation.

4.4.2. SWEEP OVER EXCITATION FREQUENCY

Next, we study the frequency response curves of the micro-plate, while maintaining other parameters. In this way, we can detect the nonlinear resonance frequencies, and hardening/softening responses for different cases.

Figure 4.9 shows the frequency response curves of the micro-plate subjected to a small AC voltage of 0.01 V and a differential pressure $P = 3300$ Pa. The graphs in this figure are determined for different values of DC voltage. The excitation frequency in this graph is normalized with respect to the natural frequency (undeformed configuration). The applied differential pressure (when V_{DC} is small) leads to a static deflection and therefore, a stretch in the micro-plate. This induces a geometrical stiffness and as a result, a shift (static hardening) in resonance frequency of the system to $1.97\omega_0$ (see $V_{DC} = 2$ V in Figure 4.9-A).

As Figure 4.9 shows, when a DC voltage below the static pull-in is applied to the system (e.g. 50 V), the vibration of the system is approximately linear. Therefore, no nonlinear hardening or softening is observed in the resonance and the frequency response of the system. However, the applied DC voltage relaxes the static deflection and as a result, a shift (static softening) is observed. In higher DC voltages though, both global and nonlinear softening appear in the frequency response of the system (see $V_{DC} = 54$ V and 54.6 V in Figure 4.9-A). As a result, an unstable solution branch emerges in the frequency response curve. At points where the stable and unstable solution branches coincide, a saddle point bifurcation is noticed. If the frequency is swept over the saddle points, the system will jump from one stable branch to the other one. However, it might also become unstable, leading to pull-in. Indeed in such cases, the transient dynamics of the system would determine whether the system settles at a stable orbit, or fails [8]. Finally, when the voltage gets close to primary limit point (i.e. P1 in Figure 4.7), the system loses stability and therefore, the resonance

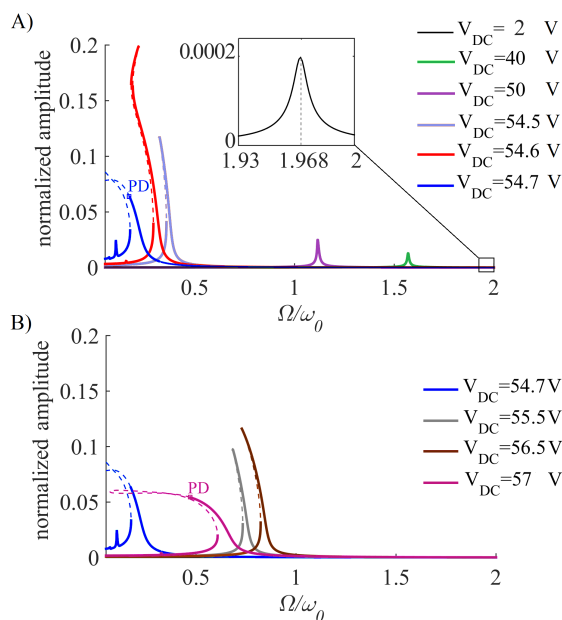


Figure 4.9: The frequency response function of the micro-plate; the normalized amplitude of vibrations ($\frac{w_{max} - w_{min}}{2d}$) as a function of excitation frequency, while $P = 3300$ Pa, and $V_{AC} = 0.01$ V. — stable solution, - - - unstable solution. PD indicates period doubling bifurcation.

frequency of the system tends to zero (see $V_{DC} = 54.7\text{V}$ in Figure 4.9-A), passing a period doubling bifurcation.

Figure 4.9-B shows the frequency response curves of the system for higher DC voltages. These frequency response curves are equivalent to the lower stable branch (i.e. from P2 to P3) of Figure 4.7. As it can be observed, increasing the DC voltage increases the resonance frequency (see $V_{DC} = 55.5\text{V}$ and 56.5V in Figure 4.9-B). When the DC voltage approaches the ultimate limit point (i.e. P3 in Figure 4.7), the frequency response function exhibits a nonlinear softening and finally, loses stability through period doubling (see $V_{DC} = 57\text{V}$ in Figure 4.9-B).

Figure 4.10 illustrates the feasible path taken by the system when sweeping up and down the frequency, when $V_{DC} = 54.7\text{V}$. As it can be observed when the frequency is increased, the system either jumps between the stable solution branches (Figure 4.10-A), or the transient behavior ends up in pull-in. In either case, the period doubling instability would not be noticed. On the other hand, by decreasing the frequency, the system exhibits a first period doubling bifurcation and as a result, the plate oscillates with a period twice the period of the excitation frequency (Figure 4.10-B). By slightly decreasing the frequency, a second period doubling bifurcation is detected (Figure 4.10-C). In fact, this shows that the system could be susceptible to losing stability upon continuous period doubling bifurcations. For the present load combination, sweeping down the frequency is a sufficient condition for observation of the dynamic pull-in.

The phase portrait, Poincaré section, and the time response of the system just before and after the period doubling (for $V_{DC} = 54.7\text{V}$) are illustrated in Figure 4.11. Before the bifurcation (see Figure 4.11-A), a stable periodic solution with frequency Ω , and a closed loop in the phase plane can be observed. After the bifurcation (see Figure 4.11-B), the only stable solution is a bifurcated branch with frequency $\Omega/2$, and a single close curved with two loops in the phase plane.

In Figure 4.9 it was clearly observed that the frequency of the nonlinear resonance peak has a strong dependence on the applied DC voltage. This dependence is explicitly shown in Figure 4.12, when the micro-plate is under the action of combined

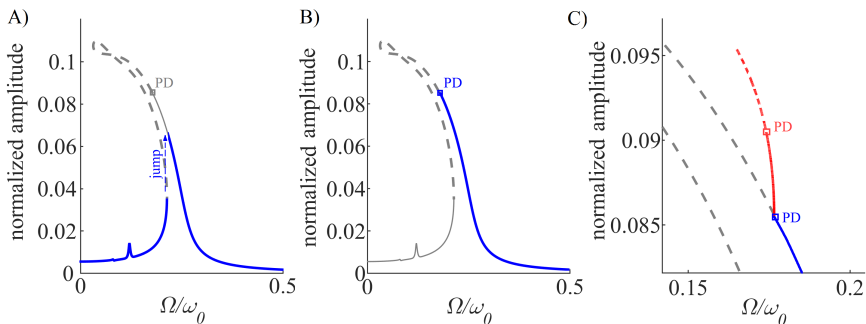


Figure 4.10: The normalized amplitude ($\frac{w_{max}-w_{min}}{2d}$) as a function of excitation frequency observed in A) sweeping up, B) sweeping down the frequency, and C) after the period doubling (zoom-in), while $P = 3300\text{Pa}$, $V_{DC} = 54.7\text{V}$, and $V_{AC} = 0.01\text{V}$. — stable solution, - - - unstable solution. PD indicates period doubling bifurcation.

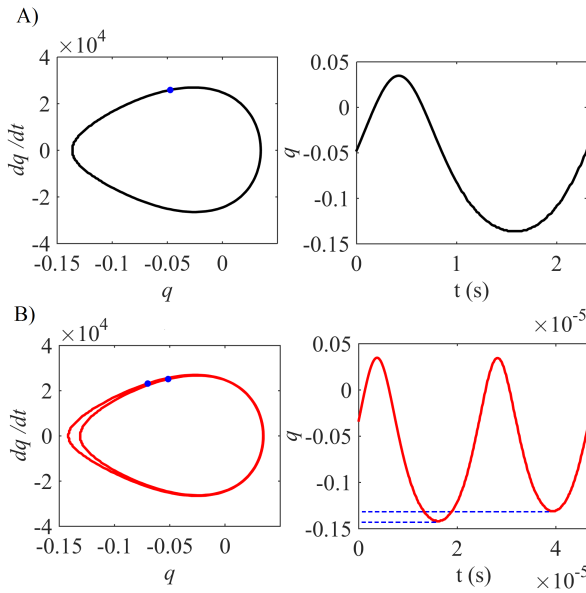


Figure 4.11: The phase portrait, the Poincaré section (the blue dot) and time response of the plate in A) just before period doubling $\Omega/\omega_0 = 0.1765$ and B) after period doubling with the new limit cycle $\Omega/\omega_0 = 0.17585$, while $P = 3300$ Pa, $V_{DC} = 54.7$ V, and $V_{AC} = 0.01$ V.

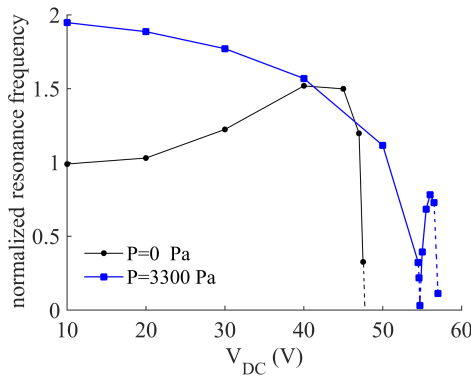


Figure 4.12: The frequency at which the maximum amplitude in the nonlinear resonance peak is obtained as a function of the applied DC voltage. — stable solution, - - - unstable solution

pressure and DC voltage. For comparison, the resonance frequency of a similar system without differential pressure is also shown in this figure. For $P = 3300$ Pa, the results indicate initially a global hardening (due to presence of differential pressure), which changes to softening when increasing the DC voltage, down to zero resonance frequency at the primary critical DC voltage. Increasing the DC voltage above 54.7 V stabilizes the system, and finally at the ultimate limit point the system becomes unstable and fails.

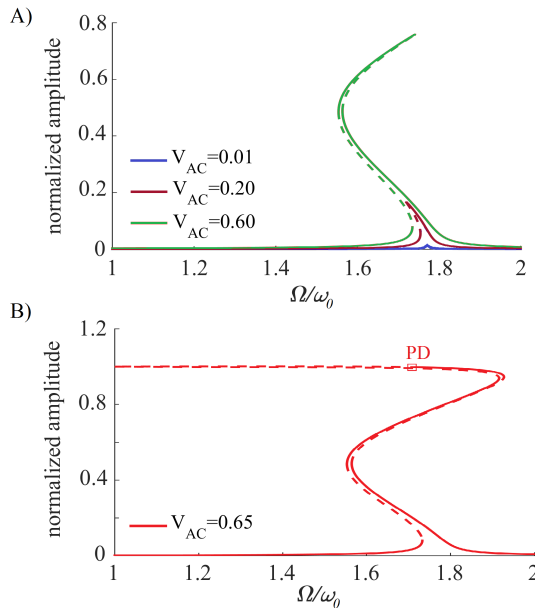


Figure 4.13: The frequency response function of the micro-plate; the normalized amplitude of vibrations ($\frac{w_{max}-w_{min}}{2d}$) as a function of excitation frequency, while $P = 3300$ Pa, and $V_{DC} = 30$ V. — stable solution, - - - unstable solution

Figure 4.13 shows the dynamic response of the micro-plate subjected to different AC voltages and relatively small DC voltage (i.e. $V_{DC} = 30$ V). Exciting the system with a small AC voltage leads to an approximately linear periodic motion around the static configuration ($V_{AC} = 0.01$ V in Figure 4.13-A). When the AC voltage is increased, the vibration of the electrode allows for lower geometrical stiffness and therefore, a dynamic nonlinear softening is observed ($V_{AC} = 0.20$ V). If the voltage is further increased, the softening behavior turns into hardening at $V_{AC} = 0.60$ V, and turns back to softening at $V_{AC} = 0.65$ V (in Figure 4.13-B) which would lead to dynamic pull-in through period doubling bifurcation. A similar behavior was also reported in Ref. [8] for micro-beam resonators. However, this bifurcation will be observed only through several steps of sweeping up or down the frequency. In fact, when a relatively small DC is applied, the system is very robust to frequency sweep and therefore, not prone to dynamic pull-in.

4.4.3. SWEEP OVER AC VOLTAGE

In this section, we study the stability of the micro-plate by varying V_{AC} , and other parameters are preserved. Figure 4.14 shows the variation of amplitude of vibrations as a function of the applied AC voltage. The graphs in this figure are calculated for $P = 3300$ Pa, $V_{DC} = 30$ V, and different driving frequencies. Due to the presence of the differential pressure and DC voltage, the plate has an initial upward static deflection of $\sim 0.37d$. This static deflection induces a geometrical stiffness and therefore, the resonance frequency of the system (when the AC voltage is relatively small) has a

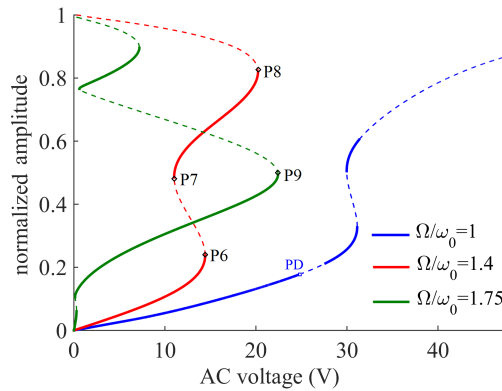


Figure 4.14: A) The normalized amplitude of vibrations ($\frac{w_{max}-w_{min}}{2d}$) as a function of the AC voltage, while $P = 3300\text{Pa}$, and $V_{DC} = 30\text{V}$. — stable solution, - - - unstable solution

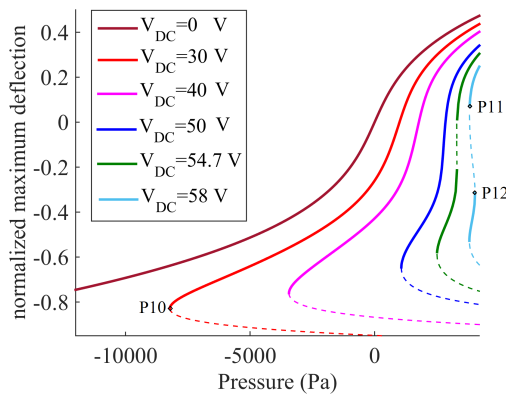


Figure 4.15: The static normalized deflection of the micro-plate ($\frac{w}{d}$) as a function of pressure. — stable equilibrium, - - - unstable equilibrium

shift with respect to its fundamental frequency ($\Omega/\omega_0 = 1.75$).

When the driving frequency is much lower than the resonance frequency of the pressurized system ($\Omega/\omega_0 = 1$ in Figure 4.14), the AC voltage can be increased even to 24.7V and the system would be stable. Finally, in a critical AC voltage the system loses stability upon a period doubling bifurcation and fails. At this critical point, the maximum voltage $V = V_{DC} + V_{AC}$ is very close to the primary limit point for static loading (Figure 4.7).

4.4.4. SWEEP OVER PRESSURE

At a higher driving frequency $\Omega/\omega_0 = 1.4$, three saddle node bifurcations appear in the graph. When increasing (or decreasing) the AC voltage over Point P6 (or P7), the system will snap from one stable solution branch to another. However, increasing the voltage over the other critical point (i.e. P8) will always lead to failure of the system. When the driving frequency is close to the resonance of the pressurized system

$\Omega/\omega_0 = 1.75$, a small AC voltage can cause a relatively high amplitude of vibrations. In this case, also, the pull-in occurs via a saddle-node bifurcation (i.e. Point P9).

Finally, we study the vibration of the micro-plate by varying the differential pressure as the bifurcation parameter, while keeping all other parameters constant. Figure 4.15 shows the static deflection of the micro-plate while loaded by pressure and DC voltage (i.e. $V_{AC} = 0$). As it can be observed, for voltages larger than zero, at least one limit point exists in the equilibrium path of the flexible electrode (e.g. Point P11 in $V_{DC} = 30\text{V}$). At this point, if the amplitude of the pressure increases in the negative direction (similar to electrostatic load), or any other perturbation is introduced to the system, pull-in occurs. For larger voltages, two other limit points appear in the equilibrium path. For example, in the curve corresponding to $V_{DC} = 58\text{V}$, if we sweep down the pressure around Point P11, the system snaps from a positive to a negative deflection.

Next, we preserve the DC voltage at 30V and introduce a small AC voltage to the system. The driving frequency is fixed at $\Omega/\omega_0 = 1$. In Figure 4.16-A, a comparison is made between the maximum deflection in case of static (i.e. $V_{AC} = 0\text{V}$) and dynamic loading (i.e. $V_{AC} = 0.05\text{V}$). As it can be noticed, when a small AC voltage is applied to the system, the overall shape of the equilibrium path does not change. However, in certain combination of load parameters, the system goes through nonlinear resonance. In this case, the resonance occurs in two configurations, at which the system has very similar deformations though in opposite directions.

Figure 4.16-B shows the maximum deflection of the micro-plate while actuated with different AC voltages, in the pressure range which leads to the nonlinear resonance of the system. As it can be observed, by increasing the AC voltage, unstable solution branches might emerge in the response of the system (see $V_{AC} = 0.10\text{V}$). Therefore, sweeping the pressure over these points would result in resonance and finally, a jump to another stable solution branch. Increasing the AC voltage further leads to combination of nonlinear resonances into one stable region (e.g. $V_{AC} = 0.30\text{V}$). As a matter of fact, when sweeping over pressure, the stability of the micro-plate is increased when a higher AC voltage is applied to the system. Overall, when sweeping the pressure, the main mechanism of pull in remains similar to the static pull-in. However, due to the dynamic motion of the micro-plate, the pull-in occurs at a different voltage and deflection.

4.5. CONCLUSIONS

The nonlinear dynamics and stability of an electrically actuated micro-plate subjected to a differential pressure has been addressed. Using an energy approach a reduced-order model was obtained, and then solved numerically. As a consequence of employing proper polynomials as the basis functions, we have been able to calculate the electrostatic load analytically and to obtain a reduced-order model for investigating the nonlinear dynamic behavior of circular micro-plates. The obtained equation incorporates dominant sources of complexities such as geometric and electrostatic nonlinearities and the non-uniform distribution of the electrostatic pressure and is versatile for performing bifurcation analysis. The bifurcation analysis was particularly performed considering pressure, DC and AC voltages and the excitation

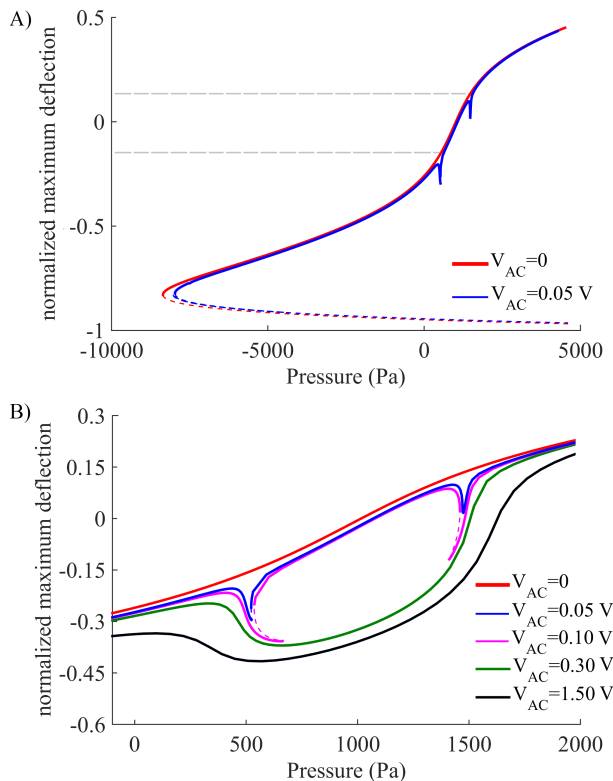


Figure 4.16: The normalized deflection of the micro-plate (its minimum over time $\frac{w_{min}}{d}$) as a function of pressure, while $V_{DC} = 30$ V, for A) whole pressure range and, B) the pressure range with nonlinear resonance — stable solution, - - - unstable solution

frequency.

The results of this study reveal the different possible failure mechanisms depending on the order of the loading applied to the micro-plate. Saddle-node and period doubling bifurcations were repeatedly observed in the analysis and therefore, are recognized as the dominant mechanisms of failure. Moreover, this study shows that in the presence of pressure, increasing the DC or AC voltages could surprisingly help to stabilize the motion of the micro-plate. This is while, in the absence of pressure, increasing the voltage always deteriorated the stability. In addition, in the presence of pressure, the motion of the micro-plate can be bi-stable or multi-stable.

The proposed description is potentially useful for designing sensing mechanisms relying on nonlinear dynamics (e.g. micro-mechanical mass sensors), as well as electrical actuators (such as an inkjet printer head, RF switches, and vacuum resonators). The presented method in this chapter is simple and fast, and it provides a great insight into the nonlinear dynamics of clamped circular micro-plates. Such an insight is necessary for improving the performance of existing MEMS devices, as well as development of new applications.

REFERENCES

- [1] W.-C. Chuang, H.-L. Lee, P.-Z. Chang, and Y.-C. Hu, *Review on the modeling of electrostatic mems*, [Sensors](#) **10**, 6149 (2010).
- [2] J. Sharma and A. Dasgupta, *Effect of stress on the pull-in voltage of membranes for mems application*, [Journal of Micromechanics and Microengineering](#) **19**, 115021 (2009).
- [3] H. Sadeghian, C.-K. Yang, H. Goosen, P. J. F. Van Der Drift, A. Bossche, P. J. F. French, and F. Van Keulen, *Characterizing size-dependent effective elastic modulus of silicon nanocantilevers using electrostatic pull-in instability*, [Applied Physics Letters](#) **94**, 221903 (2009).
- [4] H. Sadeghian, C.-K. Yang, H. Goosen, A. Bossche, P. J. F. French, and F. Van Keulen, *Temperature sensitivity of silicon cantilevers' elasticity with the electrostatic pull-in instability*, [Sensors and Actuators A: Physical](#) **162**, 220 (2010).
- [5] D. Elata and S. Abu-Salih, *Analysis of a novel method for measuring residual stress in micro-systems*, [Journal of Micromechanics and Microengineering](#) **15**, 921 (2005).
- [6] W.-M. Zhang, H. Yan, Z.-K. Peng, and G. Meng, *Electrostatic pull-in instability in mems/nems: A review*, [Sensors and Actuators A: Physical](#) **214**, 187 (2014).
- [7] S. Chowdhury, M. A. Ahmadi, and W. C. Miller, *Pull-in voltage calculations for mems sensors with cantilevered beams*, in [IEEE-NEWCAS Conference, 2005. The 3rd International](#) (IEEE, 2005) pp. 143–146.
- [8] A. H. Nayfeh, M. I. Younis, and E. M. Abdel-Rahman, *Dynamic pull-in phenomenon in mems resonators*, [Nonlinear dynamics](#) **48**, 153 (2007).
- [9] L.-D. Liao, P. C. Chao, C.-W. Huang, and C.-W. Chiu, *Dc dynamic and static pull-in predictions and analysis for electrostatically actuated clamped circular micro-plates based on a continuous model*, [Journal of Micromechanics and Microengineering](#) **20**, 025013 (2010).
- [10] J. Cheng, J. Zhe, X. Wu, K. R. Farmer, V. Modi, and L. Frechette, *Analytical and fem simulation pull-in study on deformable electrostatic micro actuators*, in [Technical Proc. of the International Conf on Modeling and Simulation of Microsystems, MSM](#) (2002) pp. 298–301.
- [11] S. Krylov and S. Seretensky, *Higher order correction of electrostatic pressure and its influence on the pull-in behavior of microstructures*, [Journal of Micromechanics and Microengineering](#) **16**, 1382 (2006).
- [12] J. Lardiès, M. Berthillier, and M. L. Bellaredj, *Analytical investigation of the pull-in voltage in capacitive mechanical sensors*, in [SPIE Microtechnologies](#) (International Society for Optics and Photonics, 2011) pp. 80661N–80661N–10.

- [13] B. Pratiher, *Stability and bifurcation analysis of an electrostatically controlled highly deformable microcantilever-based resonator*, *Nonlinear Dynamics* **78**, 1781 (2014).
- [14] B. Sajadi, F. Alijani, H. Goosen, and F. van Keulen, *Static and dynamic pull-in of electrically actuated circular micro-membranes*, in *ASME 2016 International Mechanical Engineering Congress and Exposition* (American Society of Mechanical Engineers) pp. V04AT05A030–V04AT05A030.
- [15] K. Das and R. C. Batra, *Symmetry breaking, snap-through and pull-in instabilities under dynamic loading of microelectromechanical shallow arches*, *Smart Materials and Structures* **18**, 115008 (2009).
- [16] J. Seeger and B. E. Boser, *Charge control of parallel-plate, electrostatic actuators and the tip-in instability*, *Microelectromechanical Systems, Journal of* **12**, 656 (2003).
- [17] D. I. Caruntu and I. Alvarado, *Influence of van der waals forces on electrostatically actuated mems/nems circular plates*, in *ASME 2011 International Mechanical Engineering Congress and Exposition* (American Society of Mechanical Engineers, 2011) pp. 627–633.
- [18] D. I. Caruntu and I. Alvarado, *On electrostatically actuated nems/mems circular plates*, in *SPIE Smart Structures and Materials+ Nondestructive Evaluation and Health Monitoring* (International Society for Optics and Photonics, 2011) pp. 79810Z–79810Z–10.
- [19] Y.-G. Wang, W.-H. Lin, X.-M. Li, and Z.-J. Feng, *Bending and vibration of an electrostatically actuated circular microplate in presence of casimir force*, *Applied Mathematical Modelling* **35**, 2348 (2011).
- [20] M. Abtahi, G. Vossoughi, and A. Meghdari, *Effects of the van der waals force, squeeze-film damping, and contact bounce on the dynamics of electrostatic microcantilevers before and after pull-in*, *Nonlinear Dynamics* **77**, 87 (2014).
- [21] Z. Li, L. Zhao, Z. Ye, H. Wang, Y. Zhao, and Z. Jiang, *Resonant frequency analysis on an electrostatically actuated microplate under uniform hydrostatic pressure*, *Journal of Physics D: Applied Physics* **46**, 195108 (2013).
- [22] A. H. Nayfeh, M. I. Younis, and E. M. Abdel-Rahman, *Reduced-order models for mems applications*, *Nonlinear dynamics* **41**, 211 (2005).
- [23] G. W. Vogl and A. H. Nayfeh, *A reduced-order model for electrically actuated clamped circular plates*, *Journal of Micromechanics and Microengineering* **15**, 684 (2005).
- [24] G. W. Vogl and A. H. Nayfeh, *A reduced-order model for electrically actuated clamped circular plates*, in *ASME 2003 International Design Engineering Technical Conferences and Computers and Information in Engineering Conference* (American Society of Mechanical Engineers, 2003) pp. 1867–1874.

- [25] D. I. Caruntu and R. Oyervides, *Frequency response reduced order model of primary resonance of electrostatically actuated mems circular plate resonators*, *Communications in Nonlinear Science and Numerical Simulation* **43**, 261 (2017).
- [26] D. Davidovikj, F. Alijani, S. J. Cartamil-Bueno, H. S. van der Zant, M. Amabili, and P. G. Steeneken, *Nonlinear dynamic characterization of two-dimensional materials*, *nature communications* (2017), 10.1038/s41467-017-01351-4.
- [27] M. Amabili, *Nonlinear vibrations and stability of shells and plates* (Cambridge University Press, 2008).
- [28] D. I. Caruntu and R. Oyervides, *Voltage response of primary resonance of electrostatically actuated mems clamped circular plate resonators*, *Journal of Computational and Nonlinear Dynamics* **11**, 041021 (2016).
- [29] A. H. Nayfeh and D. T. Mook, *Nonlinear oscillations* (John Wiley & Sons, 2008).
- [30] S. Timoshenko, S. Woinowsky-Krieger, and S. Woinowsky, *Theory of plates and shells*, Vol. 2 (McGraw-hill New York, 1959).
- [31] M. Amabili and I. D. Breslavsky, *Displacement dependent pressure load for finite deflection of doubly-curved thick shells and plates*, *International Journal of Non-Linear Mechanics* **77**, 265 (2015).
- [32] E. J. Doedel, A. R. Champneys, T. F. Fairgrieve, Y. A. Kuznetsov, B. Sandstede, and X. Wang, *Auto97*, (1998).
- [33] A. H. Nayfeh and B. Balachandran, *Applied nonlinear dynamics: analytical, computational and experimental methods* (John Wiley & Sons, 2008).
- [34] A. Seleim, S. Towfighian, E. Delande, E. Abdel-Rahman, and G. Heppler, *Dynamics of a close-loop controlled mems resonator*, *Nonlinear Dynamics* **69**, 615 (2012).

5

NONLINEAR VIBRATIONS OF ELECTRICALLY ACTUATED 2D NANO-MEMBRANES

In this chapter, the frequency response curves of graphene resonators is introduced as tools for extracting graphene's equivalent Young's modulus. For this purpose, vibrations of an electrically actuated circular graphene membrane are studied both experimentally and numerically. The experiments reveal the dependency of the linear and nonlinear resonance frequency of an electrically actuated graphene nano-resonator on the driving DC and AC voltages. A numerical model, similar to Chapters 4 and 3, is proposed based on nonlinear membrane theory, and by fitting the numerically calculated change in resonance frequency due to DC voltage to those of experimental observations, the Young's modulus of the membrane is determined. It is shown that by using the obtained equivalent Young's modulus, the numerical model can accurately describe the nonlinear dynamics of the graphene membrane in other sets of measurements.

5.1. INTRODUCTION

The exceptional mechanical properties of graphene have made it a promising candidate for the next generation of two dimensional (2D) nano-resonators. Potential applications of these resonators are, among others, pressure, gas and mass sensors [2–6]. In this class, *electrostatically actuated* 2D nano-resonators have a superior advantage for the potential integration and packaging in commercial Nano-Electro-Mechanical Systems (NEMS) [7–11]. In these devices, typically, a parallel-plate capacitor is formed between a fixed bottom electrode and a suspended flexible single or multi-layer graphene membrane. When an alternating (AC) electric potential is applied, a dynamic attractive electrostatic load is induced between the electrodes, leading to deformation and high-frequency excitation of the membrane. In this work a methodology is outlined by which the dependency of the resonance frequency on the DC voltage is used to determine the mechanical properties of graphene membrane.

5

The conventional method for determining mechanical properties of suspended 2D materials is Atomic Force Microscopy (AFM) [12]. Based on AFM measurements, a large range of elastic moduli (0.1–1.1 TPa) has been reported for suspended graphene ribbons and drums [13–15]. AFM requires mechanical contact between a sharp tip and the membrane, which might potentially lead to large stresses and adhesion effects near the tip causing possible membrane fracture [16]. However, a non-contact tool for estimation of the elastic properties of 2D materials, such as presented in this work, can avoid these problems.

In principle, the contact between the sharp tip of AFM cantilever with the membrane could be avoided if a non-contact load (e.g. electrostatic load) is employed to induce the deflection in the suspended graphene membrane. In this regard, the static load-deflection curves of an electrostatically loaded graphene membrane have been utilized to extract its Young's modulus [13, 17]. In this method, the pressure is distributed over the surface, and hence, the membrane is not in contact with a sharp tip applying non-uniform stress.

Another non-contact method for extracting the material properties of graphene membranes is an identification based on nonlinear resonances of the system [18]. Generally, nano-scaled resonators easily reach the nonlinear vibration regime [19–21]. In particular, for graphene, Duffing-type nonlinear responses have been regularly observed [7, 9, 22]. Moreover, in electrostatically actuated nano-resonators, the electrostatic load is also nonlinearly dependent on the deflection [23]. These sources of nonlinearities, which in practice emerge as hardening or softening effects in the frequency response of the system, are potentially beneficial for identification of the stiffness. In this regard, in a recent study, Davidovikj *et al.* [18] have introduced a method for determining the effective Young's modulus of 2D-materials by fitting the forced nonlinear Duffing response of *large amplitude vibrations* to experimental data.

In the present study, an alternative approach for characterization of suspended graphene membranes is proposed which is based on their voltage dependent resonance frequencies. In this approach, *low amplitude vibrations* are employed for material characterization. The natural frequency of an unloaded graphene membrane

is a function of its pretension only [24]. However, when the membrane is subjected to a DC electrostatic load, it will deform, and this deformation, being a function of the Young's modulus, induces geometrical stiffness in the membrane that consequently, leads to a shift in the resonance frequency. Hence, the resonance frequency of the membrane around its deformed configuration will be a function of both Young's modulus and DC voltage. By tracking the change in the resonance frequency as a function of DC voltage one can obtain the Young's modulus.

For this purpose, the vibrations of a circular graphene resonator, electrostatically actuated around its first resonance, are studied both experimentally and theoretically. First, in order to unveil the dynamic characteristics of a graphene resonator, we perform a series of measurements on a graphene membrane subjected to simultaneous DC and AC electrostatic loads. Based on these experiments, the stretching of the graphene resonator due to high DC voltage and the shift in the resonance frequency are investigated.

Next, the vibration of graphene is modeled using an equivalent continuous membrane. The numerical model is based on a Lagrangian approach and total potential energy. In the model, both the nonlinear stretching of the membrane and the non-uniformity of electrostatic load due to deflection of the membrane are incorporated. To the best of the authors' knowledge, despite earlier experimental and theoretical studies on the dynamics of electrostatically actuated graphene resonators [3, 18, 25, 26], there is no model which accounts for in-plane degrees of freedom, geometric and electrostatic nonlinearity in a nano-drum, and yet verified with experiments..

Finally, the equivalent elastic modulus is determined by fitting the theoretically calculated shift in the resonance frequency due to DC voltage, to the experimental results. It should be mentioned that, unlike the method proposed in [18], we utilize the tuning of the linear resonance frequency due to high DC voltages rather than Duffing nonlinearity which appears due to high AC voltages. In this way, (i) the Young modulus is obtained in a non-contact manner, (ii) only the resonance frequency of the system is traced, and (iii) the inaccuracy in the calibration of the amplitude around a deformed configuration will be non-influential. The validity of the proposed method is evaluated by comparing the numerical results to the experiments with high amplitude vibrations as suggested by [18].

5.2. EXPERIMENTS AND DEVICE FABRICATION

To create a platform for the electrostatic 2D nano-resonator, we start with a silicon wafer with a $d = 285$ nm thick layer of thermal silicon dioxide (SiO_2). The schematic of the fabrication process is shown in Figure 5.1. Electrical contacts, circular cavities and bonding pads are patterned on the wafer using e-beam lithography. The electrical contacts consist of a layer of Ti/AuPd, which is physically deposited (via evaporation) providing contact to the graphene membrane, together with a Cr layer which is used as a hard mask for the subsequent etching step (RIE). After etching, the Cr layer is removed using a wet etchant, resulting in cavities with a final depth of $d = 385$ nm and a radius of $R = 2.5$ μm .

Next, flakes of graphene are exfoliated from natural crystals and transferred on top

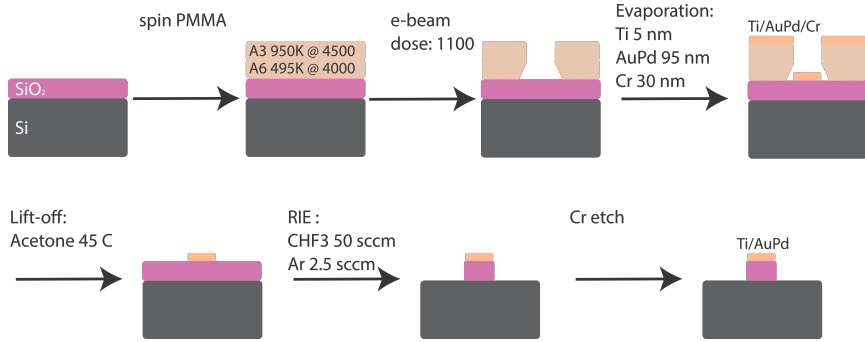


Figure 5.1: The schematic of the fabrication process of the electrical contacts, circular cavities and bonding pads.

5

of the cavities using a dry transfer method [27]. The thickness of the graphene flakes are determined by AFM measurement and are equal to $h = 5$ nm, which is approximately equivalent to 15 layers of graphene. The sample is then mounted in a vacuum chamber. The schematics of the sample and the measurement setup are illustrated in Figure 5.2-A.

In order to actuate the membrane, a combination of AC and DC voltage is applied to the bonding pads using a bias-tee (BT), and the silicon substrate is grounded. The drum's motion is probed by a Helium-Neon laser. The intensity variations caused by the interfering reflections from the moving membrane and the fixed silicon substrate underneath are detected by a photodiode [9]. The detection is done in a homodyne scheme, using a Vector Network Analyser (VNA), that outputs the AC voltage in a combination with a DC voltage source. All measurements were performed using a low laser power (< 1 mW) to reduce heating effects that would influence the mechanical properties of the drum. To relate the measured amplitude to the actual motion of the membrane, a calibration measurement of the drum's Brownian motion is performed [7]. Therefore, the calibration is the most accurate around a non-deformed configuration (i.e. for small DC voltages).

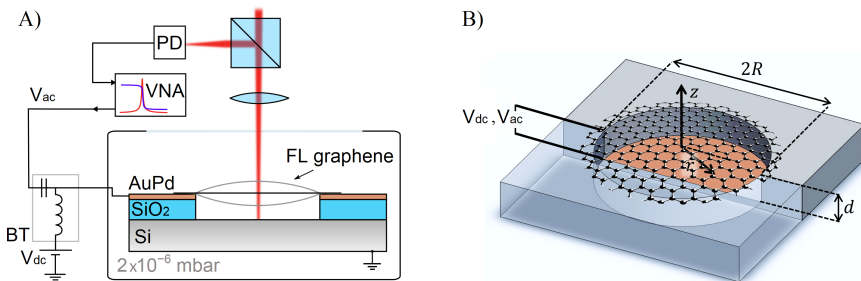


Figure 5.2: Schematics of A) device description and measurement setup with an interferometric laser setup to read out the motion of the membrane, and B) the circular multilayer graphene membrane suspended above a grounded silicon substrate.

5.3. THEORETICAL FORMULATION

In this section, we propose a model for the harmonic response of the electrostatically actuated membrane, around its first resonance frequency. Since the scaling effect on the dynamics of graphene membranes appear at much smaller membrane radii, we use classical continuum to obtain our model [28]. Moreover, the bending energy of the graphene membrane is orders of magnitude smaller than the energy from in-plane strain [12]. Hence, the graphene can be modeled as a membrane, without bending stiffness. This membrane is assumed to be isotropic and homogeneous [22].

The radius of the membrane is R and its thickness is h . The Young's modulus, Poisson ratio and the mass density of the membrane are E , ν and μ , respectively. The membrane is suspended over a grounded electrode, and the initial gap between the two electrodes is d . The schematic model of this system is shown in Figure 5.2-B. An electric potential V consisting of a DC bias voltage (V_{DC}) and an alternating AC voltage (V_{AC}) is applied to the membrane.

The alternating electrostatic field induces an alternating electrostatic load, which causes a dynamic motion in the membrane. Considering that the electrostatic load is symmetric, and the membrane is excited around its fundamental frequency, the non-axisymmetric modes will not be excited. In fact, even if the non-axisymmetric modes are accidentally excited they will decay with time due to the presence of damping [29]. For the axisymmetric modes, the only relevant displacement components are the radial (u) and transverse (w) components. We use a reduced-order model and a Lagrangian approach to obtain the equations of motion for such a system. In this approach, the displacement components are approximated by a superposition of a finite number of suitably chosen basis functions:

$$w(\rho, t) = \sum_{i=1}^N q_i(t) d\Phi_i(\rho), \quad (5.1a)$$

$$u(\rho, t) = \xi_0 R\rho + \sum_{i=1}^n q_{i+N}(t) R\Psi_i(\rho), \quad (5.1b)$$

where $\rho = r/R$ is the normalized radial coordinate, and, $q_i(t)$ are dimensionless generalized coordinates. The parameter ξ_0 models the initial strain due to the pretension N_0 in the membrane:

$$\xi_0 = \frac{N_0(1-\nu)}{Eh}. \quad (5.2)$$

The functions $\Phi_i(\rho)$, and $\Psi_i(\rho)$ are basis-functions satisfying the boundary conditions. Here, axisymmetric linear mode shapes of a clamped membrane are utilized as the transverse basis-functions:

$$\Phi_i(\rho) = J_m(\lambda_{mi}\rho), \quad i = 1 \dots N, \quad (5.3)$$

where, J_m is the m^{th} order Bessel function of the first kind. In fact, m is the number of nodal circles, and λ_{mi} is the i^{th} positive root of J_m . Figure 5.3 shows the first three associated mode-shapes. The in-plane basis-functions (Ψ_i), satisfying continuity and

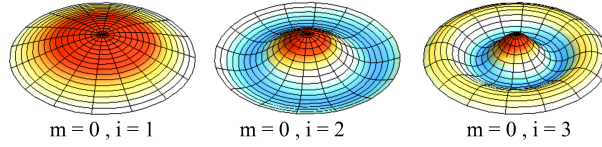


Figure 5.3: The first three axis-symmetric mode-shapes of a membrane with clamped contour, indexed by i and m .

symmetry at $\rho = 0$, are:

$$\Psi_i(\rho) = \rho^i(1 - \rho), \quad i = 1 \dots n. \quad (5.4)$$

Next, the strain components of the membrane are calculated as

$$\varepsilon_r = \frac{1}{R} \frac{\partial u}{\partial \rho} + \frac{1}{2R^2} \left(\frac{\partial w}{\partial \rho} \right)^2, \quad (5.5a)$$

$$\varepsilon_\theta = \frac{1}{R} \frac{u}{\rho}, \quad (5.5b)$$

$$\varepsilon_{r\theta} = 0. \quad (5.5c)$$

The total potential energy of the system consists of two terms: the electrostatic potential (U_e), and the potential associated with elastic deformation due to the stretching (U_s) of the membrane;

$$U = U_s + U_e. \quad (5.6)$$

The elastic potential (U_s) can be approximated by [30]:

$$U_s = \frac{EhR^2}{2(1-\nu^2)} \int_0^{2\pi} \int_0^1 \left(\varepsilon_r^2 + \varepsilon_\theta^2 + 2\nu\varepsilon_r\varepsilon_\theta + \frac{1-\nu}{2} \varepsilon_{r\theta}^2 \right) \rho d\rho d\theta, \quad (5.7)$$

and the electrostatic potential, assuming parallel-plate capacitor theory, can be evaluated as [31]:

$$U_e = -(1-\alpha) \frac{1}{2} \varepsilon V^2 R^2 \int_0^{2\pi} \int_0^1 \frac{\rho}{d+w} d\rho d\theta. \quad (5.8)$$

The constant ε is the electric permittivity of the dielectric between the electrodes and V is the applied voltage. Moreover, α provides a global correction for the electrostatic load, and is the ratio between the actual load applied to the membrane and that of the ideal parallel plate capacitor. This factor is dominated by the fringing field effects which in our setup are mainly due to the electrostatic field between the silicon substrate and the side edge of Ti/AuPd layer in the cavity. However, it can also account for the nano-scale effects that can change the capacitance of the system [32, 33]. This factor can vary for different setups between 0 to 1, depending on the configuration of the capacitor and hence, it should be calibrated for each experimental setup, separately. In this study, we have obtained this parameter using the experimental results

in the low amplitude vibrations. For simplicity, we assume that α does not depend on the deflection of the membrane.

Notice that in formulating the electrostatic potential (U_e), the local distance between the electrodes ($d + w$) is used, where w can be expressed as in (5.1a). When the membrane is excited around the first resonance, the dominant shape of the motion can be mimicked with the first mode shape, and therefore, the effect of higher modes in the electrostatic load can be neglected. Hence, the electrostatic potential is simplified to:

$$U_e = -(1 - \alpha)\pi\epsilon V^2 R^2 \int_0^1 \frac{\rho d\rho}{d + dq_1(t)\Phi_1(\rho)}. \quad (5.9)$$

To calculate the energy associated with the electrostatic potential, the function inside the integral in Equation (5.9) is written as a Taylor series expansion in terms of $q_1(t)$ around the undeformed configuration ($q_1(t) = 0$). The electric potential $V(t)$ in Equations (5.8) and (5.9) consists of a DC bias voltage V_{DC} , and an alternating AC voltage with a root-mean-square (RMS) of V_{AC} and excitation frequency Ω , thus:

$$V = V_{DC} + \sqrt{2}V_{AC} \sin(\Omega t). \quad (5.10)$$

Next, the kinetic energy of the system can be expressed as:

$$T = \pi\mu R^2 h \int_0^1 (\dot{w}^2 + \dot{u}^2) \rho d\rho, \quad (5.11)$$

where overdot indicates differentiation with respect to time. Employing the relations given in Equations (5.1a)–(5.11), the Lagrangian of the system $L = T - U$ can be expressed in terms of generalized coordinates $L(q_i, \dot{q}_i, t)$. Then, the Lagrange equations can be employed to obtain the equations of motion:

$$\frac{\partial L}{\partial q_i} = \frac{d}{dt} \left(\frac{\partial L}{\partial \dot{q}_i} \right). \quad (5.12)$$

As a result, $N + n$ equations governing the motion of the nano-membrane can be obtained. It should be noted here that in practice, the system will possess some kind of energy dissipation or damping. Assuming modal damping, Equation (5.12) gives a system of nonlinear ordinary differential equations:

$$\bar{\mathbf{M}}\ddot{\mathbf{q}} + \bar{\mathbf{C}}\dot{\mathbf{q}} + [\bar{\mathbf{K}}(N_0) + \bar{\mathbf{N}}_2(\mathbf{q}) + \bar{\mathbf{N}}_3(\mathbf{q}, \mathbf{q})]\mathbf{q} = \bar{\mathbf{F}}(\mathbf{q}), \quad (5.13)$$

where $\bar{\mathbf{M}}$ is the mass matrix, and $\bar{\mathbf{C}}$ is the damping matrix which is added to the equations of motion to describe dissipation. $\bar{\mathbf{K}}$ is the stiffness matrix and is a function of the pretension [24], and it determines, together with the mass of the membrane, the natural frequency of the un-loaded configuration. $\bar{\mathbf{N}}_2$ and $\bar{\mathbf{N}}_3$ are matrices which are linear and quadratic functions of the generalized coordinates, respectively, and when multiplied by \mathbf{q} , they cause quadratic and cubic (Duffing) nonlinearities in the equations. These matrices are functions of the Young's modulus of the membrane, as well, and are a consequence of adopting nonlinear (von Kármán) membrane theory.

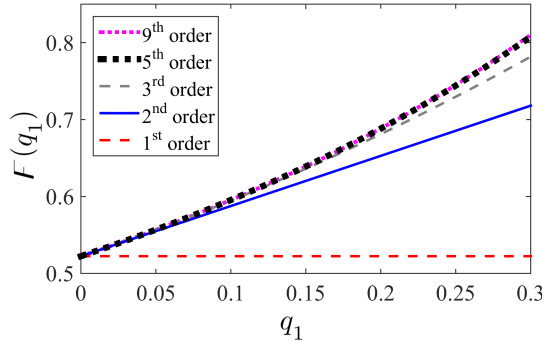


Figure 5.4: The nonlinear electrostatic potential is approximated by a polynomial function with different orders. The resulted approximated electrostatic load converges when a 5th order polynomial is employed.

$\bar{\bar{\mathbf{N}}}_2$ and $\bar{\bar{\mathbf{N}}}_3$ Moreover, $\bar{\bar{\mathbf{F}}}$ is the nonlinear generalized electrostatic force vector whose components are expressed as:

$$\begin{aligned} F_i(t) &= -\frac{1}{2}\epsilon V^2(1-\alpha)\frac{\pi R^2}{d^2}F(q_1) \quad i = 1, \\ F_i(t) &= 0 \quad i > 1. \end{aligned} \quad (5.14)$$

The function $F(q_1)$ is a polynomial which captures the nonlinearity of the electrostatic load and its nonuniform distribution on the deflected membrane. The accuracy of the function $F(q_1)$ depends on the truncation of the Taylor series employed for approximating the integral in Equation (5.9). Figure 5.4 shows different approximations of function F and it indicates that by using a Taylor series of fifth order, good convergence will be achieved.

In order to perform numerical integration, Equation (5.13) is multiplied by the inverse of the mass matrix and then, recast into first-order ordinary differential equations by introducing the dummy vector \mathbf{y} , as follows

$$\begin{aligned} \dot{\mathbf{q}} &= \mathbf{y}, \\ \dot{\mathbf{y}} &= -\bar{\bar{\mathbf{M}}}^{-1}\bar{\bar{\mathbf{C}}}\mathbf{y} - \bar{\bar{\mathbf{M}}}^{-1}[\bar{\bar{\mathbf{K}}}(N_0) + \bar{\bar{\mathbf{N}}}_2(\mathbf{q}) + \bar{\bar{\mathbf{N}}}_3(\mathbf{q}, \mathbf{q})]\mathbf{q} + \bar{\bar{\mathbf{M}}}^{-1}\bar{\bar{\mathbf{F}}}(\mathbf{t}), \end{aligned} \quad (5.15)$$

where $\bar{\bar{\mathbf{M}}}^{-1}\bar{\bar{\mathbf{C}}}$ is the dissipation term, which is assumed to be diagonal based on the assumption of modal damping, and is expressed as:

$$\begin{aligned} [\bar{\bar{\mathbf{M}}}^{-1}\bar{\bar{\mathbf{C}}}]_{ij} &= 2\omega_i\xi_i \quad i = j \\ [\bar{\bar{\mathbf{M}}}^{-1}\bar{\bar{\mathbf{C}}}]_{ij} &= 0 \quad i \neq j \end{aligned} \quad (5.16)$$

In Equation (5.16), ω_i are the natural frequencies obtained from the characteristic equation of the system (i.e. $\det[\omega_i^2\bar{\bar{\mathbf{M}}} - \bar{\bar{\mathbf{K}}}] = 0$), and ξ_i are the corresponding modal damping ratios of each generalized coordinate.

To study the periodic solutions and the frequency response of the system, a pseudo arc-length continuation and collocation scheme have been used [34]. In particular, a

continuation is carried out in three steps: (i) The continuation starts at a trivial steady state solution, zero AC and DC voltages, with a small excitation frequency much below the resonance. (ii) In the second step, the load parameter V_{DC} is chosen as the continuation parameter. Once the desired parameter value is reached, V_{AC} is introduced as the continuation parameter, until the desired value is reached. Unstable solution branches are avoided in this step. (iii) The rest of the analysis is performed by considering the excitation frequency Ω as the continuation parameter. In this step, the continuation is performed around the first resonance of the system and the stability of the solution branches is determined using the Floquet theory [35].

5.4. EXTRACTING THE EQUIVALENT YOUNG'S MODULUS

In this section, we demonstrate the concept of extracting Young's modulus from the fundamental frequency of a pre-tensioned membrane subjected to a high DC voltage and low AC. For this reason, we obtain the static deflection of the membrane due to the applied DC voltage and linearize the equation of motion (i.e. Eq. 5.13) around this configuration. While solving Equation (5.13), the force vector can be split into a static and dynamic components:

$$\bar{\mathbf{F}} = \bar{\mathbf{F}}_s + \bar{\mathbf{F}}_d, \quad (5.17)$$

where, if $V_{AC} \ll V_{DC}$, the dynamic force is much smaller than the static force. Similarly, the solution can be split into two parts:

$$\mathbf{q} = \mathbf{q}_s + \mathbf{q}_d, \quad (5.18)$$

where \mathbf{q}_s and \mathbf{q}_d are the static and dynamic solutions, respectively. The static deflection, \mathbf{q}_s , can be estimated by letting $\bar{\mathbf{F}}_d = 0$ and $\bar{\mathbf{q}} = \dot{\mathbf{q}} = 0$, leading to:

$$[\bar{\mathbf{K}}(N_0) + \bar{\mathbf{N}}_2(\mathbf{q}_s) + \bar{\mathbf{N}}_3(\mathbf{q}_s, \mathbf{q}_s)] \mathbf{q}_s = \bar{\mathbf{F}}_s. \quad (5.19)$$

The solution of this algebraic set of equations provides \mathbf{q}_s as a function of DC voltage and elastic modulus. A relatively small AC voltage will lead to a *linear* vibration around this static configuration. The dynamic analysis in such a configuration shall be performed for determining the final state of vibration by adding an incremental dynamic solution \mathbf{q}_d to the static solution \mathbf{q}_s . By subtracting Equation (5.19) from (5.13), and neglecting the higher order terms in \mathbf{q}_d , the following system of *linear* ordinary differential equations is obtained:

$$\bar{\mathbf{M}}\ddot{\mathbf{q}}_d + \bar{\mathbf{C}}\dot{\mathbf{q}}_d + \underbrace{[\bar{\mathbf{K}}(N_0) + \bar{\mathbf{N}}_2'(\mathbf{q}_s) + \bar{\mathbf{N}}_3'(\mathbf{q}_s, \mathbf{q}_s)]}_{\bar{\mathbf{K}}'(\mathbf{q}_s, E, N_0)} \mathbf{q}_d = \bar{\mathbf{F}}_d. \quad (5.20)$$

In this equation, $\bar{\mathbf{N}}_2'$ and $\bar{\mathbf{N}}_3'$ are associated with nonlinearities in \mathbf{q}_s . Equation (5.20) describes the linear vibrations of the membrane subjected to a relatively small AC voltage around a static configuration (\mathbf{q}_s). The resonance frequencies (ω') can be obtained from the characteristic equation of this new dynamic system, as a function of the static deflection q_s , pretension N_0 and the Young's modulus:

$$|\omega'^2 \bar{\mathbf{M}} - \bar{\mathbf{K}}'(\mathbf{q}_s, E, N_0)| = 0. \quad (5.21)$$

Recall that the static deflection q_s has been obtained as a function of DC voltage from (5.19). With Equation (5.21), the experimental value of ω' can be used to determine the equivalent Young's modulus E , if N_0 and q_s are known.

In order to extract the equivalent Young's modulus from the experimental data, four fundamental steps are taken:

(I) The pretension (N_0) is determined by matching the fundamental frequency of the system in the unloaded configuration ($V_{DC} = 0$) to that of experimental results (ω_0):

$$|\omega_0^2 \bar{\mathbf{M}} - \bar{\mathbf{K}}(N_0)| = 0. \quad (5.22)$$

(II) The damping ratio of the first resonance frequency (ξ_1) is obtained by fitting the low amplitude response curves (down point method) [36].

(III) The force correction factor (α) is determined by matching the numerical amplitude of the system (A_0) in low-amplitude vibrations, to the calibrated experimental data [7]. For small DC and AC voltages, one can simply ignore the geometric and electrostatic nonlinearity, and assume harmonic oscillations. Therefore [37],

$$A_0 = (1 - \alpha) F(0) \frac{\epsilon \pi R^2 V_{AC} V_{DC}}{d^2 2 \xi_1 \bar{\mathbf{K}}_{11}}. \quad (5.23)$$

(IV) Using the obtained quality factor, pretension and force correction factor, the fundamental frequency (ω') of the system is obtained numerically for a range of nonzero DC voltages (Equation (5.21)). The equivalent Young's modulus of the membrane is then achieved by fitting *the voltage dependent shift in resonance frequency* (ω') to the experimental results.

5.5. RESULTS AND DISCUSSION

In this section, the results of the experiments and theoretical studies are reported, and the suitability of the proposed numerical model as a tool for characterization of the graphene membrane and analyzing its nonlinear vibrations is investigated.

5.5.1. EXPERIMENTS

Figure 5.5 shows a set of experimental forced vibration responses around the fundamental frequency while varying the driving DC and AC voltage. The deflection was measured at the center of the membrane, where the fundamental mode shape presents the largest amplitude. In the first set, the AC voltage is kept fixed (with low RMS value of 4.5 mV) and the change in the linear resonance of the system is traced by varying the DC voltage. The natural frequency (i.e. when $V_{DC} = 0$ V) was obtained to be 13.4 MHz. This frequency has been used to obtain the pretension in the membrane. The resonance frequency slightly decreases when a small DC voltage is applied to the system, e.g. at $V_{DC} = 0.5$ V, the resonance occurs at 13.36 MHz. The frequency response of the system at this configuration is used to obtain the force correction factor. When a higher DC voltage is applied, the resonance frequency increases (see Figure 5.5-A). This change in resonance frequency is due to electrostatic (softening) and then the geometrical (hardening) nonlinearity. However, the frequency

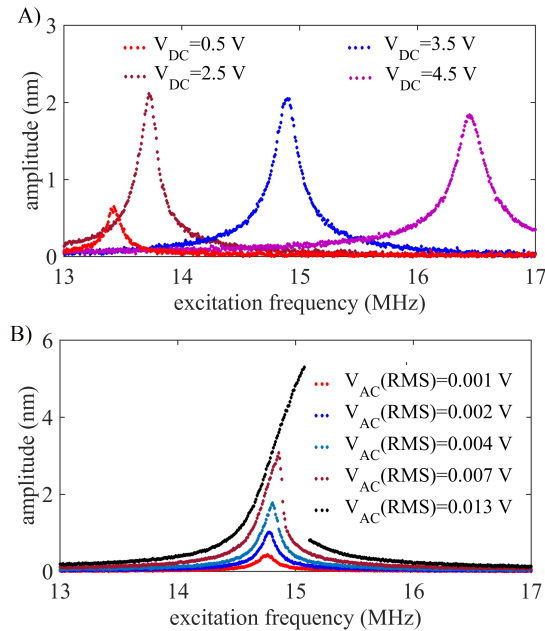


Figure 5.5: The measured amplitude of the motion as a function of excitation frequency, A) with a small AC voltage of $V_{AC} = 4.5$ mV, and different DC voltages, and B) with different AC voltages and a DC voltage of $V_{AC} = 3$ V. The measurements are taken at the center of the drum.

response function of the membrane remains linear.

It should be noticed that the maximum amplitude of the vibrations at the resonance varies with the applied DC voltage, as well. As a matter of fact, the maximum amplitude is defined by the stiffness of the system and the dynamic load, both of which depend on the DC voltage. This dependence causes the maximum amplitude to increase with the DC voltage due to a larger dynamic load, and later decrease due to higher geometrical stiffness induced in the membrane and higher damping.

Figure 5.5-B shows the experimentally obtained frequency response curves obtained by keeping the DC voltage constant at 3V and varying the AC voltage from 0.001 V to 0.013 V. As can be observed, at AC voltages above 0.004 V, the system exhibits nonlinear hardening behavior. At $V_{AC} = 0.013$ V, the system shows a clear instability and therefore a jump right after the resonance.

5.5.2. VALIDATION OF THE NUMERICAL MODEL

To validate the model (Equation (5.13)) numerically, its convergence is tested and it is compared to finite element methods in this section. The procedure outlined in Section 5.3 has been applied to a membrane with the following properties: $\nu = 0.165$, $\mu = 2.2388$ g/cm³, $h = 5$ nm, $R = 2.5$ μ m and $d = 385$ nm. Moreover, a relatively low damping ratio ($\xi_i = 0.002$) is considered in the following numerical results. In the validation of the numerical model, the effects of force correction factor are ignored

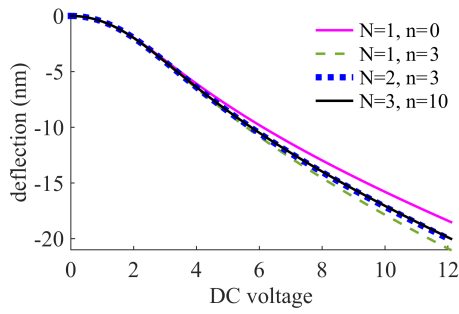


Figure 5.6: Deflection of the membrane when $E = 1150$ GPa, $N_0 = 0.085$ N/m, $V_{AC}(RMS) = 0$ V, calculated with different numbers of degrees of freedom. The solution converges at 5 degrees of freedom ($N=2$ and $n=3$).

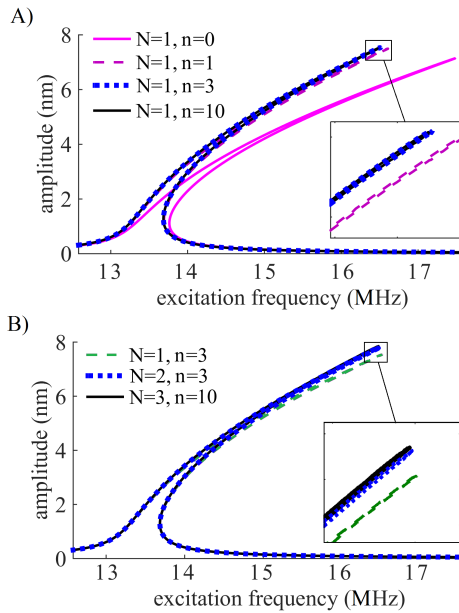


Figure 5.7: Root-mean-square amplitude of the membrane when $E = 1150$ GPa, $N_0 = 0.085$ N/m, $\xi = 0.002$, $V_{AC}(RMS) = 0.02$ V and $V_{DC} = 1$ V, numerically calculated with A) different numbers of in-plane degrees of freedom and B) transverse degrees of freedom. The solution around the first resonance converges at 5 degrees of freedom ($N=2$ and $n=3$).

($\alpha = 0$). In the Lagrangian approach, basis functions are employed to approximate the exact solution of the problem, and therefore, a convergence analysis is required to confirm the accuracy of the described deflection. In order to find the minimum number of degrees of freedoms required to accurately model the motion of the membrane (N and n), two convergence analyses (static and dynamic) have been performed. In both analyses the Young's modulus of pristine graphene (i.e. $E = 1150$ GPa

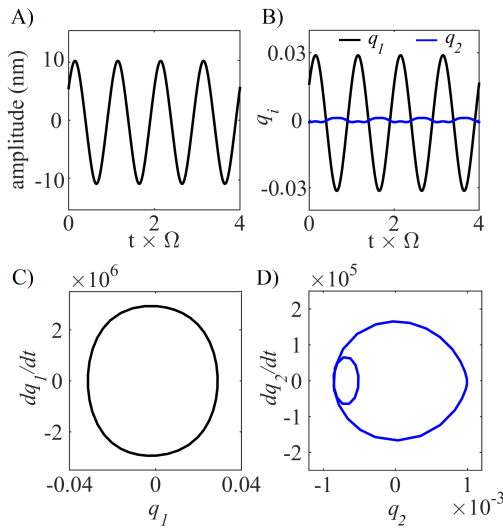


Figure 5.8: Time response of A) the deflection at the center of the membrane and B) the first two mode shapes, and two-dimensional projection of the phase portrait of C) first, and D) second modes, slightly before the resonance ($\Omega = 16.5$ GHz), using $E = 1150$ GPa, $N_0 = 0.085$ N/m, $\xi = 0.002$, $V_{AC}(RMS) = 0.02$ V and $V_{DC} = 1$ V.

[38]) is considered, to impose the highest possible *geometrical* nonlinearity in Equation (5.13). The static deflection of the membrane as a function of the applied DC voltage, when considering different numbers of degrees of freedom, is shown in Figure 5.6. The DC voltage is varied from 0–10V in the absence of V_{AC} . As can be observed, the static solution converges when 5 degrees of freedom are used in the numerical model (with two transverse and three in-plane basis functions).

In the dynamic convergence analysis, the membrane is assumed to be subjected to a DC voltage of $V_{DC} = 1$ V and a high AC voltage with the root-mean-square (RMS) of 0.025V. The steady state solution of the membrane is calculated in a frequency range around the first resonance. Figure 5.7 shows the nonlinear frequency responses of the membrane when considering different numbers of degrees of freedom. In particular, Figure 5.7-A shows the effect of additional in-plane basis functions on the nonlinear dynamic response and Figure 5.7-B shows the effect of additional transverse basis functions. It can be observed that the dynamic solution also converges with five degrees of freedom (with two transverse and three in-plane mode-shapes). Therefore, all the following numerical results are obtained by using a model including these five degrees of freedom.

Recall that in calculating the electrostatic potential in Equation 5.9, the contribution of higher modes was neglected assuming $q_1 \gg q_i$ for $i > 1$. In order to check the validity of this assumption, the time response and phase portrait of the first two transverse modes of the system, right before the nonlinear resonance (15.6MHz) are shown in Figure 5.8. The graphs in this figure are obtained using the same parameter values as in Figures 5.6 and 5.7. As can be noticed, the maximum amplitude and time derivative of the second mode are an order of magnitude smaller than the amplitude

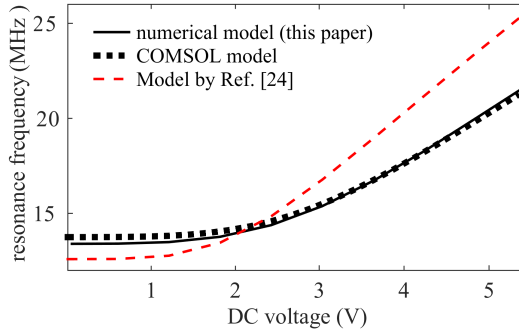


Figure 5.9: The numerical resonance frequency of the excited membrane as a function of the applied DC voltage obtained by different models, using $E = 1150 \text{ GPa}$, $N_0 = 0.085 \text{ N/m}$, $\xi = 0.002$, $V_{AC}(RMS) = 4.5 \text{ mV}$.

5

and time derivative of the first mode.

Finally, to verify the efficiency of the proposed model, an eigen-frequency analysis has been performed for a 3D finite element model built in COMSOL Multiphysics and compared to the present model. In the COMSOL model, the membrane is modeled with the same characteristics as in the convergence analysis and is discretized with fine mesh consisting of shell elements. The surface of the membrane is loaded with a nonlinear electrostatic load $\epsilon \frac{-V_{dc}^2}{2(d+w)^2}$, where w is the transverse displacement field of the outer surface of the membrane, and V_{dc} is a parameter representing the DC voltage. The eigen-frequency of the deflected system for a range of V_{dc} is obtained while incorporating the geometrical stiffness.

Figure 5.9 shows the obtained linear resonance frequency, as a function of the applied voltage. For comparison the graphs obtained by the proposed model, finite element model, and also the approximate model proposed by Ref. [26] are shown. As can be observed, the proposed model is perfectly matching the results of the FEM solution, while the single degree of freedom model of Ref. [26] diverges from these two solutions. This figure demonstrates the accuracy of the proposed method in capturing the effect of DC voltage on the resonance frequency of the membrane.

5.5.3. EXTRACTING THE EQUIVALENT YOUNG'S MODULUS

As mentioned in Section 5.4, the change in resonance frequency of the deflected membrane due to the applied DC voltage is an indication of the Young's modulus. In order to find the accurate equivalent Young's modulus, we compare the experimentally observed change in the resonance frequency to the numerical results. Based on the experimental results, a range of damping ratios (0.0038 – 0.0040) and a force correction factor of $\alpha = 0.25$ are obtained and employed for extracting the equivalent Young's modulus.

Figure 5.10 shows the obtained resonance frequency as a function of the applied DC voltage. A pretension of $N_0 = 0.0857 \text{ N/m}$ matches the natural frequency at zero DC voltage to the experiments. For illustrating the effect of employing different elas-

tic moduli, the numerical results for $E = 210$ GPa, $E = 560$ GPa, and that of pristine graphene ($E = 1150$ GPa [38]) are shown. It can be observed that the numerical results for $E = 560$ GPa are in good agreement with the experimental observations. In other words, the proposed model with this Young's modulus is able to capture the nonlinear hardening of the electrostatically actuated graphene membrane.

In order to verify the accuracy of the obtained Young's modulus, the trend of nonlinearity by varying the AC voltage is compared with the associated experimental data [18]. Figure 5.11 presents the amplitude of vibration at the center of the graphene membrane for a constant DC voltage (3 V) and different AC voltages, as expressed in Equation (5.13). As can be observed, a very good agreement is found between the experimental and numerical results for different applied dynamic loads. The numerical results in Figure 5.11 show that there are two bifurcation points associated with jump up and down in the vibration amplitude. However, such hysteresis cycle is not evident from the experimental data, because the experiments were performed by forward frequency sweeps only.

It is worth to mention that the nonlinear hardening observed in the frequency response of the excited membrane, is induced by the quadratic and cubic terms in Equation (5.13) which appear in \mathbf{N}_2 , \mathbf{N}_3 and $\mathbf{F}(\mathbf{q})$. Therefore, not only the Young's modulus, but also the applied DC voltage have an influence on the nonlinearity, which if neglected, might be mistaken with Duffing type nonlinearity.

The nonlinear resonance frequency of the system (the peaks in Figure 5.11) varies with the applied AC voltage. This change is illustrated more specifically in Figure 5.12. Due to presence of the static DC voltage, the resonance frequency of the system has a shift with respect to the free-vibration fundamental frequency (13.6 MHz), and by increasing the dynamic load (AC voltage) the system exhibits a nonlinear hardening and the resonance frequency increases further. The overall trend of the hardening of the system obtained numerically with $E = 560$ GPa is in good agreement with the experiments, which confirms the accuracy of the obtained Young's modulus.

Finally, we shall stress that the correct evaluation of the force correction factor employed in Equation (5.8) is a crucial aspect in characterization of the Young's mod-

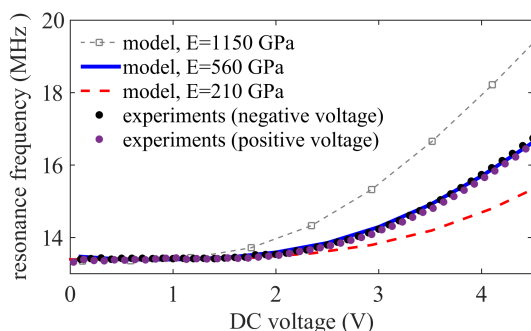


Figure 5.10: The measured resonance frequency of the excited membrane as a function of the applied DC voltage, while $V_{AC}(RMS) = 4.5$ mV, and the corresponding curve obtained numerically using $E = 210$ GPa, $E = 560$ GPa, and $E = 1150$ GPa when $N_0 = 0.0857$ N/m and $\alpha = 0.25$.

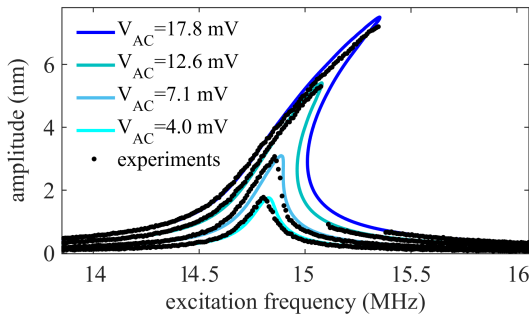


Figure 5.11: Measured traces (black scatter plot) and the corresponding curves obtained numerically (solid curves) using $E = 560$ GPa, and a modal damping ratio of $\xi = 0.004$ while $V_{DC} = 3$ V.

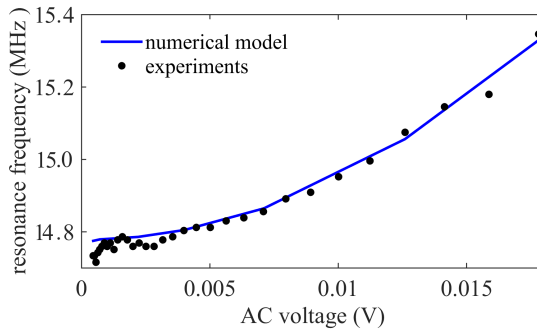


Figure 5.12: The measured resonance frequency of the excited membrane as a function of the applied AC voltage, while $V_{DC} = 3$ V, and the corresponding curve obtained analytically using $E = 560$ GPa.

ulus. Figure 5.13-A shows the obtained Young's modulus which matches the voltage dependent frequency shift as a function of this factor. As can be observed an inaccurate estimation of this factor can result in incorrect characterization of the Young's modulus. If this correction factor is neglected, the corresponding elastic modulus will be obtained as 310 GPa. As shown in Figure 5.13-B, if an inaccurate correction factor is employed to obtain the Young's modulus, the numeric results will not match the high amplitude vibrations.

5.6. CONCLUSIONS

Resonance frequency tuning of an electrostatically actuated multi-layer graphene membrane with a DC voltage has been introduced as a tool for evaluation of its equivalent Young's modulus. For this purpose, using an energy approach based on a Lagrange formulation, the equations of motion were derived, and solved numerically. The proposed model extends the earlier work on electrostatically actuated graphene membranes [26], by including not only transverse, but also radial displacements of the graphene. Moreover, based on a comparison to a detailed finite elements solu-

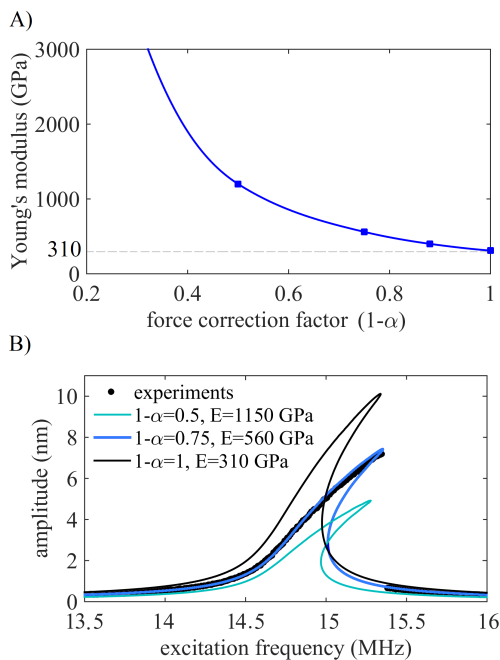


Figure 5.13: A) The matching Young's modulus as a function of the force correction factor $(1 - \alpha)$, and B) measured traces (black scatter plot) and the corresponding curves obtained numerically with different force correction factors, while $V_{DC} = 3$ V and $V_{AC} = 17.8$ mV.

tion, it has been shown that the proposed model can capture the effect of DC voltage on the frequency response, accurately.

In this study, experiments were performed to explore the linear and nonlinear vibrations of an electrostatically actuated graphene membrane. As a result, the shift in resonance frequency and nonlinear hardening and softening behavior, due to geometrical and electrostatic nonlinearities, have been investigated. It was shown that by comparing the model to experimental data, the pretension, the force correction factor, and the Young's modulus of the graphene can be determined. The obtained Young's modulus also closely matched the non-linear dynamics of the membrane, providing evidence for suitability of this method for extracting the Young's modulus of the 2D-nano resonators.

Moreover, it was found that the accurate estimation of the electrostatic load is one of the most crucial factors in this method of characterization of the Young's modulus. For a parallel plate capacitor, the fringing fields effects can be calculated theoretically. However, the fringing field, although probably the most dominant, is one out of many other factors influencing the electrostatic load [32, 33]. Therefore, it is most efficient to extract this factor directly from the experimental results.

It should be mentioned that the obtained value of the Young's modulus ($E = 560$ GPa) is lower than the reported value in literature for pristine graphene. This difference which has been repeatedly reported in other experimental studies [39], is hypothesized to be the result of wrinkles, ripples or defects in the graphene. Defects

such as wrinkles and ripples [13, 15], or grained size of the polycrystalline [39, 40], may affect the elasticity of the graphene to a large extent.

The proposed method for extracting the Young's modulus is non-contact and non-destructive, and it does not require calibration of the amplitude of vibrations in high DC voltages. In addition, this method is simple to implement and is computationally efficient.

REFERENCES

- [1] B. Sajadi, F. Alijani, D. Davidovikj, P. G. Steeneken, H. Goosen, and F. van Keulen, *Experimental characterization of graphene by electrostatic resonance frequency tuning*, *Journal of Applied Physics* **in press** (2017).
- [2] F. Schedin, A. Geim, S. Morozov, E. Hill, P. Blake, M. Katsnelson, and K. Novoselov, *Detection of individual gas molecules adsorbed on graphene*, *Nature materials* **6**, 652 (2007).
- [3] C. Chen, S. Rosenblatt, K. I. Bolotin, W. Kalb, P. Kim, I. Kymissis, H. L. Stormer, T. F. Heinz, and J. Hone, *Performance of monolayer graphene nanomechanical resonators with electrical readout*, *Nature nanotechnology* **4**, 861 (2009).
- [4] R. J. Dolleman, D. Davidovikj, S. J. Cartamil-Bueno, H. S. van der Zant, and P. G. Steeneken, *Graphene squeeze-film pressure sensors*, *Nano letters* **16**, 568 (2015).
- [5] P. Li, B. Zhang, and T. Cui, *Towards intrinsic graphene biosensor: A label-free, suspended single crystalline graphene sensor for multiplex lung cancer tumor markers detection*, *Biosensors and Bioelectronics* **72**, 168 (2015).
- [6] D. Garcia-Sanchez, A. M. van der Zande, A. S. Paulo, B. Lassagne, P. L. McEuen, and A. Bachtold, *Imaging mechanical vibrations in suspended graphene sheets*, *Nano letters* **8**, 1399 (2008).
- [7] D. Davidovikj, J. J. Slim, S. J. Cartamil-Bueno, H. S. van der Zant, P. G. Steeneken, and W. J. Venstra, *Visualizing the motion of graphene nanodrums*, *Nano letters* **16**, 2768 (2016).
- [8] S. Lee, C. Chen, V. V. Deshpande, G.-H. Lee, I. Lee, M. Lekas, A. Gondarenko, Y.-J. Yu, K. Shepard, and P. Kim, *Su-8 clamped cvd graphene drum resonators*, *arXiv preprint arXiv:1612.04279* (2016), [10.1063/1.4793302](https://doi.org/10.1063/1.4793302).
- [9] J. S. Bunch, A. M. Van Der Zande, S. S. Verbridge, I. W. Frank, D. M. Tanenbaum, J. M. Parpia, H. G. Craighead, and P. L. McEuen, *Electromechanical resonators from graphene sheets*, *Science* **315**, 490 (2007).
- [10] H. Tian, Y. Shu, X.-F. Wang, M. A. Mohammad, Z. Bie, Q.-Y. Xie, C. Li, W.-T. Mi, Y. Yang, and T.-L. Ren, *A graphene-based resistive pressure sensor with record-high sensitivity in a wide pressure range*, *Scientific reports* **5** (2015).
- [11] J. Lee, Z. Wang, K. He, J. Shan, and P. X.-L. Feng, *High frequency mos2 nanomechanical resonators*, *ACS nano* **7**, 6086 (2013).
- [12] C. Lee, X. Wei, J. W. Kysar, and J. Hone, *Measurement of the elastic properties and intrinsic strength of monolayer graphene*, *science* **321**, 385 (2008).
- [13] R. J. Nicholl, H. J. Conley, N. V. Lavrik, I. Vlassioux, Y. S. Puzyrev, V. P. Sreenivas, S. T. Pantelides, and K. I. Bolotin, *The effect of intrinsic crumpling on the mechanics of free-standing graphene*, *Nature communications* **6** (2015).

- [14] A. Zandiatashbar, G.-H. Lee, S. J. An, S. Lee, N. Mathew, M. Terrones, T. Hayashi, C. R. Picu, J. Hone, and N. Koratkar, *Effect of defects on the intrinsic strength and stiffness of graphene*, *Nature communications* **5** (2014).
- [15] S. Deng and V. Berry, *Wrinkled, rippled and crumpled graphene: an overview of formation mechanism, electronic properties, and applications*, *Materials Today* **19**, 197 (2016).
- [16] M. Huang and J. R. Greer, *Measuring graphene piezoresistance via in-situ nanoindentation*, *Ecs Transactions* **35**, 211 (2011).
- [17] C. Wong, M. Annamalai, Z. Wang, and M. Palaniapan, *Characterization of nanomechanical graphene drum structures*, *Journal of Micromechanics and Microengineering* **20**, 115029 (2010).
- [18] D. Davidovikj, F. Alijani, S. J. Cartamil-Bueno, H. S. van der Zant, M. Amabili, and P. G. Steeneken, *Nonlinear dynamic characterization of two-dimensional materials*, *nature communications* (2017), [10.1038/s41467-017-01351-4](https://doi.org/10.1038/s41467-017-01351-4).
- [19] R. Lifshitz and M. Cross, *Nonlinear dynamics of nanomechanical and micromechanical resonators*, in *Review of nonlinear dynamics and complexity*, Vol. 1 (2008) pp. 1–52.
- [20] J. Atalaya, A. Isacson, and J. M. Kinaret, *Continuum elastic modeling of graphene resonators*, *Nano letters* **8**, 4196 (2008).
- [21] Z. Wang and P. X.-L. Feng, *Dynamic range of atomically thin vibrating nanomechanical resonators*, *Applied Physics Letters* **104**, 103109 (2014).
- [22] C. Chen, S. Lee, V. V. Deshpande, G.-H. Lee, M. Lekas, K. Shepard, and J. Hone, *Graphene mechanical oscillators with tunable frequency*, *Nature nanotechnology* **8**, 923 (2013).
- [23] D. I. Caruntu and I. Alvarado, *On electrostatically actuated nems/mems circular plates*, in *SPIE Smart Structures and Materials+ Nondestructive Evaluation and Health Monitoring* (International Society for Optics and Photonics, 2011) pp. 79810Z–79810Z–10.
- [24] A. W. Leissa and M. S. Qatu, *Vibrations of Continuous Systems* (McGraw-Hill, 2011).
- [25] A. Eriksson, D. Midtvedt, A. Croy, and A. Isacson, *Frequency tuning, nonlinearities and mode coupling in circular mechanical graphene resonators*, *Nanotechnology* **24**, 395702 (2013).
- [26] C. Chen, *Graphene NanoElectroMechanical Resonators and Oscillators* (Columbia University, 2013).
- [27] A. Castellanos-Gomez, M. Buscema, R. Molenaar, V. Singh, L. Janssen, H. S. van der Zant, and G. A. Steele, *Deterministic transfer of two-dimensional materials by all-dry viscoelastic stamping*, *2D Materials* **1**, 011002 (2014).

- [28] B. Arash and Q. Wang, *Vibration of single-and double-layered graphene sheets*, [Journal of Nanotechnology in Engineering and Medicine](#) **2**, 011012 (2011).
- [29] M. Amabili, F. Alijani, and J. Delannoy, *Damping for large-amplitude vibrations of plates and curved panels, part 2: Identification and comparisons*, *International Journal of Non-Linear Mechanics* **85**, 226 (2016).
- [30] S. Timoshenko, S. Woinowsky-Krieger, and S. Woinowsky, *Theory of plates and shells*, Vol. 2 (McGraw-hill New York, 1959).
- [31] W.-M. Zhang, H. Yan, Z.-K. Peng, and G. Meng, *Electrostatic pull-in instability in mems/nems: A review*, [Sensors and Actuators A: Physical](#) **214**, 187 (2014).
- [32] J. Xia, F. Chen, J. Li, and N. Tao, *Measurement of the quantum capacitance of graphene*, [Nature nanotechnology](#) **4**, 505 (2009).
- [33] C. Zhan, J. Neal, J. Wu, and D.-e. Jiang, *Quantum effects on the capacitance of graphene-based electrodes*, [The Journal of Physical Chemistry C](#) **119**, 22297 (2015).
- [34] E. J. Doedel, A. R. Champneys, T. F. Fairgrieve, Y. A. Kuznetsov, B. Sandstede, and X. Wang, *Auto97*, (1998).
- [35] J. Guckenheimer and P. J. Holmes, *Nonlinear oscillations, dynamical systems, and bifurcations of vector fields*, Vol. 42 (Springer Science and Business Media, 2013).
- [36] D. J. Inman, *Engineering vibration*, (2014).
- [37] D. J. Ewins, *Modal testing: theory and practice*, Vol. 15 (Research studies press Letchworth, 1984).
- [38] J. Xiao and J. Gillespie Jr, *Fracture behaviors of graphene sheets and carbon nanotubes* (INTECH Open Access Publisher, 2011).
- [39] A. Isacsson, A. W. Cummings, L. Colombo, L. Colombo, J. M. Kinaret, and S. Roche, *Scaling properties of polycrystalline graphene: a review*, [2D Materials](#) **4**, 012002 (2016).
- [40] A. Shekhawat and R. O. Ritchie, *Toughness and strength of nanocrystalline graphene*, *Nature communications* **7** (2016).

6

CAPTURING SIZE-DEPENDENT BEHAVIOR OF PLATES WITH NONLOCAL THEORY

In spite of the advances in scaling the MEMS down to nano-scales, many of the fundamental issues related to the mechanics at such a scale remain unresolved. The effective elastic properties of nano-structures are shown to be strongly size-dependent. Thus, classical continuum theory fails to give a good prediction of the mechanical behavior for such length scales. In this chapter, using nonlocal elasticity theory, we aim to capture the size-dependent effects of plate structures as a function of their thickness. This, however, is hindered by a more fundamental problem, namely, the confining of the nonlocal kernel in the near-boundary regions of a finite domain. Therefore, we study two different types of nonlocal kernels, one bounded in the finite domain of the structure and the other, non-bounded. The results show that by using a three-dimensional nonlocal formulation, we can capture the non-classical influence of the structure's thickness on its bending stiffness. and this influence, highly depends on the bounding of the nonlocal kernel in the finite domain.

6.1. INTRODUCTION

Micro and nano electro-mechanical-systems (MEMS and NEMS) play key roles in a wide variety of modern applications, including nano-mechanical sensors, actuators, and many electronic devices. The performance of these devices is based on movements and deformations of their micro/nano mechanical components, such as cantilevers, double clamped beams or plates. Obviously, the further development of these devices requires a thorough understanding and modeling of their mechanical behavior. However, devices at nano-meter scale may exhibit mechanical properties not noticed at the macro-scale. Many theoretical methods such as molecular and atomistic simulations and size-dependent continuum theories are being developed to analyze this behavior. Molecular and atomistic simulations are generally time consuming and computationally expensive. Alternatively, continuum models offer superior computational efficiency.

Classical continuum mechanics is size independent and it cannot provide a good prediction for small scales. Therefore, size-dependent continuum theories have been introduced to account for these scaling effects [2, 3]. In an attempt to account for atomistic effects, these theories embed an internal material length scale. This makes it possible to qualify the size of a structure as “large” or “small” relative to its material length scale [2, 4, 5]. If “large”, then these theories should converge to classical continuum theory, and, otherwise, they should reflect the size-dependence.

One of the best-known size-dependent continuum theories is non-local continuum theory, initiated in a general notation by Piola in 1846 [6, 7]. In nonlocal continuum theory, a material point is influenced by the state of all points of the body. The mathematical description of this theory relies on the introduction of additional contributions in terms of “gradients” or “integrals” of the strain field in the constitutive equations. This, respectively, leads to so-called “weak” or “strong” non-local models [8–10]. Although both models have been found to be largely equivalent [11], the weak (gradient) formulation requires stronger continuity on the displacements gradients. In addition, in cases that a well-defined spatial interaction exists in the material, the strong (integral) approach is preferred, because it models the nonlocality in a more transparent way [11].

In strong nonlocal theories, particularly formulated by Kröner in 1967 [3], and then by Eringen in 1977 [2, 5], the point-to-point relationship between stresses and strains does not hold anymore. Instead, the stress in each point is influenced by the strain of all points of the body. This influence is captured by a spacial integral over the body. The integral is weighted with a decaying kernel, which is designed to incorporate the long-range interaction between atoms in the continuum model. With the spacial integral, the dimensions of the body are brought into the constitutive equations, and thus, the constitutive equations will be size-dependent.

It is worth to mention here that closely related to strong nonlocal theory, the *peridynamics* theory has been developed by Silling [10]. In fact, in peridynamics, instead of spatial differential operators, integration over differences of the displacement field is used to describe the existing, possibly nonlinear, forces between particles of the solid body [10, 12]. However, in contrast to the peridynamic theory, the strong non-local theories rely on spatial integrations. The present study mainly focuses on the

commonly used strong formulation given by Eringen.

The strong nonlocal theory has been used in many studies for modeling micro- nano-mechanical devices. In these studies, mechanical components such as thin-film elements and plate-like structures have been modeled with so-called *two-dimensional* non-local formulations, also known as “nonlocal plate theories” [13–15]. In these theories, the plate-like structures are generally modeled as a two-dimensional domain. In this way, the nonlocal contribution of the strain field in the transverse direction is ignored. Therefore, the size of a plate is only defined by its lateral dimensions, and thus, its thickness is not incorporated in its size-dependent behavior.

In plane stress problems, which are inherently two dimensional—such as the stress analysis near the crack tip in a thin plate [5]—ignoring the nonlocal effects in transverse direction is within reason. Also, for structures whose thickness is much smaller than the material length-scale, such as a monolayer graphene, the non-local effect in transverse direction is in fact meaningless [16]. However, modeling a plate as a two-dimensional domain and ignoring the nonlocal contribution in the transverse direction is not always valid. First of all, from a physical point of view, a nonlocal theory is supposed to incorporate the interaction between atoms in a continuum model and so its effect should exist in all directions [17]. Second, since the thickness of a plate is significantly smaller than its lateral dimensions, the length scale at which classical elasticity breaks down appears in the transverse direction first. Moreover, in problems in which there is a uniform strain field in the tangential directions, the nonlocal stress as a function of weighted average of strain in tangential directions is simply equal to the classical stress. This means the two-dimensional formulation fails to reflect any size-dependency. In such a case, it is likely that transverse non-locality would have a more pronounced size-dependence contribution.

In this chapter, we particularly investigate how the strong three dimensional non-local formulation can incorporate the plate thickness. Moreover, we study the effect of thickness in the predicted size dependence of the overall flexural rigidity and elastic modulus of the plate.

It is worth to note that in nonlocal elasticity, as a consequence of including contributions of integrals of the strain field in the constitutive equations, the differential order of the governing equations changes. This results in additional boundary conditions which should physically reflect the surface properties of the material/structure. The latter, however, has not been discussed rigorously in literature so far and instead, the boundaries are often avoided in the respective analyses. When a three dimensional nonlocal formulation is employed in the analysis of plates, these extra boundary conditions should be defined on the upper and lower surface of the plate. In order to investigate the significance of these boundary conditions, two different treatments of the boundaries will be addressed.

This chapter is structured as follows. In Section 6.2, the fundamentals of Eringen’s nonlocal elasticity theory, some important considerations and the basis of conventional nonlocal plate theory are reviewed. In Section 6.3, we will use a three dimensional nonlocal formulation to solve an example of uniformly deformed plate. For this purpose two types of boundary conditions will be applied for the nonlocal formulation. The results of this analysis will be discussed and compared to classical plate theory in Section 6.4. In the last section, the conclusions of this study will be

presented.

6.2. NONLOCAL ELASTICITY THEORY

In linear nonlocal elasticity, the stress tensor (\mathbf{t}) for a homogenous and continuous domain is determined as [2, 18]:

$$\begin{aligned} t_{ij}(\mathbf{x}) &= \int_{V_b} \alpha(|\mathbf{x} - \mathbf{x}'|, e_0 a) C_{ijkl} \varepsilon_{kl}(\mathbf{x}') dV(\mathbf{x}') \\ &= \int_{V_b} \alpha(|\mathbf{x} - \mathbf{x}'|) \sigma_{ij}(\mathbf{x}') dV(\mathbf{x}') \end{aligned} \quad (6.1)$$

where $\varepsilon_{kl}(\mathbf{x}')$ are the classical Cauchy's strain components at the point \mathbf{x}' and C_{ijkl} are the components of the elasticity tensor. Index k and l are the dummy index in Einstein's summation convention, and Cartesian coordinates have been assumed. The product of these two terms can be simply substituted with classical stress component $\sigma_{ij}(\mathbf{x}')$, as in the second line. Then, V_b is the volume of the body at hand. The function $\alpha(|\mathbf{x} - \mathbf{x}'|, e_0 a)$ is the non-local kernel representing the effect of long-range interactions [10]. This radial kernel reflects the nonlocal contribution of strain in all points \mathbf{x}' of the body. The nonlocal kernel α is also a function of parameters a and e_0 . The parameter a is the material characteristic length scale (e.g. atomic distance, lattice parameter, granular distance) [13], and e_0 is a constant for adjusting the model to match experiments or other models [5, 14, 17]. Other properties of the nonlocal kernel α will be discussed later in this section.

It should be stressed that the proof of existence of Cauchy's stress tensor is based on the equilibrium of contact forces with a force which is assumed to be continuous in space. We may use a similar assumption as well (as proposed in [6, 7]). Moreover, in strain gradient nonlocal theories, the constitutive equations are much more than one stress-strain relationship. Instead, so-called *double* or *hyper* stress components are defined associated to higher order strain gradients [19]. In the strong nonlocal theory, however, the basic equations for an isotropic solid can be expressed in its simplest form as in Equation 6.1 [2, 3, 8–11].

Accordingly, the nonlocal strain energy is expressible as [5]:

$$U_{nonlocal} = \frac{1}{2} \int_{V_b} t_{ij} \varepsilon_{ij} dV. \quad (6.2)$$

Please note that this formulation of internal energy is a particular case of the formulation given by Kröner [3], provided that the kernel α reflects the local (short-range) as well the nonlocal (long-range) effects. The equilibrium equations in the nonlocal continuum theory are the same as for classical continuum theory, but represented in terms of the nonlocal stresses (t_{ij}) rather than the local stresses (σ_{ij}).

6.2.1. NONLOCAL KERNEL

The function used as the nonlocal kernel ($\alpha(|\mathbf{x} - \mathbf{x}'|, e_0 a)$) needs to have the following characteristic properties;

- 1- To reflect the properties of atomistic long term interactions correctly, it acquires its maximum at $\mathbf{x} = \mathbf{x}'$ and monotonically decreases with $|\mathbf{x} - \mathbf{x}'|$.
- 2- To ensure that classical elasticity is included in the limit of a vanishing internal characteristic length, it must tend to Dirac's delta function when $e_0 a \rightarrow 0$. [18], i.e.

$$\lim_{e_0 a \rightarrow 0} \alpha(|\mathbf{x} - \mathbf{x}'|, e_0 a) = \delta(|\mathbf{x} - \mathbf{x}'|). \quad (6.3)$$

- 3- The stress at \mathbf{x} should have the same contribution to the stress at \mathbf{x}' as *vice versa*, thus, the nonlocal kernel is symmetric in its arguments \mathbf{x}' and \mathbf{x} , i.e. $\alpha(\mathbf{x}, \mathbf{x}') = \alpha(\mathbf{x}', \mathbf{x})$.

- 4- According to Eringen's nonlocal continuum theory [2], the function α is normalized in the volume of the body (V_b):

$$\int_{V_b} \alpha(|\mathbf{x} - \mathbf{x}'|) dV(\mathbf{x}') = 1. \quad (6.4)$$

This property assures that a uniform local strain field should also result in a uniform nonlocal stress field (See Equation 6.1), provided that the material is isotropic and homogeneous [20]. If the domain of the body at hand is large enough to be considered as an infinite domain, then this feature implies that α is always normalized on such an infinite domain. It should be noted that nonlocal kernels have an effective influence zone, V_e , centered around \mathbf{x} and an effective cut-off length, L_e [17, 18]. Outside this influence zone, the function $\alpha(x - x')$ practically vanishes and, thus, it can be assumed that

$$\int_{V_e} \alpha(|\mathbf{x} - \mathbf{x}'|) dV(\mathbf{x}') \simeq \int_{V_\infty} \alpha(|\mathbf{x} - \mathbf{x}'|) dV(\mathbf{x}') = 1. \quad (6.5)$$

Many kernels have been suggested in literature with the above mentioned properties, and in general, all these kernels qualitatively lead to similar results [18, 21]. However, for a kernel with these properties, in points closer than its cut-off length (L_e) to the boundary, the influence zone of the kernel exceeds the boundary. Consequently, it only collects the nonlocal influence of the points \mathbf{x}' inside the body (see Figure 6.1-a). Thus, the normalization condition would not be satisfied anymore.

To satisfy the normalization condition, either the analysis domain should be far from boundaries [2], and then we can use the common kernels; or, a modified bounded nonlocal kernel should be used. The shape of such a kernel is modified near boundaries such that it satisfies the normalization condition based on all material points

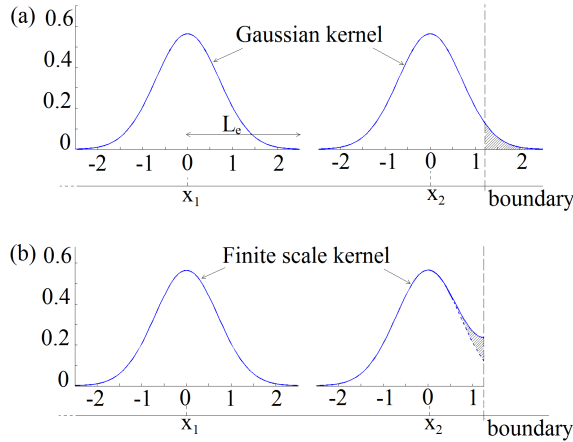


Figure 6.1: A schematic representation of one-dimensional kernels at two points within the body (x_1) and near the boundary region (x_2): (a) Gaussian density function, normalized on an infinite domain; (b) A bounded kernel which adapts its shape when the effective influence zone includes a boundary.

6

available (Figure 6.1-b) [4, 11, 22, 23]. It is worth noting that the kernel function in such an expression cannot not be a function of $|\mathbf{x} - \mathbf{x}'|$ any more, but \mathbf{x} and \mathbf{x}' .

It should be noted that bounding the nonlocal kernel in the finite domain of the body, results in bringing the dimensions and perhaps the shape of of the body into the definition of the nonlocal kernel. In order to introduce this modification to the nonlocal kernel mathematically, we first need to specify the final property of the kernel α .

5- The final feature of the function α , is an assumption, and physically speaking it is not really required [18]. It is assumed that the kernel α is the Green's function of an operator L . In other words, it is supposed that an operator L can be found for any kernel α where:

$$L\alpha(|\mathbf{x}, \mathbf{x}'|) = \delta(|\mathbf{x}, \mathbf{x}'|). \quad (6.6)$$

The later, as a matter of fact, is an assumption to convert integral equations to differential equations. Such an operator L can be used to relate the non-local stress to the local stress. Applying L to Equation 6.1 would yield:

$$Lt_{ij} = \sigma_{ij}. \quad (6.7)$$

Therefore, a choice of kernel implicitly defines a differential operator which transforms the non-local stress to the local one [20]. Equation 6.7 is commonly used instead of the definition given in Equation 6.1.

As a matter of fact, for solving Equations 6.7, one has to impose boundary conditions on t_{ij} . It should be reminded that Green's function of a boundary value problem should also satisfy the boundary conditions of the problem. Therefore, these

boundary conditions are actually the tools to change the shape of the kernel in the near-boundary regions, as schematically shown in Figure 6.1-b.

In literature, most of the suggested operators L are second-order operators [18]. For the resulted second-order differential equation, the required boundary conditions involve either the zeroth- or first-order derivatives of the function. Thus, as an appropriate boundary condition for Equation 6.7, either the value of nonlocal stress components, their derivatives, or a linear combination of these two must be defined on the boundary. Fixing the stress components (t_{ij}) on the boundaries does not have any physical motivation. Hence, homogeneous or inhomogeneous boundary conditions on the first derivative of the stress components (e.i. Neumann B.C.) shall be employed.

Although the boundary conditions on the nonlocal kernel, which indicate the extra boundary conditions on the stress derivatives, are key elements in nonlocal elasticity, they are discussed in very few studies. In most publications, non-bounded kernels are used; and the boundary effects (like in Fig. 6.1-a,) are justified by the surface effects [4]. In a few studies, a homogeneous Neumann boundary condition is applied on the nonlocal kernel [4, 11, 23]. However, there is no discussion on the connection between the suggested mathematical boundary conditions and the underlying physics.

It should be mentioned that the added boundary conditions are a challenging problem in so-called weak nonlocal or higher order elasticity theories, as well. In strain gradient elasticity, for example, these boundary conditions automatically appear either for the second order gradient of the displacement components or associated *double stress* (i.e. the partial derivative of energy density to strain gradients) [19]. Although a clear interpretation of the mentioned boundary conditions is not provided in this theory either, it has been shown that the strain gradient and nonlocal formulation are largely equivalent *if* the appropriate boundary conditions are employed for the nonlocal kernel [11].

It is the authors' opinion that the boundary conditions on the nonlocal kernel should reflect the surface properties of the material/structure. From a physics point of view, the nonlocal kernel is supposed to incorporate the long range interactions of atoms into continuum mechanics. Hence, if its shape is varying near boundaries, it should result from the rearrangement of atoms near the surface of the pristine material. In addition, there are fewer possibilities for interaction between atoms near the surface, and this should also be reflected in the model.

We should keep in mind that the extra boundary conditions become very relevant in applying nonlocal elasticity to a plate. In such a case, the relevant boundaries are the lateral surfaces, for which the additional boundary conditions on the stress or the kernel should be defined. In this chapter, we investigate the difference between the predicted mechanical response of the plate, when applying a non-bounded kernel (Fig. 6.1-a), or, a bounded one using a homogeneous Neumann boundary condition (Fig. 6.1-b). This is done for an example of uniform deformation of a plate.

6.2.2. CONVENTIONAL NONLOCAL PLATE THEORIES

In nonlocal elasticity, as described above, all formulations are three-dimensional. The points \mathbf{x} and \mathbf{x}' are arbitrary points in space and the integrals in Equations 6.1–6.2

involve the entire volume of the body. The kernel function α is a three-dimensional kernel, i.e. it reflects the nonlocal contribution of the strain field in all directions and its dimension is m^{-3} .

For thin plates, however, many studies have modeled the plate as a two-dimensional domain. In such models, the points \mathbf{x} and \mathbf{x}' are arbitrary points of the mid-plane of the plate and the integrals are taken over the surface area of the plate. The nonlocal kernel in such a model is a two-dimensional function, ignoring the components with respect to the transverse direction (z) [13–15, 24–26]. The dimension of a two-dimensional kernel is m^{-2} and it is normalized over the the area of the plate.

With above mentioned assumptions in the nonlocal plate theory, the nonlocal stress is defined as [15]:

$$\bar{t}_{ij}(\mathbf{x}) = \int_A \alpha(|\mathbf{x} - \mathbf{x}'|) \bar{\sigma}_{ij}(\mathbf{x}') dA(\mathbf{x}'), \quad (6.8)$$

where A is the surface area of the plate and i and j denote the in-plane coordinates. The over-line is employed specifically for vector form indication of the nonzero components of the second order tensors of stress and strain in the plate. The tangential resultants of stress (\mathbf{N}_{nl}) are then calculated by integrating the nonlocal stress components along the transverse direction (z) in the limits of plate thickness (h). Considering that $\alpha(|\mathbf{x}' - \mathbf{x}|)$ is not a function of z and, thus, it does not affect any integration in transverse direction, the tangential stress resultants and tangential stress couples can be written as:

$$\begin{aligned} \mathbf{N}_{nl} &= \int_h \bar{\mathbf{t}} dz \\ &= \int_h \left(\int_A \alpha(|\mathbf{x} - \mathbf{x}'|) \bar{\boldsymbol{\sigma}}(\mathbf{x}') dA(\mathbf{x}') \right) dz \\ &= \int_A \left(\int_h \alpha(|\mathbf{x} - \mathbf{x}'|) \bar{\boldsymbol{\sigma}}(\mathbf{x}') dz \right) dA(\mathbf{x}') \\ &= \int_A \alpha(|\mathbf{x} - \mathbf{x}'|) \left(\int_h \bar{\boldsymbol{\sigma}}(\mathbf{x}') dz \right) dA(\mathbf{x}') \\ &= \int_A \alpha(|\mathbf{x} - \mathbf{x}'|) \mathbf{N}^{cl}(\mathbf{x}') dA(\mathbf{x}'), \end{aligned} \quad (6.9)$$

and similarly the tangential stress couples (\mathbf{M}_{nl}) can be calculated as:

$$\begin{aligned} \mathbf{M}_{nl} &= \int_h \bar{\mathbf{t}} z dz \\ &= \int_A \alpha(|\mathbf{x} - \mathbf{x}'|) \int_h \bar{\boldsymbol{\sigma}}(\mathbf{x}') z dz dA(\mathbf{x}') \\ &= \int_A \alpha(|\mathbf{x} - \mathbf{x}'|) \mathbf{M}^{cl}(\mathbf{x}') dA(\mathbf{x}'). \end{aligned} \quad (6.10)$$

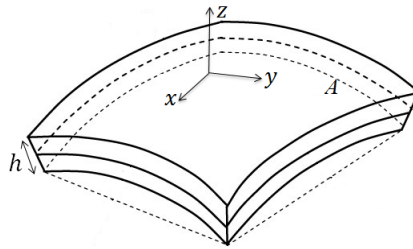


Figure 6.2: deflection of the plate with thickness h and surface area A .

In these equations \mathbf{N}^{cl} and \mathbf{M}^{cl} are the tangential stress resultant and couples from the classical plate theory. The equations of motion are then identical as for the classical Kirchhoff plate theory, but based on the nonlocal tangential stress resultants and couples.

Notice that based on Equations 6.9 and 6.10, in nonlocal plate theories, the nonlocal tangential stress resultants and couples do not have any nonlocal contributions from the transverse direction. Therefore, the thickness of the plate does not have any influence on the size-dependency of the result. Considering that the kernel function is normalized over the area, if \mathbf{N}^{cl} and \mathbf{M}^{cl} are uniform in the plate, there would be no difference between the nonlocal and classical tangential stress resultants and couples, and therefore, the two solutions (classical and nonlocal) would predict similar mechanical responses.

This model is valid for inherently two dimensional plane-stress problems, where there is no variation of the classical stress field through the thickness. Otherwise, it cannot be motivated on the basis of the fundamentals of nonlocal theory or physics. However, it has been the basis of nonlocal plate theory which is commonly used for solving many other problems related to plates, where the stress varies through the thickness, as well.

6.3. EFFECTS OF THICKNESS IN NONLOCAL PLATE THEORY

In this section, using an example of a plate with both a uniform stretch and a uniform curvature, the effect of thickness in nonlocal plate theory is studied. In fact, we use a three-dimensional nonlocal formulation in order to calculate the tangential resultant stresses and couples induced by such a deformation in the plate. With this solution we shall study the effect of thickness of the plate on its mechanical response as predicted by nonlocal elasticity theory. Moreover, we will compare the results with the classical plate theory. The solution discussed here can be extended to a plate with non-uniform deformation, as well.

Assume a plate with a uniform thickness h , and lateral area A (Figure 6.2). The lateral dimensions of the plate are much larger than its thickness. The mid-plane of the plate is subjected to both a uniform curvature κ and stretch γ (Figure 6.2). Using classical plate theories (based on plane-stress assumptions), the tangential strain ϵ

at the interior of the plate, i.e. sufficiently far away from the edges, is described as

$$\bar{\boldsymbol{\varepsilon}} = \begin{pmatrix} \varepsilon_{xx} \\ \varepsilon_{yy} \\ 2\varepsilon_{xy} \end{pmatrix} = \begin{pmatrix} \gamma_{xx} \\ \gamma_{yy} \\ 2\gamma_{xy} \end{pmatrix} - z \begin{pmatrix} \kappa_{xx} \\ \kappa_{yy} \\ 2\kappa_{xy} \end{pmatrix}, \quad (6.11)$$

where x and y denote the tangential coordinates. The transverse coordinate is z , and the midplane coincides with $z = 0$. Using classical linear constitutive equations, the classical tangential stresses follow as

$$\bar{\boldsymbol{\sigma}} = \begin{pmatrix} \sigma_{xx} \\ \sigma_{yy} \\ \sigma_{xy} \end{pmatrix} = \mathbf{Q}\bar{\boldsymbol{\varepsilon}}, \quad (6.12)$$

where \mathbf{Q} represents the elasticity tensor for a homogeneous and isotropic material and in a plane-stress problem:

$$\mathbf{Q} = \frac{E}{1-\nu^2} \begin{pmatrix} 1 & \nu & 0 \\ \nu & 1 & 0 \\ 0 & 0 & \frac{1-\nu}{2} \end{pmatrix} \quad (6.13)$$

where E is the Young's modulus and ν is the Poisson ratio of the material. As a result, the nonlocal stress can be calculated:

$$\bar{\mathbf{t}} = \int_V \alpha(|\mathbf{x} - \mathbf{x}'|) \mathbf{Q}(\boldsymbol{\gamma} - z' \boldsymbol{\kappa}) dV(\mathbf{x}'). \quad (6.14)$$

It is worth noting that the classical plane-stress assumption ($\sigma_{zz} = 0$) as adopted in classical plate theory, now has directly lead us to a plane-stress condition for the nonlocal stresses as well ($t_{zz} = 0$). In particular, we can employ Equation 6.1 to explicitly prove this case:

$$\begin{aligned} \bar{t}_{zz}(\mathbf{x}) &= \int_{V_b} \alpha(|\mathbf{x} - \mathbf{x}'|) \bar{\sigma}_{zz}(\mathbf{x}') dV(\mathbf{x}') \\ &= \int_{V_b} \alpha(|\mathbf{x} - \mathbf{x}'|) (0) dV(\mathbf{x}') = 0. \end{aligned} \quad (6.15)$$

In addition, we stress here that imposing the plane-stress assumption on the nonlocal stresses ($t_{zz} = 0$) will also result in plane-stress condition for the classical stress components ($\sigma_{zz} = 0$), provided that the kernel α is a positive definite function.

For deriving \mathbf{t} in Equation 6.14, the appropriate nonlocal kernel $\alpha(|\mathbf{x}' - \mathbf{x}|)$ should be chosen. Here, a three-dimensional Gaussian function is chosen as the nonlocal kernel $\alpha(|\mathbf{x}' - \mathbf{x}|)$:

$$\alpha(|\mathbf{x} - \mathbf{x}'|) = \frac{1}{(\pi(e_0 a)^2)^{\frac{3}{2}}} \exp\left(-\frac{|\mathbf{x} - \mathbf{x}'|^2}{(e_0 a)^2}\right). \quad (6.16)$$

This function has been reported to show an excellent agreement with the atomic dispersion curves of crystalline materials [2, 17]. The Gaussian density function is Green's function of the diffusion (or heat) equation in an infinite domain:

$$\nabla^2 t - \frac{\partial t}{\partial \tau} = 0, \quad (6.17)$$

where, $\tau = \frac{(e_0 a)^2}{4}$. We can also derive Green's function of the mentioned equation in a bounded domain by applying appropriate boundary conditions as discussed in Section 6.2.1. Here, both solutions with bounded and unbounded kernels are presented for the example at hand.

6.3.1. GAUSSIAN KERNEL

To begin with, we neglect the nonlocal boundary effects in all boundaries of the plate and consider the unbounded kernel as in Equation 6.16. Without the boundary effects, the shape of the nonlocal kernel would be similar in all material points in different positions. A one-dimensional schematic of this kernel is shown in Figure 6.1-a. As this figure shows, the kernels are similar at the point $\mathbf{x} = \mathbf{x}_1$ within the body, and at $\mathbf{x} = \mathbf{x}_2$ where the influence length of the kernel exceeds the boundary. By using Equations 6.14 and 6.16, and by decoupling between in-plane and transverse directions, the nonlocal in-plane stress can be expressed as:

$$\begin{aligned} \bar{\mathbf{t}} &= \int_A \int_{-h/2}^{h/2} \alpha(|\mathbf{x} - \mathbf{x}'|) \mathbf{Q}(\boldsymbol{\gamma} - z' \boldsymbol{\kappa}) dz' dA' \\ &= \int_x \int_y \frac{\exp\left(-\frac{(x-x')^2 + (y-y')^2}{(e_0 a)^2}\right)}{(\sqrt{\pi} e_0 a)^2} dx' dy' \times \\ &\quad \int_{-h/2}^{h/2} \mathbf{Q}(\boldsymbol{\gamma} - z' \boldsymbol{\kappa}) \frac{\exp\left(-\frac{(z-z')^2}{(e_0 a)^2}\right)}{(\sqrt{\pi} e_0 a)} dz' \end{aligned} \quad (6.18)$$

Notice that the function inside the first integral is a two-dimensional Gaussian kernel itself and is normalized on an infinite area. As mentioned before, the lateral geometries of the plate are considered to be much larger than its thickness and the plate dimensions can be assumed as infinite. In other words, near-boundary regions in these two directions can be ignored relative to their dimensions. Therefore, the first integral equals to unity almost everywhere in the plate, and nonlocal stress can be simplified to the second integral only:

$$\bar{\mathbf{t}} \simeq \int_{-h/2}^{h/2} \mathbf{Q}(\boldsymbol{\gamma} - z' \boldsymbol{\kappa}) \frac{\exp\left(-\frac{(z-z')^2}{(e_0 a)^2}\right)}{(\sqrt{\pi} e_0 a)} dz'. \quad (6.19)$$

In fact, this result is valid in the points sufficiently far away from the edges. Note that due to the assumed uniformity of curvature and stretch, in-plane dimensions

vanish from the equations and only the integration in transverse direction remains. Of course, for non-uniform deformation (i.e. $\boldsymbol{\kappa}(x, y)$ and $\boldsymbol{\gamma}(x, y)$), the in-plane non-locality would also remain in the formulations. The nonlocal stress can be solved and simplified to

$$\begin{aligned} \bar{\mathbf{i}} = & \mathbf{Q}\boldsymbol{\gamma} \left(\frac{1}{2} \left(\operatorname{erf}\left(\frac{z+h/2}{e_0 a}\right) - \operatorname{erf}\left(\frac{z-h/2}{e_0 a}\right) \right) \right) \\ & - \mathbf{Q}\boldsymbol{\kappa} \left(\frac{1}{2} z \left(\operatorname{erf}\left(\frac{z+h/2}{e_0 a}\right) - \operatorname{erf}\left(\frac{z-h/2}{e_0 a}\right) \right) \right. \\ & \quad \left. - \frac{1}{2} \frac{e_0 a}{\sqrt{\pi}} \left(\exp\left(-\frac{(z-h/2)^2}{(e_0 a)^2}\right) \right. \right. \\ & \quad \left. \left. - \exp\left(-\frac{(z+h/2)^2}{(e_0 a)^2}\right) \right) \right), \end{aligned} \quad (6.20)$$

where erf is the error function. Notice that the choice of not normalizing the kernel function α results in a non uniform in-plane stress over the thickness even for the case of a uniform stretch (i.e., $\boldsymbol{\kappa} = 0$). Next, we can calculate the tangential stress resultants and couples in the plate:

$$\begin{aligned} \mathbf{N}_{\text{nl}} &= \int_{-h/2}^{h/2} \bar{\mathbf{i}} dz \\ &= h\mathbf{Q}\boldsymbol{\gamma} \left(\operatorname{erf}(\eta) + \frac{1}{\eta\sqrt{\pi}} (\exp(-\eta^2) - 1) \right), \end{aligned} \quad (6.21)$$

$$\begin{aligned} \mathbf{M}_{\text{nl}} &= \int_{-h/2}^{h/2} \bar{\mathbf{i}} z dz = \\ & \frac{h^3}{12} \mathbf{Q}\boldsymbol{\kappa} \left(\operatorname{erf}(\eta) - \frac{1}{\sqrt{\pi}} \left(\frac{2}{\eta} \exp(-\eta^2) \right. \right. \\ & \quad \left. \left. + (3\eta^{-1} - 2\eta^{-3})(1 - \exp(-\eta^2)) \right) \right). \end{aligned} \quad (6.22)$$

The parameter $\eta = \frac{h}{e_0 a}$, which is the thickness normalized with the internal length scale of the material is introduced to simplify the formulations. Equations 6.21 and 6.22 can also be written as:

$$\mathbf{N}_{\text{nl}} = \lambda \mathbf{A}\boldsymbol{\gamma}, \quad (6.23)$$

$$\mathbf{M}_{\text{nl}} = \beta \mathbf{D}\boldsymbol{\kappa}. \quad (6.24)$$

Here, λ and β are introduced as the nonlocal modification factors on classical extensional (or membrane) stiffness matrix ($\mathbf{A} = h\mathbf{Q}$) and bending stiffness matrix $\mathbf{D} = \frac{h^3}{12}\mathbf{Q}$,

respectively. These factors can be explicitly defined using the following equations:

$$\begin{aligned}\lambda &= \frac{1}{h} \int_{-h/2}^{h/2} \int_{-h/2}^{h/2} \alpha(|z-z'|) dz' dz \\ &= \frac{1}{\eta\sqrt{\pi}} (\exp(-\eta^2) - 1) + \operatorname{erf}(\eta),\end{aligned}\quad (6.25)$$

and,

$$\begin{aligned}\beta &= \frac{12}{h^3} \int_{-h/2}^{h/2} \int_{-h/2}^{h/2} -z' z \alpha(|z-z'|) \\ &= \operatorname{erf}(\eta) - \frac{1}{\sqrt{\pi}} \left(\frac{2}{\eta} \exp(-\eta^2) \right. \\ &\quad \left. + (3\eta^{-1} - 2\eta^{-3})(1 - \exp(-\eta^2)) \right).\end{aligned}\quad (6.26)$$

Note that a thickness of a plate that is large relative to the internal length scale (i.e., when $\eta \rightarrow \infty$), results in nonlocal modification factors that converge to 1 and therefore, nonlocal theory converges to classical plate theory. This result will be discussed in the Section 6.4 (Results and Discussion).

The nonlocal modification factors λ and β were calculated assuming a uniform deformation of the plate. If a non-uniform stretch $\boldsymbol{\gamma}(x, y)$ and curvature $\boldsymbol{\kappa}(x, y)$ are assumed in Equation 6.11, the in-plane strain terms can also be expressed by $\boldsymbol{\varepsilon}(x, y)$. Using a similar formulation to Equations 6.12 to 6.22, to describe the nonlocal elasticity, results in nonlocal stress resultants and stress couples like:

$$\begin{aligned}\mathbf{N}_{\mathbf{nl}} &= \int_A \mathbf{A}\boldsymbol{\gamma}(x, y) \frac{\exp\left(-\frac{(x-x')^2+(y-y')^2}{(e_0 a)^2}\right)}{(\sqrt{\pi}e_0 a)^2} dx' dy' \\ &\times \frac{1}{h} \int_Z \int_Z \frac{\exp\left(-\frac{(z-z')^2}{(e_0 a)^2}\right)}{(\sqrt{\pi}e_0 a)} dz' dz,\end{aligned}\quad (6.27)$$

$$\begin{aligned}\mathbf{M}_{\mathbf{nl}} &= \int_A -\mathbf{D}\boldsymbol{\kappa}(x, y) \frac{\exp\left(-\frac{(x-x')^2+(y-y')^2}{(e_0 a)^2}\right)}{(\sqrt{\pi}e_0 a)^2} dx' dy' \\ &\times \frac{12}{h^3} \int_Z \int_Z \frac{\exp\left(-\frac{(z-z')^2}{(e_0 a)^2}\right)}{(\sqrt{\pi}e_0 a)} z' z dz' dz\end{aligned}\quad (6.28)$$

The stress resultants, as well as stress couples, consist of two terms; the first term is due to in-plane non-locality, which resembles Equations 6.9 and 6.10 and can be treated using existing nonlocal plate theories. The second terms in both equations are created by out of plane non-locality, and resemble the modification factor λ and β from Equations 6.25 and 6.26. This suggests that the same modification factors on the extensional and bending stiffness matrices can be introduced to conventional nonlocal plate theories, to argument them by a dependency on the plate thickness.

6.3.2. BOUNDED KERNEL

In Section 6.3.1, it was shown that only transverse non-locality has a dominant contribution in the nonlocal stress state in a uniformly deformed plate. For simplicity in this part, we use a one-dimensional nonlocal formulation in transverse direction only.

As mentioned before, the nonlocal kernel should be normalized in the volume of the structure at hand. Most kernels suggested in literature are derived for infinite domains. Therefore, these kernels are not normalized anymore in the near-boundary regions, where their influence zone exceeds the boundary. As an alternative solution, to ensure that Equation 6.4 holds everywhere in the body, one can benefit from the operator L mentioned in Equation 6.6. Particularly, the Green's function of such an operator in a boundary value problem is always normalized in the solution domain, and thus, it can still be employed as the nonlocal kernel [4, 11].

Similar to previous section, the Green's function of the diffusion equation (Equation 6.17) is chosen as the nonlocal kernel. As mentioned in Section 6.2.1, the homogeneous natural boundary condition (Neumann) is applied on Equation 6.17, and consequently, on its Green's function. This boundary condition is applied to the top and bottom surfaces of the plate ($z = \frac{h}{2}$ and $z = -\frac{h}{2}$):

$$\frac{\partial \alpha_h(\frac{h}{2}, z')}{\partial z'} = \frac{\partial \alpha_h(-\frac{h}{2}, z')}{\partial z'} = 0, \quad (6.29)$$

where α_h is the kernel bounded in $[-\frac{h}{2}, \frac{h}{2}]$. The solution of such a boundary value problem for any z and z' in $[-\frac{h}{2}, \frac{h}{2}]$ is [27]:

$$\alpha_h(z, z') = \sum_{n=-\infty}^{\infty} (\alpha(z - z' - 2nh) + \alpha(z + z' - (2n - 1)h)), \quad (6.30)$$

where α is unbounded Green's function of the diffusion equation in an infinite domain, which is the Gaussian density function given by Equation 6.16.

The bounded kernel α_h is plotted in Figure 6.3 for three different locations with respect to the boundaries. As shown in Figure 6.3, the shape of the function α_h changes in regions near the boundaries such that the function remains normalized inside the volume of the structure. In other words: for any point z in $[-\frac{h}{2}, \frac{h}{2}]$, the following condition is satisfied:

$$\int_{-\frac{h}{2}}^{\frac{h}{2}} \alpha_h(z, z') dz' = 1. \quad (6.31)$$

By substituting the kernel given in Equation 6.30, into Equation 6.14, the nonlocal stress terms are calculated. Consequently, the nonlocal tangential stress resultants and stress couples in the plate can be determined. As a result, a similar nonlocal modification factor λ_h and β_h on the extensional and bending stiffness matrices can

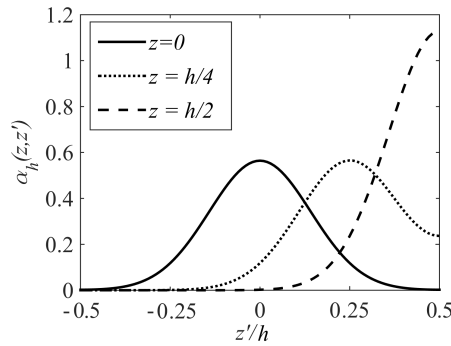


Figure 6.3: The Green's function of bounded diffusion equation for different locations and, for the case $h = 5e_0a$. The shape of the kernel varies so that it satisfies the boundary conditions and stays normalized.

be determined. Due to similarity of the procedure to the previous section, we avoid to repeat the whole calculations here. Accordingly, λ_h and β_h can be calculated using the following equations:

$$\lambda_h = \frac{1}{h} \int_Z \int_{Z'} -\alpha_h(z, z') dz' dz = 1, \quad (6.32)$$

$$\beta_h = \frac{12}{h^3} \int_Z \int_{Z'} -\alpha_h(z, z') z' z dz' dz. \quad (6.33)$$

Notice that normalizing the kernel function results in a modification factor for the stress resultant that is equal to 1, and the stress resultant $\mathbf{N}_{\mathbf{n}}$ is similar to that of the classical plate theory. This will be discussed and compared to the result of the calculations with a Gaussian kernel, in “Results and Discussion”. It should be mentioned that the Green's function of the three dimensional diffusion equation in a finite domain is not separable, i.e. it cannot be decoupled mathematically in-plane and out-of-plane terms, as for the Gaussian kernel. Therefore, the effect of out-of-plane and in-plane non-locality cannot be separated anymore. Considering that for plates with semi-infinite geometry in tangential directions, the kernel needs to be bounded only in z direction. Thus, we introduce a new three-dimensional kernel:

$$\alpha'_h(\mathbf{x}, \mathbf{x}') = \frac{\exp\left(-\frac{(x-x')^2 + (y-y')^2}{(e_0a)^2}\right)}{(\sqrt{\pi}e_0a)^2} \times \sum_{n=-\infty}^{\infty} \left(\alpha(z-z' - 2nh) + \alpha(z+z' - (2n-1)h) \right). \quad (6.34)$$

The new kernel is only bounded in transverse direction. Using the same process mentioned in the previous section, the new type of kernel can be employed to calcu-

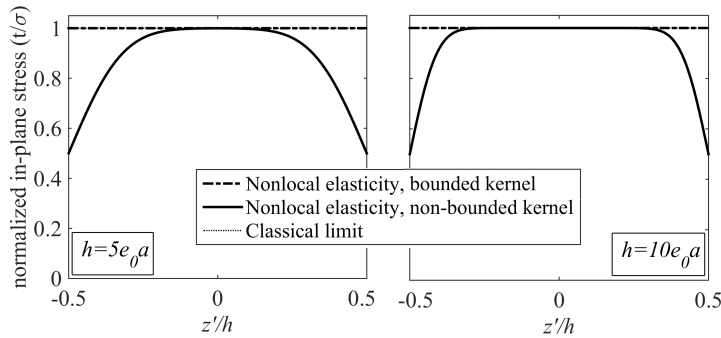


Figure 6.4: Normalized in-plane stress due to one dimensional stretch, corresponding to the nonlocal solutions for two different kernels and two different thicknesses $h = 10e_0a$ and $h = 5e_0a$. The transverse coordinate is normalized by the material length scale.

late the modification factor for the stiffness matrices (λ_h and β_h). These modification factor can be used to correct for the effects of thickness in the existing nonlocal plate theories, in problems with nonuniform deformations.

6

6.4. RESULTS AND DISCUSSION

In Section 6.3, using the strong nonlocal formulation, also known as Eringen's nonlocal theory, the tangential stress resultants and stress couples were calculated in a plate with a uniform deformation. In order to consider the non-locality in all directions, this calculation was performed with a three-dimensional kernel. It was shown that for a very thin plate, of which the lateral geometries are much larger than its thickness, the only remaining terms of the kernel are the ones expressing non-locality in transverse direction. It is emphasized that existing nonlocal beam or plate theories only account for in-plane non-locality in their formulation [14, 15, 24–26]. As mentioned in the Introduction, the reason for this common omission is that the nonlocal plate theories were initially introduced for inherently plane-stress problems, where the strain variation is the most significant in in-plane directions. As a result, the non-locality along the thickness could be ignored. In bending of plates, however, the strain gradient in the transverse direction is substantial. Consequently, this makes the effect of non-locality significant in that direction.

In this section, the effect of including the transverse non-locality on the stress and effective stiffness of the plate is discussed. First, consider a simple example of one-dimensionally stretched plate (i.e., $\boldsymbol{\gamma} = [\gamma \ 0 \ 0]$, $\boldsymbol{\kappa} = [0 \ 0 \ 0]$). Figure 6.4 shows the distribution of the tangential nonlocal stress in transverse direction for this example. Both solutions in Figure 6.4 (with bounded and non-bounded kernels) are normalized by the uniform stress as calculated by classical plate theory. As mentioned before, if the kernel is bounded and normalized in the domain, it ensures that a uniform strain field introduces a uniform stress field in the domain. Therefore, the nonlocal stress as calculated by a bounded kernel is uniformly distributed in the

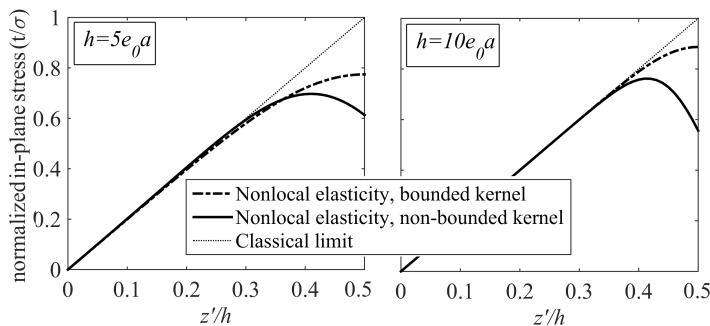


Figure 6.5: Normalized in-plane stress due to cylindrical bending, corresponding to the nonlocal solutions for two different kernels and two different thicknesses $h = 10e_0a$ and $h = 5e_0a$. The transverse coordinate is normalized by the material length scale.

thickness and is similar to the classical stress.

The nonlocal stress, as calculated with non-bounded kernel, is not uniform in the transverse direction. On the contrary, it has a sharp decrease near the surfaces of the plate. This sharp decrease of the lateral stress in the two surfaces of the structure is independent of the thickness and it always reduces to half of the classical stress. This is because for $z = h/2$ and $z = -h/2$, half of the nonlocal kernel exceeds the boundary and the other half is collecting the influence of the uniform strain inside the body. This behavior does not indeed describe physics or fundamentals of surface elasticity, and supports the reason behind the principle of normalization of the kernel in nonlocal theory.

Figure 6.5 shows the distribution of the tangential nonlocal stress in transverse direction, in a simple example of cylindrical bending of a plate (i.e., $\boldsymbol{\kappa} = [\kappa \ 0 \ 0]$, $\boldsymbol{\gamma} = [0 \ 0 \ 0]$). Both solutions (with bounded and non-bounded kernels) are normalized by the maximum stress as calculated by classical plate theory.

As can be observed in Figure 6.5, the nonlocal in-plane stress does not vary linearly in the thickness of the plate as it does in the classical solution. The nonlocal stress in the near-boundary region is lower than the classical stress. This difference increases when the thickness of the plate gets smaller. However, inside the body, i.e. far enough from the boundaries, the difference between classical and nonlocal solutions vanishes. The length of the boundary region in which this difference is significant, is very close to the effective cut-off length of the kernel ($2e_0a$). Including the transverse nonlocality in the formulation, allows us to indicate some surface effects in elasticity of the structure.

There is a considerable difference between the nonlocal solutions with a non-bounded kernel and with a bounded kernel. When using a non-bounded kernel, the in-plane stress shows a sharp reduction near the surface which does not reflect a physical behavior. In contrast, the in-plane stress derived with a bounded kernel has a smooth increase near the surface.

The modification factors λ and β on the extensional and bending matrices stiffness were calculated in Section 6.3. These modification factors only include the effect of non-locality in the transverse direction. Therefore, they only depend on the

plate's thickness h . Figure 6.6 shows the modification factor λ as a function of non-dimensional thickness η . If the chosen kernel is not bounded in transverse direction, the extensional stiffness of the plate is influenced by its thickness. Such a formulation predicts a softening when the thickness gets comparable to the material length scale. When the thickness of the plate is large, then the modification factor tends to unity which means stiffness will approach the classical limit $\mathbf{A} = h\mathbf{Q}$.

On the other hand, the bounded nonlocal kernel results in a constant extensional stiffness for the plate. As mentioned before, a uniform tensile strain in the plate, using a bounded kernel would result in a uniform nonlocal tensile stress equal to the classical stress. Therefore, the nonlocal solution with bounded kernel does not indicate the effective tensile modulus to change with the thickness.

Figure 6.7 shows the modification factor β for the nonlocal bending stiffness as a function of non-dimensional thickness η . When the thickness of the plate is relatively small, it can significantly influence the bending stiffness of a plate, as calculated by the nonlocal theory. When the thickness of the plate is relatively large, the modification factor tends to unity which means the bending stiffness will be equal to its classical limit $\mathbf{D} = \frac{h^3}{12}\mathbf{Q}$. According to these calculations, the thickness at which the difference between classical and nonlocal solutions gets more than 1% is $h = 16e_0a$.

In the calculation of the modifying factors λ and β , the initial calculation was based on a uniform deformation in a plate. However, it was shown that if the kernel can be decoupled in in-plane and out-of-plane directions, such modification factors can be used for a non-uniform deformation as well. In the latter case, the in-plane non-locality would have a contribution to the nonlocal stress resultants and stress couples. This contribution needs to be treated by existing nonlocal plate theories.

The results, as shown in Figures 6.6 and 6.7, suggest that the nonlocal solution with the bounded kernel reflects the size dependency of the elastic properties at a relatively smaller length scale. The difference between the two nonlocal solutions is relatively large, and is almost comparable to their differences with the classical elasticity. According to Eringen's nonlocal theory and several other publications [4, 11, 22], the solution with bounded kernel is considered to be the "correct" nonlocal

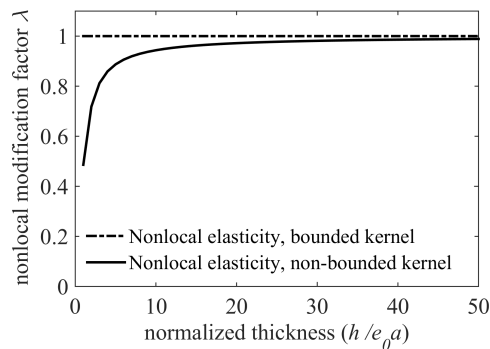


Figure 6.6: Nonlocal modification factor for extensional stiffness matrix as a function of the thickness of the plate normalized with internal length scale.

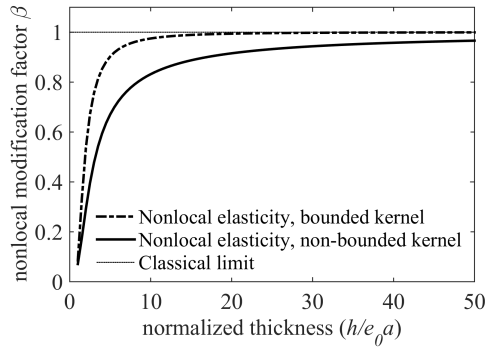


Figure 6.7: Nonlocal modification factor for bending stiffness matrix as a function of the thickness of the plate normalized with internal length scale.

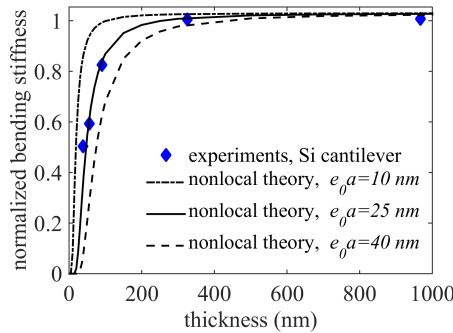


Figure 6.8: The normalized bending stiffness of a wide silicon cantilever in cylindrical bending based on pull-in measurements [28], and calculated with nonlocal theory with three different internal length scales.

solution.

Finally, we briefly discuss an example on how this theoretical approach can be applied in practice. For this purpose, a comparison is made to an experimental result provided by Sadeghian, *et al.* [28]. In that study, the size-dependence of the elastic behavior in Silicon nano-cantilevers has been experimentally investigated. The employed cantilevers in this study were 170 to 8 μm long, 20 to 8 μm wide and 1019 to 40 nm thick. Considering the large aspect ratio of the cantilevers they can be modeled as plates.

Figure 6.8 shows the experimentally obtained bending stiffness of the cantilevers when subjected to a non-uniform cylindrical bending. The bending stiffness in this graph is normalized with its classical amount $\frac{E t^3}{12(1-\nu^2)}$. The experimental results clearly show that the bending stiffness of the cantilevers is a function of their thickness.

For comparison the proposed nonlocal modification factors derived for three different length scales β are also shown in this figure. The theoretical results are calculated using a bounded kernel. The very similar trend to the experiments can be modeled using the modification factor proposed in this chapter and the best match is achieved

when $e_0 a = 25$ nm. We shall remind here that the internal length scale $e_0 a$ can be affected by the Silicon crystal properties as well as all the defects particularly on its surface. This excellent match between the model and the experimental results shows the potential for employing the proposed model in mechanical characterization of nano-structures. The observed scale effect can be captured with nonlocal elasticity theory effectively, and moreover, it is easy to implement.

6.5. CONCLUSIONS

In this chapter, using a nonlocal elasticity theory, we have presented a formulation to capture the effect of thickness on size-dependent behavior of plates. We have discussed some new aspects and challenges of employing the strong three dimensional nonlocal formulation for analysis of plates. The presented formulation has been employed for a practical problem and is shown to be capable to describe the size effect observed experimentally.

Generally, in employing nonlocal elasticity formulation for plate problems, the non-locality in the constitutive equations is only considered in tangential directions of the plate. This, in turn, results in predicting a size dependent mechanical behavior which does not reflect any dependence to the plate thickness. This is while experimental results indicate otherwise [28]. Moreover, if the nonlocal elasticity aims to capture the long-range interactions between the atoms of the material in a continuous framework, their impact should be reflected in all directions, including the transverse direction.

The main problem in capturing non-locality in transverse direction for plates lies in confining the nonlocal kernel at the two surfaces of the structure. In this study, to investigate the effects of including the transverse non-locality in analysis of plates, we have employed two types of nonlocal kernels with bounded and non-bounded boundaries. In particular, the problem of uniform deformations of a plate has been studied with both types of kernels. The results show that using the nonlocal formulation with a bounded kernel can reflect the physics of the problem better. In fact, using a bounded kernel (i) for a given uniform local strain field, a nonlocal formulation predicts a uniform nonlocal stress field, (ii) stress components near the surface do not exhibit the sharp reduction, which occurs in case of employing a non-bounded kernel.

It should be mentioned here that although according to Eringen's theory of nonlocal elasticity, the solution given by a bounded kernel (finite-scale kernel) is suggested to provide the "correct" solution, there is no suggestion for a physical interpretation of the chosen boundary conditions on such a kernel. Thus, there is a definite need for a thorough study to define the reasoning behind the adaptation of the kernel in boundary regions. The authors suggest that calculating the suitable boundary condition for the nonlocal kernel in nonlocal elasticity theories (and other higher order elasticity theories) should be practicable using a molecular dynamics simulation or another atomistic model. These boundary conditions should not be problem dependent and instead they should reflect the physical properties in the surface of the structure. Otherwise, the nonlocal continuum theories will not be viable as they have to be adapted to every single problem.

Moreover, in practice, defects are in the nature of all materials. In a structure with a defected surface, the surface properties such as inhomogeneous elasticity should also be involved in the formulation. Furthermore, the effect of the surface defects should be reflected in the nonlocal kernel either via the boundary conditions or the internal length scale.

As a result of this study, two nonlocal modification factors on extensional and bending stiffness matrices have been presented to account for the effect of thickness in the nonlocal formulations. These modification factors are valid for any shape of the plates. Provided that the nonlocal kernel is separable in transverse and tangential coordinates, they can be used for solutions based on conventional nonlocal plate theories. The observed scaling effect and a good match to experimental results motivate future research into clear interpretation of the internal length scale and the boundary conditions.

REFERENCES

- [1] B. Sajadi, H. Goosen, and F. van Keulen, *Capturing the effect of thickness on size-dependent behavior of plates with nonlocal theory*, [International Journal of Solids and Structures](#) (2017), 10.1016/j.ijsolstr.2017.03.010.
- [2] A. C. Eringen, *Nonlocal continuum field theories* (Springer, 2002).
- [3] E. Kröner, *Elasticity theory of materials with long range cohesive forces*, [International Journal of Solids and Structures](#) **3**, 731 (1967).
- [4] A. Angela Pisano and P. Fuschi, *Closed form solution for a nonlocal elastic bar in tension*, [International Journal of Solids and Structures](#) **40**, 13 (2003).
- [5] A. C. Eringen, *Edge dislocation in nonlocal elasticity*, [International Journal of Engineering Science](#) **15**, 177 (1977).
- [6] F. dell'Isola, U. Andreaus, L. Placidi, and D. Scerrato, *Intorno alle equazioni fondamentali del movimento di corpi qualsivogliono, considerati secondo la naturale loro forma e costituzione*, in *The complete works of Gabrio Piola: Volume I* (Springer, 2014) pp. 1–370.
- [7] F. Dell'Isola, A. Della Corte, and I. Giorgio, *Higher-gradient continua: The legacy of piola, mindlin, sedov and toupin and some future research perspectives*, [Mathematics and Mechanics of Solids](#) , 1081286515616034 (2016).
- [8] M. Di Paola, G. Failla, A. Pirrotta, A. Sofi, and M. Zingales, *The mechanically based non-local elasticity: an overview of main results and future challenges*, [Philosophical Transactions of the Royal Society A: Mathematical, Physical and Engineering Sciences](#) **371** (2013), 10.1098/rsta.2012.0433.
- [9] J. Engelbrecht and M. Braun, *Nonlinear waves in nonlocal media*, [Applied Mechanics Reviews](#) **51**, 475 (1998), 10.1115/1.3099016.
- [10] S. Silling and R. Lehoucq, *Peridynamic theory of solid mechanics*, [Advances in applied mechanics](#) **44**, 73 (2010).
- [11] R. Peerlings, M. Geers, R. De Borst, and W. Brekelmans, *A critical comparison of nonlocal and gradient-enhanced softening continua*, [International Journal of Solids and Structures](#) **38**, 7723 (2001).
- [12] O. Weckner, G. Brunk, M. A. Epton, S. A. Silling, and E. Askari, *Comparison between local elasticity and non-local peridynamics*, Sandia National Laboratory Report J **1109**, 2009 (2009).
- [13] A. C. Eringen, *Plane waves in nonlocal micropolar elasticity*, [International Journal of Engineering Science](#) **22**, 1113 (1984).
- [14] P. Lu, H. Lee, C. Lu, and P. Zhang, *Application of nonlocal beam models for carbon nanotubes*, [International Journal of Solids and Structures](#) **44**, 5289 (2007).

- [15] P. Lu, P. Zhang, H. Lee, C. Wang, and J. Reddy, *Non-local elastic plate theories*, *Proceedings of the Royal Society A: Mathematical, Physical and Engineering Science* **463**, 3225 (2007).
- [16] W. Duan, C. M. Wang, and Y. Zhang, *Calibration of nonlocal scaling effect parameter for free vibration of carbon nanotubes by molecular dynamics*, *Journal of Applied Physics* **101**, 024305 (2007).
- [17] R. Picu, *On the functional form of non-local elasticity kernels*, *Journal of the Mechanics and Physics of Solids* **50**, 1923 (2002).
- [18] A. C. Eringen, *On differential equations of nonlocal elasticity and solutions of screw dislocation and surface waves*, *Journal of Applied Physics* **54**, 4703 (1983).
- [19] D. C. Lam, F. Yang, A. Chong, J. Wang, and P. Tong, *Experiments and theory in strain gradient elasticity*, *Journal of the Mechanics and Physics of Solids* **51**, 1477 (2003).
- [20] S. Ghosh, V. Sundararaghavan, and A. M. Waas, *Construction of multi-dimensional isotropic kernels for nonlocal elasticity based on phonon dispersion data*, *International Journal of Solids and Structures* **51**, 392 (2014).
- [21] R. Maranganti and P. Sharma, *Length scales at which classical elasticity breaks down for various materials*, *Physical review letters* **98**, 195504 (2007).
- [22] R. Abdollahi and B. Boroomand, *Benchmarks in nonlocal elasticity defined by eringen's integral model*, *International Journal of Solids and Structures* **50**, 2758 (2013).
- [23] X. Ren and L. Truskinovsky, *Finite scale microstructures in nonlocal elasticity*, *Journal of elasticity and the physical science of solids* **59**, 319 (2000).
- [24] J. Peddieson, G. R. Buchanan, and R. P. McNitt, *Application of nonlocal continuum models to nanotechnology*, *International Journal of Engineering Science* **41**, 305 (2003).
- [25] J. Reddy, *Nonlocal nonlinear formulations for bending of classical and shear deformation theories of beams and plates*, *International Journal of Engineering Science* **48**, 1507 (2010).
- [26] Q. Wang and K. Liew, *Application of nonlocal continuum mechanics to static analysis of micro-and nano-structures*, *Physics Letters A* **363**, 236 (2007).
- [27] I. Stakgold and M. J. Holst, *Green's functions and boundary value problems*, Vol. 99 (John Wiley & Sons, 2011).
- [28] H. Sadeghian, C.-K. Yang, H. Goosen, P. J. F. Van Der Drift, A. Bossche, P. J. F. French, and F. Van Keulen, *Characterizing size-dependent effective elastic modulus of silicon nanocantilevers using electrostatic pull-in instability*, *Applied Physics Letters* **94**, 221903 (2009).

7

APPLICATION OF MICRO-PLATES FOR SURFACE STRESS MEASUREMENTS

In previous chapters the characteristics of a micro-plate as a transducer to convert the electrostatic energy to mechanical energy was studied. In this chapter, we aim to investigate the opposite practice of the micro-plates. As a matter of fact, in sensing applications, the micro-plates can serve as transducers to convert the mechanical energy to an electrical signal. Surface stress based measurement is a relatively new mechanism in biological and chemical sensing. The viability of this mechanism depends on the maximum sensitivity, accuracy and precision that can be achieved with these sensors. In this chapter, an analytical solution and a finite element model are employed to describe the electromechanical behavior of a surface stress based sensor with capacitive measurements. Using this approach, we can calculate the optimum design of the sensor to obtain the maximum capacitive sensitivity. Moreover, using the finite element simulation, we study the effect of this optimization on accuracy and precision of the system in surface stress sensing. This study shows that the ratio of sensing area to the whole micro-plate plays a key role in the functionality of such a sensor.

7.1. INTRODUCTION

The principle of bio-molecular recognition in nano-mechanical sensors is based on molecular adsorption on one side of a plate-like component [2, 3]. As a consequence, the surface stress of the component changes and this leads to deformation of the component. Next, the corresponding deflection of the system can be measured and used to estimate the surface stress and, thus, the amount of molecular adsorption.

Several types of nano-mechanical components, including doubly clamped beams, cantilevers, and membranes, are used for biological detection [2, 4, 5]. Cantilevers are the most commonly used structures in surface stress based measurements. They are highly compliant as compared to other types of structures and their micro-fabrication technology is well established and simpler than for membranes [3, 6]. However, when used in liquid environments, cantilever structures may restrain most types of readout techniques. For example, an electrolyte solution around the cantilever allows for Faradic currents which limit most electric readout techniques. In addition, due to the high compliance of cantilevers, even a small flow can affect the cantilever's deflection to a large extent [7, 8].

Clamped plates and membranes, on the other hand, can provide a separation between their detection and sensing surfaces. Thus, in liquid environments, they potentially benefit from a wider range of electric readout techniques [8, 9]. However, compared to cantilevers, a clamped plate is a relatively stiff structure. This structural stiffness results from the boundary conditions which restrict both the transverse displacement and its derivatives at the edges. Particularly, in case of a uniform surface stress loading, it does not show any deformation, and this leads to a poor sensitivity of the overall sensor [6, 10]. In order to narrow this drawback and to maximize the sensing signal, the structural parameters of the sensor should be optimized. The design freedom in such an optimization is mainly restricted to the dimensions of the plate, the shape and dimensions of the functionalized area.

Based on finite elements simulations, it has been shown that the output signal of surface stress based capacitive sensors can be improved by adjusting the geometrical parameters such as the gap between the electrodes and specially, the size of the sensing or functionalized area [11–13]. However, the finite element simulations are only valid for specific choices of materials and dimensions, and they do not provide any insight to the problem. In addition, they are generally time-consuming, expensive. On the other hand, an analytical solution—if available—can provide a closed form formulation for calculating the sensitivity of a sensor with any dimension or material. Therefore, analytical solutions are usually preferred for design purposes. In addition, an analytical solution provides more insight to the mechanics of the device, which is paramount for its further development. To the best of our knowledge, no analytical solution is available for calculating the deflection of a fully clamped plate/membrane arising from surface stress changes on a part of its surface.

Apart from the sensitivity, there are some other parameters which have to be considered when evaluating the suitability of a sensor, such as linearity, repeatability, accuracy and precision. Accuracy is the degree of closeness of a measured or calculated quantity to its reference (expected) value. Accuracy is closely related to precision also called reproducibility. In general, in biological detections, the poor surface coverage

of target molecules on the functionalized area (e.g. due to contamination of the surface or poor adhesion), might result in a low accuracy and precision [14–17].

It is commonly assumed that if the surface coverage is uniformly dispersed, the surface stress induced by the adsorption exhibits a non-linear dependence on the surface coverage, and it steeply increases when the coverage is near saturation [2, 18, 19]. However, at low concentration of target molecules, or when the target molecules or proteins are large, the distribution of the coverage might be randomly dispersed or just accumulated in one area [19, 20]. In which case, the surface coverage is not as uniform, and the theoretical model will not provide an accurate estimate of the concentration. In practice, low precision can be tackled by employing parallel probes in one measurement. However, still a high reliability of individual sensing components is favorable.

This chapter aims to find the optimal design of a capacitive surface stress sensor with a circular clamped plate/membrane as its sensing component. First, an analytical solution is presented to calculate the deformation of such a plate due to a change in the surface stress, while this change occurs only on a smaller concentric area of its surface. Using this study, we can find the optimum size of the functionalized area in order to create the maximum deflection.

Next, we present a design for a membrane-based capacitive sensor for surface stress measurements. Using the presented solution, the capacitive sensitivity of this sensor is obtained analytically. Then, to verify the competence of the approximated solution, the results will be compared to a detailed finite element solution. Eventually, we will discuss the optimized sensitivity of the membrane-shape sensors in comparison with cantilevers, and the effects of material and geometrical parameters on this sensitivity.

Moreover, using the finite element model, we study the effect of the shape and position of the agglomeration of target molecules on the ultimate response of these types of sensors. We show that by optimizing the size of the functionalized area, in addition to achieving a better sensitivity, the performance of the sensor with respect to precision can be improved.

7.2. ANALYTICAL FORMULATION

In micro-mechanical biological and chemical sensing, the bonding of measurand molecules to the functionalized surface of a plate leads to a change in the surface stress and as a result to bending of the plate. The surface stress variation for plate-like structures is usually estimated analytically by applying the famous “Stoney” equation. The latter provides a linear relationship between the tangential surface stress in the surface layer and the curvature of the plate [21]. Stoney’s equation, however, was initially derived for a system composed of a pre-stressed thin film attached to and fully-covering a relatively thick substrate with free boundary conditions.

There are many extensions and modifications of Stoney’s equation to relax some of its simplifying assumptions [22–24]. Yet, this equation has not been extended or modified for a fully-clamped circular plate, up until now. In this section, we shall derive a closed form approximate solution for calculating the deflection of a clamped circular plate due to a change in surface stress on a circular and concentric smaller

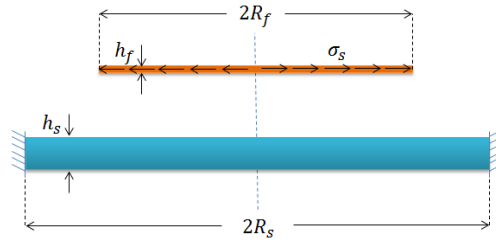


Figure 7.1: The thin film and the substrate with different radii, and an equivalent pretension in the thin film

functionalized area of its surface.

An isotropic and homogeneous clamped circular plate of radius R_s is considered (Figure 7.1). As a substitute for the functionalized surface layer, a thin film is assumed to be attached to the substrate. The shape of the film is circular and concentric with the substrate. The radius of this film is R_f and it is subjected to a pretension which is equivalent to the change in surface stress. The thickness of the thin film and the substrate are h_f and h_s , respectively, where $\frac{h_f}{h_s} \ll 1$. The Young's modulus and Poisson's ratio of the film and substrate are E_f , ν_f , E_s and ν_s , respectively. The problem is considered to be axisymmetric and Kirchhoff plate theory is employed. In all other parameters to be introduced, the subscripts s and f refer to the substrate and the thin film, respectively.

The chemical reaction between the functionalized surface and the measurand bio-molecules introduces a surface stress to the plate. This tangential surface stress change is modeled with an equivalent tangential stress resultant (σ^s) in the thin film. This stress resultant (σ^s) is assumed to be isotropic, i.e. similar in radial and angular directions, and uniform. In the analysis, we can either consider the tangential stress resultant in the film, or an equivalent isotropic and uniform in-plane strain ϵ_m . This equivalent strain can be calculated with Hooke's law giving

$$\epsilon_m = \sigma^s \frac{1 - \nu_f}{E_f h_f}. \quad (7.1)$$

If we attach the pre-stressed thin film to the clamped plate, the system will deform to relax the stress in the film. We analyze the equilibrium state of the film and the plate after the relaxation, together as one system.

Let u_f and u_s denote the radial displacements at the mid-plane of the thin film and substrate after relaxation of the system, and w the out-of-plane displacement in both. Since the film is relatively thin, the variation of its displacement and stress components in transverse direction is negligible. The continuity of displacements across the film/substrate interface requires:

$$u_f = u_s - \frac{h_s + h_f}{2} \frac{dw}{dr}. \quad (7.2)$$

Based on Kirchhoff plate theory, the non-vanishing stress resultant in the thin film and the substrate (N_r and N_θ in radial and tangential directions) can be calculated

as:

$$N_{rf} = \frac{E_f h_f}{1 - \nu_f^2} \left(\frac{du_f}{dr} + \nu_f \frac{u_f}{r} \right) + \sigma^s, \quad (7.3)$$

$$N_{\theta f} = \frac{E_f h_f}{1 - \nu_f^2} \left(\nu_f \frac{du_f}{dr} + \frac{u_f}{r} \right) + \sigma^s, \quad (7.4)$$

$$N_{rs} = \frac{E_s h_s}{1 - \nu_s^2} \left(\frac{du_s}{dr} + \nu_s \frac{u_s}{r} \right), \quad (7.5)$$

$$N_{\theta s} = \frac{E_s h_s}{1 - \nu_s^2} \left(\nu_s \frac{du_s}{dr} + \frac{u_s}{r} \right). \quad (7.6)$$

The tangential stress couples of the substrate in radial and tangential directions (M_r and M_θ) can be calculated by

$$M_{rs} = \frac{E_s h_s^3}{12(1 - \nu_s^2)} \left(\frac{d^2 w}{dr^2} + \frac{\nu_s}{r} \frac{dw}{dr} \right), \quad (7.7)$$

$$M_{\theta s} = \frac{E_s h_s^3}{12(1 - \nu_s^2)} \left(\nu_s \frac{d^2 w}{dr^2} + \frac{1}{r} \frac{dw}{dr} \right). \quad (7.8)$$

If we assume the plate and the film, together, as one laminated plate, the non-vanishing stress resultant in this structure can be calculated for $r < R_f$ and $R_f < r < R_s$, as

$$N_r = \begin{cases} N_{rf} + N_{rs} & r < R_f, \\ N_{rs} & R_f < r, \end{cases} \quad (7.9)$$

$$N_\theta = \begin{cases} N_{\theta f} + N_{\theta s} & r < R_f, \\ N_{\theta s} & R_f < r. \end{cases} \quad (7.10)$$

In calculating the tangential stress couples of the system, the equivalent moment due to presence of the thin film should be considered. Hence,

$$M_r = \begin{cases} N_{rf} \frac{h_s + h_f}{2} + M_{rs} & r < R_f \\ M_{rs} & R_f < r, \end{cases} \quad (7.11)$$

$$M_\theta = \begin{cases} N_{\theta f} \frac{h_s + h_f}{2} + M_{\theta s} & r < R_f \\ M_{\theta s} & R_f < r. \end{cases} \quad (7.12)$$

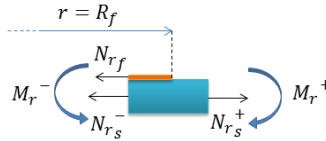


Figure 7.2: Cross section of a volume element at the edge of the film, including the thin film and the substrate, and the associated stress resultants and couples.

For the laminated plate, the equilibrium in radial and transverse directions can be expressed as [25]:

$$N_r - N_\theta + \frac{dN_r}{dr} r = 0, \quad (7.13)$$

$$M_r - M_\theta + \frac{dM_r}{dr} r = 0. \quad (7.14)$$

Using Equations (7.9)–(7.14), we obtain:

$$\begin{cases} N_{r_f} - N_{\theta_f} + \frac{dN_{r_f}}{dr} r + N_{r_s} - N_{\theta_s} + \frac{dN_{r_s}}{dr} r = 0 & r < R_f, \\ N_{r_s} - N_{\theta_s} + \frac{dN_{r_s}}{dr} r = 0 & R_f < r, \end{cases} \quad (7.15)$$

and

$$\begin{cases} \frac{h_s + h_f}{2} (N_{r_f} - N_{\theta_f} + \frac{dN_{r_f}}{dr} r) + M_{r_s} - M_{\theta_s} + \frac{dM_{r_s}}{dr} r = 0 & r < R_f, \\ M_{r_s} - M_{\theta_s} + \frac{dM_{r_s}}{dr} r = 0 & R_f < r. \end{cases} \quad (7.16)$$

Due to the presence of a discontinuity at $r = R_f$, the equilibrium of forces and moments for a volume element on the edge of the film should be considered separately:

$$N_{r_f}^- + N_{r_s}^- = N_{r_s}^+, \quad (7.17)$$

and,

$$\frac{1}{2} (h_s + h_f) N_{r_f}^- + M_{r_s}^- = M_{r_s}^+. \quad (7.18)$$

The superscripts $-$ and $+$ denote the limits of the functions in R_f from $r < R_f$ and $r > R_f$, respectively (see Figure 7.2). It should be noticed that here, the thin film stress resultant N_{r_f} includes the driving load σ^s .

Next, following Equations (7.2)–(7.16), the general solutions for the displacement components u_s and w can be calculated. Considering that the displacement should be finite at $r = 0$, the general solution of the equilibrium equations is obtained as:

$$w = \begin{cases} C_1 r^2 + C_2 & r < R_f, \\ C_3 r^2 + C_4 \ln r + C_5 & R_f < r, \end{cases} \quad (7.19)$$

$$u_s = \begin{cases} C_6 r & r < R_f, \\ C_7 r + C_8 / r & R_f < r. \end{cases} \quad (7.20)$$

The radial displacement in the thin film (u_f) follows from Equation (7.2). The parameters C_i ($i=1-8$) are the unknown degrees of freedom to be determined by satisfying continuity and boundary conditions, and the equilibrium at $r = R_f$ as expressed by (7.17) and (7.18). Continuity at the edge of the thin film requires:

$$u_s^+ = u_s^-, \quad (7.21)$$

$$w^+ = w^-, \quad (7.22)$$

$$\frac{dw^+}{dr} = \frac{dw^-}{dr}. \quad (7.23)$$

The clamping boundary condition implies:

$$u_s|_{R_s} = 0, \quad (7.24)$$

$$w|_{R_s} = 0, \quad (7.25)$$

$$\frac{dw}{dr}|_{R_s} = 0. \quad (7.26)$$

Hence, the unknown constants (C_i) can be calculated. Because of their complexity, the resulting expressions are not shown here. If we assume $\frac{h_f}{h_s} \ll 1$, and if the stiffness of the two materials is of the same order of magnitude (thus, higher-order terms of $\frac{E_f h_f}{E_s h_s}$ can be neglected with respect to 1), the solution for the displacement field can be simplified to:

$$w = \begin{cases} 3 \frac{\sigma^s}{h_s^2} \frac{1-\nu_s^2}{E_s} [R_f^2 \ln \frac{R_f}{R_s} + (1 - \frac{R_f^2}{R_s^2}) \frac{r^2}{2}] & r < R_f, \\ 3 \frac{\sigma^s}{h_s^2} \frac{1-\nu_s^2}{E_s} [R_f^2 \ln \frac{r}{R_s} + \frac{R_f^2}{2} (1 - \frac{r^2}{R_s^2})] & R_f < r, \end{cases} \quad (7.27)$$

$$u_s = \begin{cases} -\frac{1}{2} \frac{\sigma^s}{h_s} \frac{1-\nu_s^2}{E_s} (1 - \frac{R_f^2}{R_s^2}) r & r < R_f, \\ -\frac{1}{2} \frac{\sigma^s}{h_s} \frac{1-\nu_s^2}{E_s} (\frac{R_f^2}{r^2} - \frac{R_f^2}{R_s^2}) r & R_f < r. \end{cases} \quad (7.28)$$

The maximum deflection of the system is at $r = 0$ and is equal to

$$\Delta w = 3 \frac{\sigma^s}{h_s^2} \frac{1 - \nu_s^2}{E_s} R_f^2 \ln \frac{R_f}{R_s}. \quad (7.29)$$

Equation (7.29) can be looked upon as an extension of Stoney's formula for a film and substrate with different radii, with clamped boundary condition. Obviously if $R_f \rightarrow 0$, no film is left on the substrate and the deflection equates to zero. Also, if $R_f = R_s$, the deflection of the plate would vanish completely. This suggests the possibility of finding the optimum radius for the functionalized area which leads to the maximum deflection of the substrate. This, in turn, may provide the maximum sensitivity of the sensors (e.g., based on using optical readout techniques). Clearly, the maximum deflection is achieved when $\frac{\partial w|_{r=0}}{\partial R_f} = 0$. By solving this maximization problem, one can show that the optimum ratio of $\frac{R_f}{R_s}$ is always $\frac{R_f}{R_s} = 0.606$, and the corresponding maximum deflection of the membrane (i.e. its absolute amount) would be

$$\Delta w_{max} = \alpha \frac{\sigma^s}{h_s^2} \frac{1 - \nu_s^2}{E_s} R_s^2, \quad (7.30)$$

where $\alpha = 0.552$ (when $\frac{E_f}{E_s} \frac{h_f}{h_s} \ll 1$). This result is comparable to Stoney's solution for deflection of a cantilever due to a change in its tangential surface stress, where the thickness of the cantilever is the same as the membrane and its length is equal to the membrane radius:

$$w_{st} = 3 \frac{\sigma^s}{h_s^2} \frac{1 - \nu_s}{E_s} R_s^2. \quad (7.31)$$

Equations 7.31 and 7.30 imply the maximum deflection of a membrane, in optimized configuration, would be $0.184(1 + \nu_s)$ times that of an equivalent cantilever. The comparison between the sensitivity of cantilevers and membranes will be discussed in more detail in the Section "Results and discussion".

7.3. SENSITIVITY OF THE CAPACITIVE MEMBRANE SENSOR

In this section, the sensitivity of a *capacitive* sensor for surface stress based measurements is studied. A simplified model of this sensor with a micro-membrane as its sensing component is considered. A part of its surface is coated with a thin metal layer which, in fact, plays two roles. First, its surface is functionalized with probe molecules to adsorb the target molecules and second, it acts as an electrode for capacitive measurements. The whole structure is suspended over a conductive pad which is the other electrode for capacitance measurements. This conceptual design is graphically shown in Figure 7.3. The initial capacitance between two straight and parallel electrodes, can be calculated by

$$C_0 = \epsilon_r \epsilon_0 \frac{A_e}{d}, \quad (7.32)$$

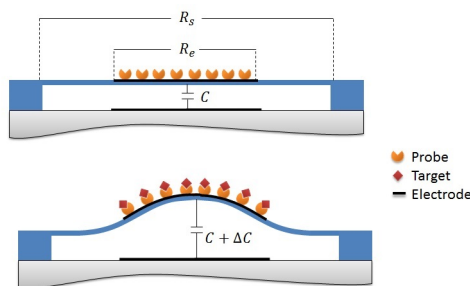


Figure 7.3: The schematic of the capacitive sensor for surface stress measurement, before (top) and after (bottom) the reaction between the probe and target molecules

where ϵ_0 is the vacuum permittivity, ϵ_r is the relative permittivity of the material between the plates, A_e is the electrode surface area, and d is the distance between the electrodes. The adsorption of target molecules on the metal layer will create a change in its surface stress which causes the membrane to deflect. After deflection, the capacitance of the system can be calculated by

$$C = \epsilon_r \epsilon_0 \int \frac{dA_e}{d + w}, \quad (7.33)$$

where w is the transverse deflection of the thin film (flexible electrode). The *sensitivity* of the sensor is defined as the relative capacity change to the input parameter, i.e., change of surface stress in the functionalized area. Using (7.32) and (7.33), the absolute change in capacitance can be calculated by

$$\Delta C = \epsilon_r \epsilon_0 \pi \left(\frac{R_e^2}{d} - \int_0^{R_e} \frac{2r dr}{d + w} \right), \quad (7.34)$$

which can be approximated using the expression for w in Equation (7.27), and the electrode radius (R_e) can be replaced by the radius of the thin film subjected to the change in surface stress (R_f). If the applied surface stress change (σ^s) is small, the response of the sensor can be linearized and therefore, the sensitivity of the sensor will be proportional to $\Delta C / \sigma^s$.

In order to maximize the sensitivity, the dimensions of the sensor shall be optimized. Clearly, a higher sensitivity can be achieved by decreasing the initial distance between the electrodes (d). However, the electrode radius (R_e) has an optimum size which can be calculated analytically by equating the first derivative of ΔC with respect to R_e (or R_f) to zero:

$$\frac{\partial(\Delta C)}{\partial R_e} = 0. \quad (7.35)$$

It should be mentioned that R_e which optimizes the maximum displacement is different from the one which maximizes ΔC . The results of this analysis will be discussed in Section “Results and discussion”.

Table 7.1: Model parameters

	Membrane	Electrode	Gap
Material	Silicon	Gold	Air
Elasticity Modulus	169 GPa	80 GPa	
Poisson ratio	0.2	0.3	
Radius	125 μm	R_e	
Thickness	0.5 μm	0.025 μm	2 μm
Relative Permittivity	11.68	1	1.006

7.4. FINITE ELEMENT MODEL

In order to evaluate the accuracy of the presented analytical solution, the simple sensor described in the last section is modeled with finite element software (COMSOL). The membrane is considered to be Silicon (undoped) which is a very common choice for MEMS devices. The electrode is chosen to be gold which is one of the most used materials for immobilizing bio-receptors on nanomechanical systems [2, 10, 11, 26]. The gap between the membrane and the bottom electrode is assumed to be filled with low pressure air. The mechanical properties of the chosen materials and other specifications of the model are given in Table 7.1.

The finite element model is 3D, and the mechanics and electrostatics equations of the system are solved fully coupled. The Silicon membrane and the thin surface layer are discretized with tetrahedral solid elements and triangular shell elements, respectively. The air gap is also discretized with tetrahedral elements to calculate the electrostatic field.

The surface layer of the electrode subjected to the surface stress is modeled with a very thin membrane, and the surface stress is modeled with a an equivalent pre-tension in this membrane. A pretension of 10 $m\text{N}/\text{m}$, which is a typical surface stress caused in biological reactions, is applied to the surface layer. Then, the mechanical and electrical response of the system are calculated. This calculation was performed for different electrode radii. The results of the FEM calculations and the proposed analytical solution will be compared in Section 7.6.

7.5. PRECISION OF THE SENSOR

In addition to sensitivity, accuracy and precision are two other sensor parameters which have to be considered in its design. *Precision* refers to the closeness of results of the measurements, for a similar input, to each other. *Accuracy* is the degree to which the average result of the measurement, conforms to the reference (expected) value. These two terms are graphically explained in Figure 7.4.

In surface stress based measurements, in order to function as a sensor, the concentration of the target molecules must be related to the surface stress, which in turn results in different deflections. As mentioned in the Introduction, a low density of the target molecules in the environment results in a partial coverage of the functionalized surface. Hence, only a part of the functionalized area will be subjected to the

surface stress change. Let us denote the ratio between this area to the whole functionalized area as *coverage ratio*.

Here, we assume that the coverage ratio increases monotonically with the density of molecules in environment [18, 20]. So, the coverage ratio is equal to 1, if the concentration of target molecules is high enough and the surface is saturated. Otherwise, the coverage ratio is lower than 1.

When the coverage ratio is less than one, it could imply a patch wise covering due to the agglomeration of target molecules in one area. The shape and the position of this agglomeration can influence the ultimate response of the sensor. Therefore, the output signal is not only a function of the coverage ratio, but also its shape, and this accordingly reduces the precision.

In Section 7.2 we showed that if the coverage is uniform over the functionalized area, a full size electrode ($R_e = R_s$) will result in very poor sensitivity. However, when a poor coverage is obtained, the size of electrode might seem irrelevant. In this section, we briefly study the effect of the radius of the functionalized area (thin electrode) on the performance of the sensor in case of a partial coverage. For this purpose, two models with different radii of the gold layer, one with maximum sensitivity and one covering the whole membrane, are considered. The finite element model employed is similar to that of the previous section.

The shape of the surface layer (modeled with a thin membrane) mimics the shape of the agglomeration of the molecules. In the finite element model this shape is controlled with a parametrized function as

$$\begin{aligned} x &= X_0 R_e + R_e (\sum_{i=0}^n A_i \cos(i s)) \cos(s), \\ y &= R_e (\sum_{i=0}^n A_i \cos(i s)) \sin(s), \end{aligned} \quad (7.36)$$

where x and y are the Cartesian coordinates and s is a curve parameter from 0 to 2π . As a matter of fact, Equation 7.36 resembles a Fourier Cosine expansion of the actual shape of the agglomeration of the molecules. The advantage of the Fourier representation is the level-of-detail interpretation which is provided by the parameter i . The low values of this parameter represent the coarse structure of a shape, while higher values add the details. In Equation 7.36, the parameter X_0 is introduced to move the created area out of the center. To study the effect of the shape of the adsorption area on the output, this parameter and the parameters A_i (assuming $i=1-7$) are varied between 0 to 1 randomly. In addition, if the shape intersects with the perimeter of the

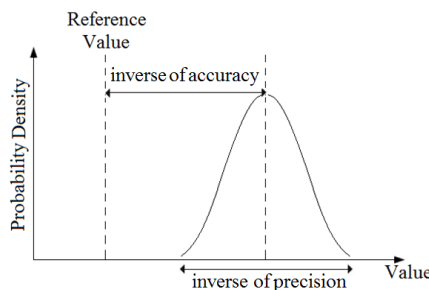


Figure 7.4: A graphic definition of accuracy and precision of a sensor.

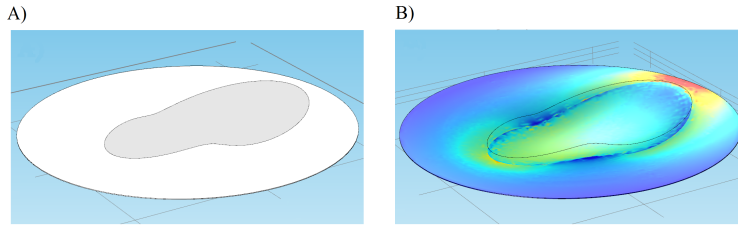


Figure 7.5: A part of the Comsol model, including the silicon membrane, the flexible electrode covering the whole membrane, and the thin layer with a random shape mimicking an agglomeration of molecules, A) before deformation, and B) after deformation due to a positive surface stress change.

functionalized area ($\sqrt{x^2 + y^2} > R_f$), only the inner part is subjected to the surface stress change. Any curve intersecting itself is skipped in the simulation, automatically.

Next, similar to the previous section, a pretension of 10 mN/m is applied to the surface layer, and deflection and capacitance of the system are calculated. Figure 7.5, for example, shows one configuration of this model before and after deformation. Due to different shapes of the adsorption area, a range of capacitance change is obtained for one coverage ratio. In practice, it is desired to restrict the range of the response in order to achieve a better precision in the sensor. Therefore, using the COMSOL model, the effect of the size of the functionalized area on the range of the capacitance changes is studied.

As a result of the FEM simulations, two factors of *eccentricity* and *circularity* were found to be appropriate and influential factors, for discussing the shape of the agglomeration of molecules. Circularity (f_c) is commonly used in image analysis and allows us to see how far a shape is from a circle. This shape factor is defined as

$$f_c = \frac{4\pi A}{P^2}, \quad (7.37)$$

where A is area and P is the perimeter of the related shape. Clearly, this factor is one for a circle and less than one for any other shape. Eccentricity (f_e) is defined as the ratio of the distance between the center of the adsorption area and the center of the plate, to the radius of the functionalized area. The results of this study are presented and discussed in Section 7.6.

7.6. RESULTS AND DISCUSSION

To discuss the effect of the size of the functionalized area on the sensitivity of a membrane sensor, we consider the model parameters given in Table 7.1 as a test case. Considering that Silicon is a relatively stiff material (see Table 7.1), the simplifying assumption $\frac{E_f}{E_s} \frac{h_f}{h_s} \ll 1$ holds and consequently, the solution for the displacement field is very close to the analytical solution presented by (7.27) and (7.28).

Figure 7.6 shows the deflection for the center of the plate as a function of the radius of the functionalized area (electrode). The graphs in this figure are obtained using the approximate analytical solution and the finite element model. It shows that

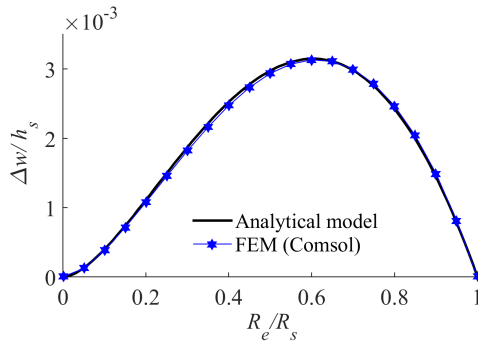


Figure 7.6: Deflection of a silicon membrane due to 10 mN/m change in surface stress, as a function of the normalized radius of the functionalized area.

the results of the two solutions are in close agreement which confirms the accuracy of the presented approximate solution.

It should be noticed that this problem is solved for a small surface stress of 10 mN/m, which does not cause a large deflection. Therefore, the results of the non-linear finite element model lead to a *slightly* lower deflection compared to the linear approximate solution. Figure 7.6 clearly shows that the maximum deflection of the membrane occurs when the radius of the electrode is 0.6 of that of the membrane. This optimized radius hardly depends on the choice of parameters, as long as $\frac{E_f}{E_s} \frac{h_f}{h_s} \ll 1$.

Figure 7.7 shows the change in the capacitance of the sensor as a function of the radius of the functionalized area (electrode). It should be mentioned that in our finite element model, the permittivity of the Silicon membrane and the air gap, and the fringing electric field around the periphery of the electrodes are all included. These factors (particularly the permittivity of the Silicon membrane) cause an absolute difference in capacitance from those predicted analytically. However, the relative ca-

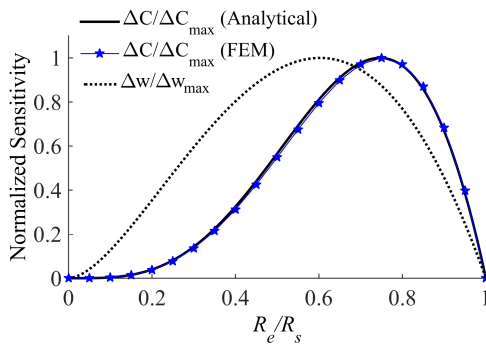


Figure 7.7: The normalized capacitance change of the system and maximum deflection of the curvature due to a change in surface stress, as a function of the normalized radius of the functionalized area.

capacitance change is similar for both the FEM and analytical models.

As can be observed from Figure 7.7, the sensitivity is maximum for an optimum radius of the functionalized area, $R_e/R_s = 0.76$. This optimum radius depends on the choice of the parameters of the sensor, i.e., materials and dimensions of the sensor. In order to compare the effect of the electrode radius on the capacitance and deflection of the system, the normalized deflection of the membrane is also shown in Figure 7.7. The results clearly show that the optimum radius to maximize the capacitive sensitivity is different from the one which maximizes the deflection.

This analysis was also performed for other choices of materials, while preserving other parameters in Table 7.1. The normalized deflection and the change in capacitance are shown in Figure 7.8 as a function of the radius of functionalized area and the Young's modulus of the membrane. It should be mentioned that for relatively compliant materials (i.e. smaller E_s), the simplifying assumption $\frac{E_f}{E_s} \frac{h_f}{h_s} \ll 1$ does not hold and hence, the graphs in Figure 7.8 are obtained by the exact solution of (7.19)-(7.26).

Clearly, the sensitivity of a mechanical sensor increases if a more compliant material is employed for the sensing component. This could also be observed from Equa-

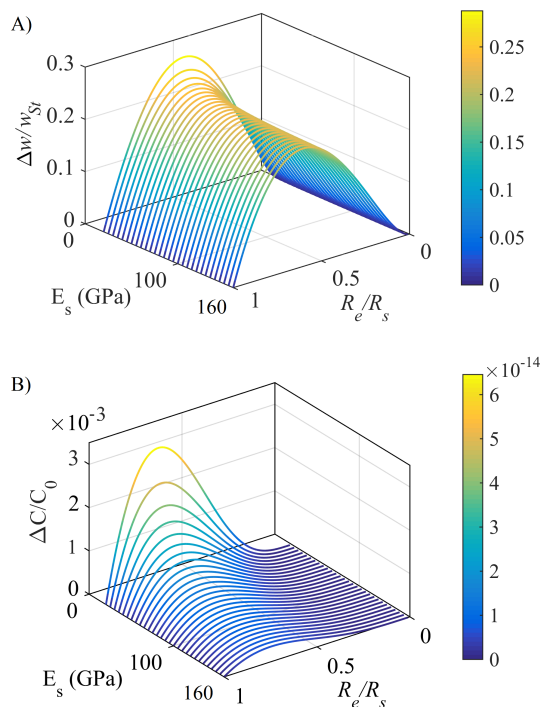


Figure 7.8: A) The maximum deflection of a membranes normalized by the deflection of an equivalent cantilever and B) the normalized change of the capacitance of the system due a change in surface stress, vs. Young's modulus of the membrane and the relative radius of functionalized area. The change in capacitance is normalized by (C_0) the capacitance of the system if $R_e = R_s$.

tion (7.30). In the current case, however, the optimized size of the functionalized area also depends to E_s , and hence, so does the parameter α in (7.30). In order to observe this effect, the maximum deflection of the membrane, $\Delta w = w|_{r=0}$, is normalized by the deflection of an equivalent cantilever, as given in (7.31).

According to Figure 7.8-A, by optimizing the radius of the functionalized area, the deflection of a clamped membrane can be optimized to a minimum of 22 percent of an equivalent cantilever. For stiff materials, where $E_s > 50$ GPa (e.g. Si, SiO₂, SiN), the optimum radius to maximize capacity is $R_e/R_s \approx 0.76$. However, this optimum radius and the maximum achievable deflection significantly differ for more compliant materials (e.g., polymers). For instance, for a Young's modulus of $E_s = 20$ GPa, the optimum radius changes to $R_e/R_s = 0.54$ and the deflection of the clamped membrane can be optimized to 29 percent of an equivalent cantilever.

Figure 7.8-B shows the change in capacitance of the system as a function of the Young's modulus of the membrane and the radius of the functionalized area. It shows that the maximum capacitive sensitivity, and the associated optimum radius, strongly depend on the material of the membrane. The overall capacitive sensitivity of the sensor is increased by a factor 10 when the compliance of the membrane is decreased by only a factor 8. In fact, the results shown in Figure 7.8 imply that this optimization has a better result for materials with lower stiffness.

It should be mentioned here that if the membrane is made of a conductive material (like doped Silicon), the whole membrane serves as an electrode (i.e. $R_e = R_s$). Then, the gold layer will only provide the functionalized surface (i.e. $R_f \neq R_e$). In this case, the optimum radius of the functionalized area (R_f) to create the maximum capacity change will be different and can be calculated based on the solution method proposed in this chapter. For such a case using the test parameters at hand, the radius of $R_f/R_s = 0.71$ will maximize the capacitive sensitivity.

It is noteworthy that the other design parameter which has an influence on sensitivity is the slenderness of the membrane ($S = \frac{R_s}{h_s}$). As Equation (7.30) shows, the deflection of the membrane increases monotonically with the aspect ratio of the membrane. This means that by increasing the slenderness, the sensitivity of the sensor will increase. However, this parameter has no influence on the optimum radius of the electrode for maximizing the sensitivity of the system.

This analysis was performed based on a full coverage of target molecules on the functionalized area and a uniform surface stress change. Next, we discuss how the optimization of the radius of the functionalized area can affect the precision for bi-

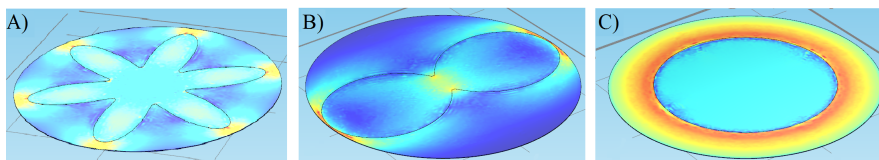


Figure 7.9: Three different shape of the surface layer mimicking the agglomeration of molecules on the functionalized area, with a same coverage ratio of 0.45, and different circularity A) $f_c = 0.23$ and $\Delta C/C_{max} = 2.126 \times 10^{-4}$, B) $f_c = 0.52$ and $\Delta C/C_{max} = 1.032 \times 10^{-4}$, c) $f_c = 1$ and $\Delta C/C_{max} = 3.021 \times 10^{-4}$

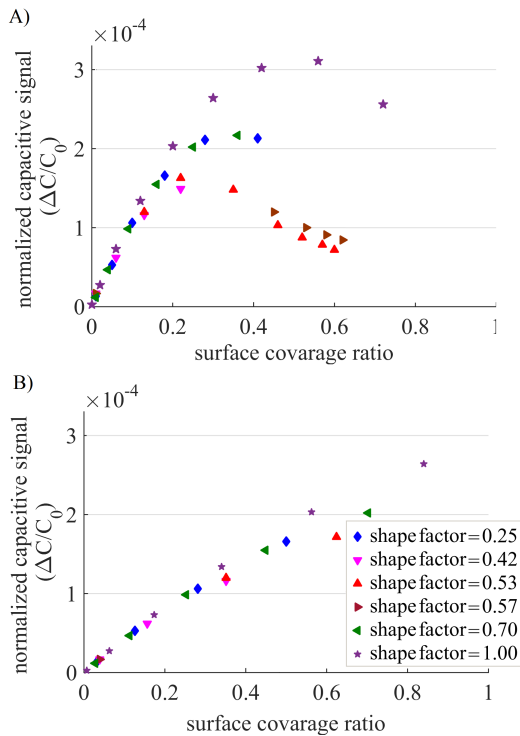


Figure 7.10: The capacity change for A) $R_e/R_s = 1$ and B) $R_e/R_s = 0.6$, as a function of coverage ratio for different shape-factors of agglomeration of molecules.

7

ological and chemical detections, if the coverage is not full and uniform. Figure 7.9 shows three differently shaped adsorption areas, though with similar coverage ratios. Although these examples have hyperbolic shapes, they clearly show how a similar coverage ratio may result in completely different capacity changes.

Figure 7.10 shows the normalized capacity change as a function of the coverage ratio, while considering a random circularity (and an eccentricity of zero) of the area subjected to surface stress. The graphs are obtained for two cases, namely, $R_e = R_s$ (Figure 7.10-A) and $R_e = 0.6R_s$ (Figure 7.10-B). As can be observed, the maximum capacity change occurs when the shape of the adsorption is circular, i.e. the shape factor is equal to one.

When $R_e = R_s$ (Figure 7.10-A), the output of the sensor has a strong dependence on the shape of the agglomeration of molecules and this leads to a significant reduction in the precision of the sensor. First of all, there is no one-to-one relationship between the capacity change and the coverage ratio. Second, a similar coverage ratio may result in a relatively large range of capacity change. Moreover, the maximum capacity change occurs when the coverage ratio is around 0.58, though, the results indicate that the precision of the sensor is the worst around this coverage ratio.

When $R_e = 0.76R_s$ (Figure 7.10-B), on the other hand, the response of the system has a near linear relationship with the coverage ratio and the maximum capacity

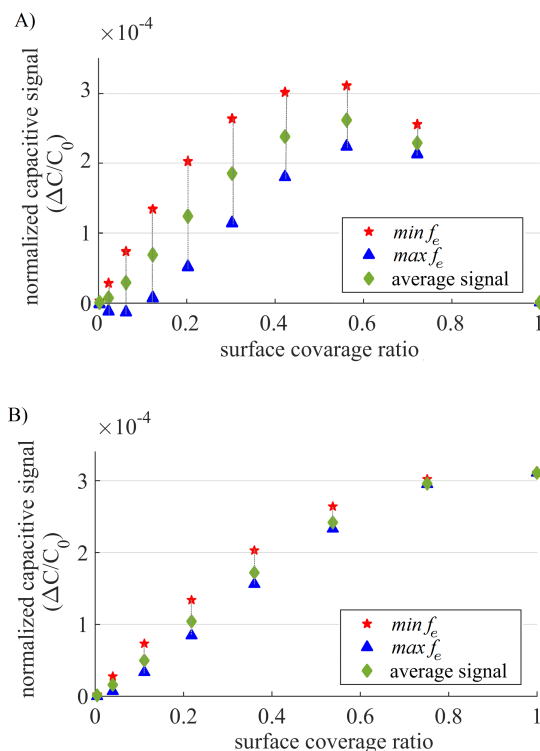


Figure 7.11: The range of the output signal for A) $R_e/R_s = 1$ and B) $R_e/R_s = 0.76$ due to eccentricity of agglomeration of molecules.

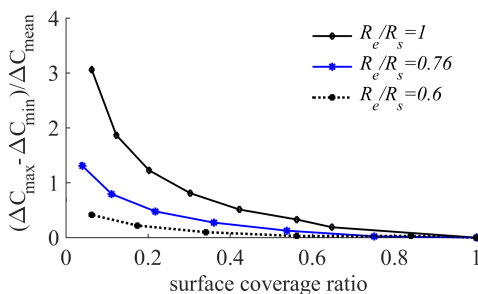


Figure 7.12: The relative range of capacitance changes, due to eccentricity of agglomeration of molecules for different radii of the functionalized area.

change occurs with the full coverage. Reducing the size of the functionalized area can strongly confine the dependency of the capacity change to the shape of the adsorption area.

Figure 7.11 shows the range of the capacity change caused by different eccentric-

ity of the aggregation of molecules. The results of the FEM simulations show that for any coverage ratio, the maximum signal occurs if the aggregation of molecules is concentric at the functionalized area (i.e. f_e is minimum or equates to zero), and this signal decreases monotonically with the eccentricity. Therefore, for a similar coverage ratio, a large range of output signal might be observed. This is only due to different eccentricities which results in a very poor accuracy and precision for the sensor (see Figure 7.11-A). Clearly, the maximum eccentricity can be confined by reducing the size of the functionalized area (see Figure 7.11-B). In fact, by reducing the size of functionalized area, the response of the sensor has a near linear and a one-to-one relation with the coverage ratio of the target molecules.

In order to clarify the effect of reducing the size of the functionalized area on the accuracy of the system, the relative range of capacitance change due to the eccentricity of agglomeration of molecules is shown in Figure 7.12. It can be clearly observed that for any radius of the functionalized area, the poorest accuracy can be expected for the lowest coverage ratio. For instance, for $R_e/R_s = 1$, when a small cluster of molecules is adsorbed to the functionalized area, the range of the response of the sensor is higher than three times its average response.

The range of the capacitive signal for any coverage ratio can be reduced to a large extent, when the size of the functionalized area is decreased, which, in turn, increases the accuracy and precision of the sensor. Evidently, this increase in the accuracy and precision is limited by the inherent *signal to noise ratio* of the sensor, in practice. Overall, the results of this study shows that by decreasing the size of the functionalized area, not only the sensitivity of the surface stress sensors can be optimized, but also, the linearity, accuracy and precision of the system can be improved.

7

7.7. CONCLUSION

This chapter presented an analytical solution for the displacement of a membrane subjected to a surface stress changes in a part of its surface. Using this solution, we derived the sensitivity of a membrane-shape capacitive sensor for surface stress measurement. The competence of the proposed solution was verified by a comparison with a detailed finite element model. The proposed analytical solution presents a very accurate, fast and robust tool that can be used for design purposes.

The results of this study imply that the relative size of the functionalized area, has a significant influence on the overall performance of such a sensor. This solution shows that we can increase the deflection of the circular membrane-shape sensor up to at least 22 percent of that of an equivalent cantilever shaped sensor. It is important to emphasize that using membrane sensors, in comparison to cantilevers, allow us to benefit from capacitive read-out techniques in liquid environments. Although the absolute amount of capacity change is small, due to the high resolution of capacitive measurements, the ultimate (optimized) sensitivity may be comparable to—or even better than—cantilevers.

Furthermore, it was noticed that using the proposed optimized size of the functionalized area, the linearity, accuracy and precision of the system can be significantly improved. Consequently, the overall reliability of the system can be increased.

REFERENCES

- [1] B. Sajadi, H. Goosen, and F. van Keulen, *Optimization of capacitive membrane sensors for surface-stress based measurements*, *IEEE Sensors Journal* (2017), [10.1109/JSEN.2017.2687045](#).
- [2] J. Tamayo, P. M. Kosaka, J. J. Ruz, A. San Paulo, and M. Calleja, *Biosensors based on nanomechanical systems*, *Chemical Society Reviews* **42**, 1287 (2013).
- [3] F. T. Goericke and W. P. King, *Modeling piezoresistive microcantilever sensor response to surface stress for biochemical sensors*, *IEEE Sensors Journal* **8**, 1404 (2008).
- [4] J. Arlett, E. Myers, and M. Roukes, *Comparative advantages of mechanical biosensors*, *Nature nanotechnology* **6**, 203 (2011).
- [5] M. Godin, V. Tabard-Cossa, Y. Miyahara, T. Monga, P. Williams, L. Beaulieu, R. B. Lennox, and P. Grutter, *Cantilever-based sensing: the origin of surface stress and optimization strategies*, *Nanotechnology* **21**, 075501 (2010).
- [6] E. T. Carlen, M. S. Weinberg, C. E. Dube, A. M. Zapata, and J. T. Borenstein, *Micromachined silicon plates for sensing molecular interactions*, *Applied physics letters* **89**, 173123 (2006).
- [7] R. Raiteri, H.-J. Butt, and M. Grattarola, *Changes in surface stress at the liquid/solid interface measured with a microcantilever*, *Electrochimica Acta* **46**, 157 (2000).
- [8] J.-k. Choi, M. Cha, and J. Lee, *Thin membrane transducer detecting dna hybridization on chip*, in *Sensors, 2009 IEEE* (IEEE) pp. 815–818.
- [9] A. Zapata, E. Carlen, E. Kim, J. Hsiao, D. Traviglia, and M. Weinberg, *Biomolecular sensing using surface micromachined silicon plates*, in *Solid-State Sensors, Actuators and Microsystems Conference, 2007. TRANSDUCERS 2007. International* (IEEE) pp. 831–834.
- [10] M. Cha, J. Shin, J.-H. Kim, I. Kim, J. Choi, N. Lee, B.-G. Kim, and J. Lee, *Biomolecular detection with a thin membrane transducer*, *Lab chip* **8**, 932 (2008).
- [11] S. Satyanarayana, D. T. McCormick, and A. Majumdar, *Parylene micro membrane capacitive sensor array for chemical and biological sensing*, *Sensors and Actuators B: Chemical* **115**, 494 (2006).
- [12] W. Zhang, H. Feng, S. Sang, Q. Shi, J. Hu, P. Li, and G. Li, *Structural optimization of the micro-membrane for a novel surface stress-based capacitive biosensor*, *Microelectronic Engineering* **106**, 9 (2013).
- [13] V. Tsouti and S. Chatzandroulis, *Sensitivity study of surface stress biosensors based on ultrathin si membranes*, *Microelectronic Engineering* **90**, 29 (2012).
- [14] V. Tsouti, C. Boutopoulos, M. Ioannou, D. Goustouridis, D. Kafetzopoulos, I. Zergioti, D. Tsoukalas, P. Normand, and S. Chatzandroulis, *Evaluation of capacitive surface stress biosensors*, *Microelectronic Engineering* **90**, 37 (2012).

- [15] A. Moulin, S. O'shea, and M. Welland, *Microcantilever-based biosensors*, [Ultra-microscopy](#) **82**, 23 (2000).
- [16] V. Tabard-Cossa, M. Godin, I. J. Burgess, T. Monga, R. B. Lennox, and P. Grütter, *Microcantilever-based sensors: effect of morphology, adhesion, and cleanliness of the sensing surface on surface stress*, [Analytical chemistry](#) **79**, 8136 (2007).
- [17] V. Tsouti and S. Chatzandroulis, *Non-ideal biological layer deposition effects on membrane surface stress based biosensor performance*, [Microelectronic Engineering](#) **144**, 23 (2015).
- [18] M. L. Sushko, J. H. Harding, A. L. Shluger, R. A. McKendry, and M. Watari, *Physics of nanomechanical biosensing on cantilever arrays*, [Advanced Materials](#) **20**, 3848 (2008).
- [19] Z. Gao, C.-S. Kim, and D. B. Henthorn, *Sensor application of poly (ethylene glycol) diacrylate hydrogels chemically-anchored on polymer surface*, [IEEE Sensors Journal](#) **13**, 1690 (2013).
- [20] J. Tian, Y. Bai, X. Tang, S. Sang, and F. Wang, *A capacitive surface stress biosensor for csfv detection*, [Microelectronic Engineering](#) (2016), [10.1016/j.mee.2016.02.037](#).
- [21] G. G. Stoney, *The tension of metallic films deposited by electrolysis*, [Proceedings of the Royal Society of London. Series A, Containing Papers of a Mathematical and Physical Character](#) **82**, 172 (1909).
- [22] X. Feng, Y. Huang, and A. Rosakis, *On the stoney formula for a thin film/substrate system with nonuniform substrate thickness*, [Urbana](#) **51**, 61801 (2007).
- [23] Y. Huang and A. Rosakis, *Extension of stoney's formula to non-uniform temperature distributions in thin film/substrate systems. the case of radial symmetry*, [Journal of the Mechanics and Physics of Solids](#) **53**, 2483 (2005).
- [24] L. Freund, *Substrate curvature due to thin film mismatch strain in the nonlinear deformation range*, [Journal of the Mechanics and Physics of Solids](#) **48**, 1159 (2000).
- [25] S. Timoshenko, S. Woinowsky-Krieger, and S. Woinowsky, *Theory of plates and shells*, Vol. 2 (McGraw-hill New York, 1959).
- [26] J. Park, I. C. Kim, J. Cha, S. Park, J. Lee, and B. Kim, *Mechanotransduction of cardiomyocytes interacting with a thin membrane transducer*, [Journal of Micromechanics and Microengineering](#) **17**, 1162 (2007).

8

ELECTROSTATIC INSTABILITY: A MECHANISM FOR SURFACE STRESS SENSING

In this chapter, we briefly study the stability of the capacitive surface stress sensor as discussed in Chapter 7. In particular, the sensitivity of the electrostatic instability of a clamped circular plate to a change in its surface stress is studied and the effect of a differential pressure on this sensitivity is investigated. This study shows that limit voltages of an electrically loaded clamped plate are highly sensitive to a change in surface-stress and this sensitivity can be further improved by pressurizing the plate and by optimizing the size of the functionalized area. This suggests the suitability of a pressurized clamped plate or membrane with electrostatic instability as the readout mechanism for surface-stress based measurements.

8.1. INTRODUCTION

Surface stress based measurement is a relatively new mechanism in biological and chemical molecular detection. The principle is based on molecular adsorption on one side of a plate or cantilever. As a consequence, the surface stress of the component changes and the component deforms [1, 2]. The deflection of the system can be measured and used to estimate the surface stress [3, 4].

The pull-in instability, has been shown to be a sensitive readout technique for surface stress measurements [5–7]. For such measurements, the sensor is basically designed as a simple parallel plate capacitor using one flexible electrode as the sensing component. When an electric potential is applied to the capacitor, an attractive electrostatic load is induced between its electrodes. At a critical voltage the stiffness of the structure in transverse direction vanishes and the system becomes unstable and pull-in occurs. The pull-in voltage of a capacitor is influenced by the initial distance between the electrodes and stiffness of the flexible component, both of which are affected by a deflection due to a change in surface stress of the system. Therefore, a change in surface stress directly leads to a change in the limit voltage of the sensor.

In this chapter, we briefly study the sensitivity of the electrostatic instability of a clamped micro-plate as a readout mechanism for surface stress based measurements. For this purpose, a simplified model of a surface stress sensor, similar to Chapter 7, is considered. A circular membrane is assumed as the sensing component, while only a smaller circular area of its surface is subjected to changes in surface stress. A discretized model of such a sensor is built, and finite element method is used to study the sensitivity of the critical voltage of the membrane to the changes in surface stress. Then the optimized radius of functionalized area (i.e. the area loaded with surface stress) to maximize this sensitivity will be calculated.

In addition, the effect of applying a differential pressure on the flexible electrode on the sensitivity is studied. As mentioned in Chapter 2, a differential pressure leads to a significant change in pull-in behavior of the system. As a result, the system exhibits a primary limit point which leads to a snapping behavior, before the ultimate pull-in occurs. The sensitivity of both critical voltages to a change in surface stress is studied for different differential pressures and different radii of the functionalized area. The results of this study suggest that the electrostatic instability of a clamped plate is highly sensitive to surface stress and the size of the functionalized area can significantly affect this sensitivity.

8.2. METHODOLOGY

In order to study the sensitivity of critical voltage of a membrane sensor to surface stress changes, a simplified model of a capacitive surface stress sensor is considered. The model of the sensor consists of a circular conductive plate, fully clamped along its circumference. A part of the membrane surface is coated with a thin layer of gold. This gold layer is functionalized to adsorb the target molecules and thus, it represents the functionalized area. The membrane is suspended over a grounded electrode and the initial distance between the electrodes is d . A differential pressure P and an elec-

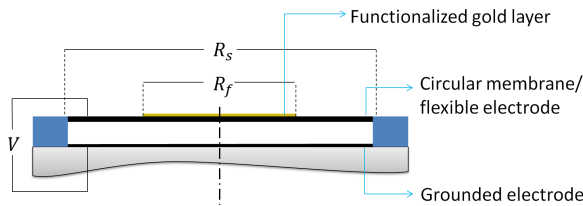


Figure 8.1: The conceptual design of a surface stress sensor with a clamped plate as the flexible electrode and sensing component.

tric potential V are applied to the membrane. This conceptual design is graphically shown in Figure 8.1.

The commercial finite element software COMSOL [8] has been used to model the electrostatics and mechanics of such a system. The material properties and specifications employed in the finite element model are given in Table 8.1. The details of the model can be found in Section 7.4.

Table 8.1: Model parameters

	Membrane	Functionalized film	Gap
Material	doped Silicon	Gold	Air
Elasticity Modulus	169 GPa	80 GPa	
Poisson ratio	0.2	0.3	
Radius	$R_s=125 \mu\text{m}$	R_f	
Thickness	$0.5 \mu\text{m}$	$0.025 \mu\text{m}$	$d = 2 \mu\text{m}$
Relative Permittivity	11.68	1	1.006

In order to calculate the equilibrium path for this structure, the differential pressure and *average* deflections of the plate are prescribed. Then, the required electric potential to maintain the equilibrium of the plate in such a configuration is calculated. To solve the highly nonlinear equations, the Newton method was employed. This calculation is repeated over a range of average deflections and as a result, the equilibrium path of the system is achieved. The critical voltages can be found by tracing the limits of the electric potential.

To model the effects of the surface stress, a compressive stress resultant of 10 N/m , which is typical of biological reactions, is applied on the thin layer of gold, and the simulations are repeated. The simulations are repeated for different radii of the thin film and different differential pressures. As a result, the optimized radius of the functionalized area to maximize the sensitivity of the sensor can be obtained.

8.3. RESULTS AND DISCUSSION

In this section, the results of the proposed finite element model are discussed and the sensitivity of the critical voltages of the membrane sensor to surface stress changes

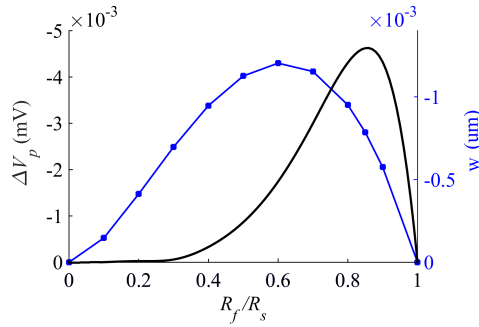


Figure 8.2: The change in pull in voltage (ΔV_p) and the deflection of the membrane (w) due to a 0.01 N/m change in surface stress as a function of the normalized radius of the functionalized area $\frac{R_f}{R_s}$.

is investigated. First, we consider a case where no differential pressure is applied to the system (i.e. $P=0$). In this case the equilibrium solution has only one limit point (pull-in) and the critical voltage at this limit point is $V_p = 15.5 \text{ V}$. By applying the surface stress, the flexible electrode deforms and consequently, the critical voltage and deflection at this limit point slightly decrease. Figure 8.2 shows the change of pull-in voltage (ΔV_p) due to a 0.01 N/m change in surface stress in its functionalized area. The deflection in the center of the membrane (w) is also shown in the this figure.

As it can be observed in Figure 8.2, if the functionalized area covers the whole surface of the membrane (i.e. $\frac{R_f}{R_s} = 1$), the deflection of the membrane due to surface stress changes is zero. Furthermore, there is an optimum radius of the functionalized area which leads to the maximum deflection of the sensor. This optimum radius depends on the materials and geometry of the sensor, as well as the surface stress changes.

It should be noticed that the maximum sensitivity of pull-in voltage does not necessarily coincide with the maximum deflection. For instance, for the model de-

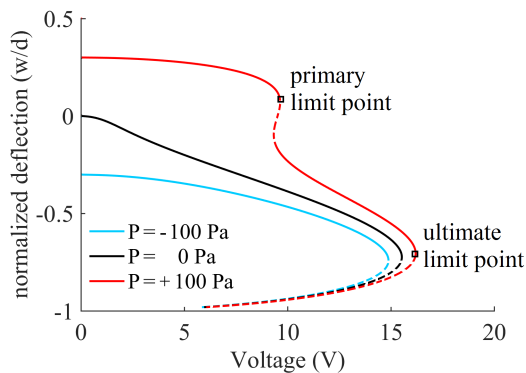


Figure 8.3: The deflection of the membrane as a function of the applied voltage. Pressurizing the micro-membrane leads to emergence of more limit points in the equilibrium solution of the system.

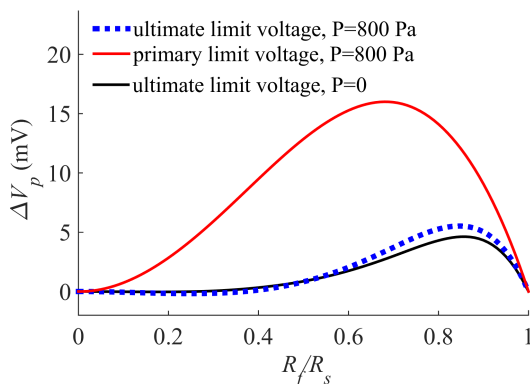


Figure 8.4: The change of the primary and ultimate limit voltages (ΔV_p) to a 0.01 N/m change in surface stress as a function of the normalized radius of the functionalized area R_f .

scribed here, the radius of the functionalized area to create the maximum deflection is $R_f/R_s = 0.6$ and the optimum radius to create the maximum change in the pull-in voltage is $R_f/R_s = 0.85$.

Next, the effect of pressurizing the sensor on its sensitivity is studied. As mentioned before, if a differential pressure (in opposing direction of the electrostatic load) is applied on the membrane, the system might exhibit new limit points in its equilibrium solution (see Figure 8.3); one critical point is close to the limit point in an unloaded system, only at a slightly different voltage and deflection. We refer to this point as the ultimate limit point. The other critical point occurs earlier, and it only happens if the pressure is higher than a certain amount. We refer to this point as the primary limit point. These limit points and the threshold of their existence have been extensively discussed in Chapter 2.

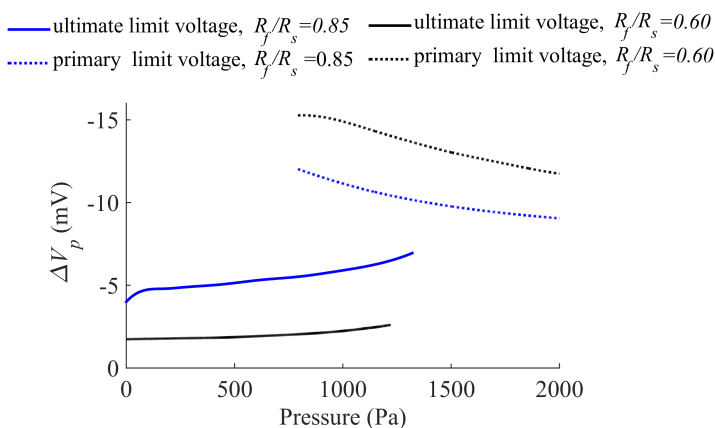


Figure 8.5: The change of the critical voltages of the system due to a 0.01 N/m change in surface stress as a function of the applied pressure, for two different radii of functionalized area.

The observed primary limit voltage is highly sensitive to surface stress changes in the functionalized area. Moreover, the sensitivity of the primary limit and ultimate pull-in voltage to the surface stress changes are functions of the size of the functionalized area, as well as the applied differential pressure. The changes of primary and ultimate limit voltage of the system, due to the change in surface stress on functionalized area, are shown in Figure 8.4. For comparison, the change of the limit voltage for two cases (i.e. when $P=0$ and $P=800$ Pa) are included. As can be observed, applying a differential pressure slightly improves the maximum sensitivity of the ultimate limit voltage (at $R_f/R_s=0.85$). The primary limit voltage, however, appears to be significantly more sensitive to the surface stress changes as compared to the ultimate limit voltage. It should be noted that the optimum sensitivity for the test case at hand is more than 15 mV for 0.01 N/m change in the surface stress.

Figure 8.5 shows the change of the critical voltages as a function of the applied pressure. This figure is obtained for two cases, namely $R_f/R_s = 0.6$ and $R_f/R_s = 0.85$. As can be observed, the sensitivity of the pull-in voltage can be improved by applying a positive pressure. The sensitivity of the primary limit voltage is generally higher than the sensitivity of pull-in voltage. However, this sensitivity decreases monotonically with the pressure. Therefore, the optimum pressure to maximize the sensitivity is the minimum pressure which allows for occurrence of the primary limit point.

8.4. CONCLUSIONS

A finite element analysis was performed to study the sensitivity of the electrostatic instability of a membrane based capacitive sensor to the surface stress changes. The electrostatic instability has been shown to be a sensitive readout mechanism for surface stress-based measurements. The sensitivity of the critical voltages to surface stress depends on the size of functionalized area. Hence, this size can be optimized to maximize this sensitivity.

In addition, it was shown that applying a differential pressure on the micro-membrane allows for observation of a so-called primary limit point which is significantly more sensitive to surface stress changes. As the results of this study indicate, an optimization of two design parameters, namely, the pressure and the size of the functionalized area, can remarkably improve the sensitivity.

REFERENCES

- [1] R. Raiteri, M. Grattarola, H.-J. Butt, and P. Skládal, *Micromechanical cantilever-based biosensors*, [Sensors and Actuators B: Chemical](#) **79**, 115 (2001).
- [2] J. Tamayo, A. Humphris, A. Malloy, and M. Miles, *Chemical sensors and biosensors in liquid environment based on microcantilevers with amplified quality factor*, [Ultramicroscopy](#) **86**, 167 (2001).
- [3] V. Tsouti, C. Boutopoulos, I. Zergioti, and S. Chatzandroulis, *Capacitive microsystems for biological sensing*, [Biosensors and Bioelectronics](#) **27**, 1 (2011).
- [4] A. Jain, P. R. Nair, and M. A. Alam, *Flexure-fet biosensor to break the fundamental sensitivity limits of nanobiosensors using nonlinear electromechanical coupling*, *Proceedings of the National Academy of Sciences* **109**, 9304 (2012).
- [5] M. Khater, *Use of instabilities in electrostatic micro-electro-mechanical systems for actuation and sensing*, Thesis (2011).
- [6] J. Sharma and A. Dasgupta, *Effect of stress on the pull-in voltage of membranes for mems application*, [Journal of Micromechanics and Microengineering](#) **19**, 115021 (2009).
- [7] H. Sadeghian, H. Goosen, A. Bossche, and F. van Keulen, *Application of electrostatic pull-in instability on sensing adsorbate stiffness in nanomechanical resonators*, [Thin Solid Films](#) **518**, 5018 (2010).
- [8] *Comsol multiphysics user guide (version 4.3 a)*, (2012).

9

OVERVIEW, CONCLUSIONS AND RECOMMENDATIONS

In this chapter, a brief summary and relevant conclusions arising from the performed research are presented. Moreover, some reflections on the limitations of the chosen approaches and recommendations for continuation of this research are provided.

9.1. OVERVIEW AND CONCLUSIONS

The main aim of this research was to provide theoretical techniques to study and characterize the mechanical performance and stability of micro-plates in electrostatic MEMS devices. The provided techniques allow us to investigate the mechanical behavior minutely, which is paramount for improving the performance of associated MEMS devices, as well as development of MEMS with new application.

For this purpose, first, the nonlinear mechanics and stability of a micro-plate in interaction with an electrostatic field has been investigated in Chapter 2. An analytical solution has been proposed to approximate the deformation, the pull-in voltage and the critical deflection of the flexible electrode. The proposed method is simple and computationally inexpensive and still, provides very good agreement with equivalent detailed finite elements solutions.

The results of this study suggests that the nonlinear geometrical stiffness of a clamped micro-plate —often referred to as membrane effect— plays an important roll in its nonlinear response to an applied electric potential. Hence, the pull-in voltage and deflection obtained by a conventional engineering solution (which is typically based on parallel plate electrodes with a linear spring constant), is somewhat irrelevant for a real capacitor with clamped electrodes. Nevertheless, when no compressive in-plane stress emerges in the system, the results of the engineering model are often highly conservative and safe to be used for design.

The effect of a differential pressure on the stability of a clamped micro plate in interaction with an electrostatic field has been addressed in Chapter 2. The results of this study indicate that in presence of a differential pressure, the flexible electrode is prompted to exhibit a primary instability and a snapping behavior, before electrostatic pull-in occurs. As a matter of fact, the pressure can cause additional limit points and an unstable solution branch in the equilibrium solution of the system.

The newly observed critical point (which we refer to as primary limit point) is highly sensitive to the applied differential pressure. Thus, the possibility of employing the sensitivity of the limit voltage to pressure for sensing applications has been discussed, and particularly, two different methods for employing this limit point for pressure measurements have been suggested. Although electrostatic instability as a sensing mechanism does not allow for continuous sensing methods, using the primary limit point can benefit from the advantages of high sensitivity, robustness of pull-in measurements, and avoiding contact failure. In addition, still the device can be fabricated with standard flat electrodes.

The pressure range in which the primary limit point emerges in the solution can be calculated using the proposed method in Chapter 2. It is evident that when the micro-plate becomes unstable, right at the critical points, the stiffness of the system equals to zero. However, in a pressure range that the primary instability *does not* exist, still the combination of pressure and electrostatic load lead to a very low stiffness in the system. This phenomenon is, in particular, very appealing for sensing applications.

It should be mentioned that employing a system close to its unstable configuration makes it sensitive to imperfections. However, it has been shown that a small initial deflection (similar to plate's first two buckling modes) only leads to a shift in the

required range of pressure for existence of the primary instability and snap-through. If the initial deflection is relatively large, the micro-plate will behave bistable even if not loaded electrically.

Recall that in actuation applications, an AC voltage will be applied to the system, and therefore, the frequency and amplitude of this AC voltage will also influence the voltage and deflection of the limit points. In fact, other types of instabilities (rather than limit points) might emerge in the solution branches of the system. Hence, the nonlinear steady state response of an electrically actuated micro-plate and its stability have been studied in Chapters 3 and 4. A Lagrangian approach has been utilized to derive the approximate equation of motion. In order to investigate the branches of periodic solutions and detect instabilities, a pseudo arc-length continuation and collocation technique have been employed.

Based on the proposed scheme, the effects of load parameters, namely DC and AC driving voltages, the excitation frequency, and also differential pressure on the instability of the system have been explored. The proposed method is simple and computationally efficient and it allows for analysis of highly nonlinear settings, which would have been significantly expensive to investigate with any other computational method.

The results indicate that in presence of a differential pressure the steady state motion of an electrically actuated micro plate — similar to its equilibrium in static loading— can be bi-stable or even multi-stable. This, in first place, means that the response of the system depends on its initial conditions. Moreover, different sequences of loading lead to different instability mechanisms. Saddle-node and period doubling bifurcations were repeatedly observed in the results and therefore, are recognized as the main mechanisms of failure. In addition, it was found that in the presence of pressure, increasing the DC or AC voltages could surprisingly help to stabilize the motion of the micro-plate. This is while, in the absence of pressure, a higher voltage only can aggregate the stability.

Considering that NEMS are the ultimate miniaturization step from MEMS devices, we studied the possibility of analyzing nano-plates (with a thickness in the order of 10^{-9} m) within the framework of continuum mechanics. First, in order to examine the validity of the proposed model in Chapters 3 and 4, we employed a similar methodology to analyze the nonlinear vibration of an electrically actuated Graphene nano-resonator in Chapter 5. The method has been shown to be particularly beneficial for extracting the Young's modulus of the Graphene membrane.

In fact, the Young's modulus of a single layer Graphene is claimed to be 1.15TPa in literature. However, in the study performed in Chapter 5, the Young's modulus matching the theoretical results with the experiments is obtained 560GPa. If this Young's modulus is employed in the simulations, the effects of geometrical and electrostatic nonlinearities could be accurately captured by the proposed method. The mismatch between the expected Young's modulus and the experimental results might originate from the inherent imperfections in the Graphene membrane, such as ripples and wrinkles. The results of this study support the argument that these imperfections do not have any global effect on the first vibration modes. However, they can affect the overall Young's modulus of the material.

Next, we have briefly studied the possibility of capturing the scaling effects in

mechanical behavior of nano-plates by employing a *nonlocal* continuum theory. In particular, in Chapter 6, a model has been proposed for capturing the effects of thickness on the size-dependency of the mechanics of plates. A strong three dimensional nonlocal formulation has been employed, and the effect of thickness on the flexural rigidity and effective elastic modulus of the plate has been studied. Based on this research, two modification factors for the extensional and bending stiffness matrices were presented to account for the effect of thickness in the nonlocal elasticity formulations.

In nonlocal elasticity, as a consequence of including contributions of integrals of the strain field in the constitutive equations, additional boundary conditions are required. These boundary conditions define the shape of the nonlocal kernel at the boundaries. Although in literature, the solution given by a bounded kernel is suggested to provide the “correct” solution, there is no clear physical interpretation of the chosen boundary conditions. Presumably, these boundary conditions should reflect the surface material property of the structure. Therefore, the suitable boundary conditions for the nonlocal kernel shall be obtained using molecular dynamics simulations or other atomistic models.

Finally, in Chapters 7 and 8, the mechanical performance and instability of a micro-plate as a transducer in surface stress sensing have been investigated. A design has been presented for a membrane-based capacitive sensor for surface stress measurements. An analytical solution has been presented to calculate the mechanical response of such a sensor. Using this model, the optimum size of the functionalized area in order to create the maximum sensitivity can be found. Furthermore, using a finite element model, the effect of the shape and position of the agglomeration of target molecules on the ultimate response of these types of sensors have been investigated.

In fact, a uniform surface stress change does not induce any deflection in a fully clamped circular micro-plate. However, its deflection can be increased if a smaller area of its surface is subjected to the surface stress changes. Therefore, the relative size of the functionalized area has a significant influence on the sensitivity of the surface stress sensor. Based on the performed study, the maximum deflection of a circular micro-plate occurs when the radius of the functionalized area is 0.6 times the plate radius. In that case, the deflection is at least 22 percent of an equivalent cantilever with similar thickness and a length equal to the plate radius.

Notice that a clamped plate as a surface stress transducer has an advantageous insulating property in comparison to cantilevers, and therefore, it can benefit from capacitive read-out techniques in liquid environments. Although the deflection of a clamped plate is smaller than cantilevers, the high resolution of the capacitive measurements yields to *signal to noise ratio* comparable to—or even better than—cantilevers. The results of this study suggest that using the proposed optimized size of the functionalized area, the overall reliability of the capacitive surface stress sensors can be increased.

In Chapter 8, the electrostatic instability of a membrane-based capacitive sensor and its sensitivity to surface stress has been investigated. The electrostatic instability has been shown to be a promising readout mechanism for surface stress measurements. Particularly, when the micro-plate is loaded with a differential pressure, the

observed primary limit point is remarkably sensitive to the surface stress changes. Similar to the concept of employing electrostatic instability as a mechanism for pressure measurements, this system can benefit from the high sensitivity and robustness of pull-in measurements, and still avoids contact failure.

The techniques proposed in this thesis are simple and computationally efficient. They can provide in-depth insight into the problems and have made it possible to analyze some phenomena exhibited by micro-plates that were not feasible otherwise. The methodology and the results presented in this thesis can be useful to many MEMS settings with plate-like micromechanical components.

9.2. LIMITATIONS AND RESEARCH OUTLOOK

This thesis has provided some models for characterization of micro-plates in electrostatic MEMS devices. Evidently, all theoretical models, including those proposed here, rely on some simplifying assumptions which confine their competence. However, it has been nicely quoted by Henri Poincaré in another context: “Perhaps we ought to wait, and not look for a solution until have patiently assembled all the elements, but if we were so reasonable, if we were curious without impatience, it is probable we would never have created science and we would always have been content with a trivial existence [1].”

There are several aspects excluded in the present research, which might be of particular importance for the nonlinear behavior and stability of the device. A couple of these aspects which have not been investigated in this thesis and remain as open questions for future research projects are outlined here.

9.2.1. IMPERFECTIONS ANALYSIS

In fabrication processes of MEMS devices or during their operation, unexpected loadings or defects might emerge in the system which can influence the mechanics of the micro-component and ultimately affect the performance of the device. In this thesis, we have discussed the effect of a differential pressure and we have included a uniform in-plane residual stress in the models. However, some imperfections such as small holes or cracks, anisotropy of material, or non-uniform residual stress can all be influential to the nonlinear behavior of the component. For example, in the analysis in Chapter 2, a small defect can break the symmetry and therefore, the proposed mode shapes to describe the displacement fields need to be adapted to account for those a-symmetric shapes. In dynamic analysis in Chapters 3 and 4, a defect changes the resonance frequencies of the plate, which, in turn, might result in internal resonance or other nonlinear effects. Studying the effects of defects and imperfections on nonlinear mechanics of micro plates is an interesting research topic by its own.

Furthermore, at small scales, imperfections such as cracks, holes or slight ripples can affect the effective material properties of the component. Earlier in this chapter, in the discussion on the nonlinear dynamics of Graphene resonators, we mentioned the hypothesis of the effect of imperfections on the Graphene material properties. As a matter of fact, if such hypothesis holds, it can be of great interest

in nondestructive identification of imperfections in Graphene membranes. A non-contact method for concurrent estimation of Young's modulus and imperfections of 2D nano-materials, by exploiting their nonlinear dynamics response is an interesting research topic which can be perused as a continuation of this research.

9.2.2. POST-INSTABILITY ANALYSIS

Another interesting research question arising from this thesis is the behavior of the micro-plates in electrostatic MEMS devices, after it reaches its critical configuration. In this study, the stable and unstable solution branches in steady state motion of the micro-plate have been discussed and based on that, the post-instability behavior of the plate has been determined. However, to study post-instability phenomena rigorously, a full transient analysis is required.

Using a transient analysis one can determine if during the snapping the symmetry of the system breaks, or, if a period doubling bifurcation leads to a chaos. It should be noticed that such analysis is strongly influenced by the imperfections. A transient analysis can be particularly important in design of actuators. As a matter of fact, the actuator can be designed in a way so that chaos is avoided in its operating frequency range. Furthermore, this transient analysis is required for designing a feedback controller for the actuator.

9.2.3. EXPERIMENTAL VERIFICATION

The present study has been mainly focused on analytical and computational methods. In order to employ these methods in engineering applications and design, the validity of their results needs to be evaluated and calibrated by experiments. In Chapters 5 and 6, comparisons were made with experimental results. However, the discussion on stability of micro-plates in interaction with electric fields remains to be verified experimentally. Without further research into experimental stability calibration, and verification of bi-stable behavior of flat micro-plates, it will not be possible to employ the proposed results in practice.

9

It is the author's opinion, however, that the theoretical solutions are not only to solve one existing problem, but also to present an in-depth insight, letting the scientist to dream and then, to make those dreams happen in practice.

REFERENCES

- [1] F. Verhulst, *Henri Poincaré: impatient genius* (Springer Science and Business Media, 2012).

CURRICULUM VITÆ

Banafsheh SAJADI

06-04-1985 Born in Tehran, Iran.

EDUCATION

- 2017–2018 Postdoc in Dept. Precision and Microsystems Engineering
Delft University of Technology, Delft, The Netherlands
Project: Nonlinear Identification of Two-Dimensional Materials
via Reduced Order Modeling
Supervisors: Prof. dr. P. Steeneken, Dr. F. Alijani
- 2013–2017 PhD in Dept. Precision and Microsystems Engineering
Delft University of Technology, Delft, The Netherlands
Thesis: On the Mechanics and Stability of Micro-Plates in
Electrically Loaded MEMS Devices
Supervisors: Prof. dr. F. van Keulen, Dr. J.F.L. Goosen
- 2008–2011 Postgraduate in the major of Applied Mechanics
Sharif University of Technology, Tehran, Iran
Thesis: Experimental and Theoretical Investigation on
Elasto-plastic Behavior of Glass Fiber Reinforced Composites
Supervisors: Prof. dr. R. Naghdabadi, Dr. M. Asghari
- 2003–2007 Undergraduate in the major of Mechanical Engineering
Sharif University of Technology, Tehran, Iran
Thesis: Dynamics of Fullerene in Carbon Nano-tubes
Supervisor: Prof. dr. R. Naghdabadi

LIST OF PUBLICATIONS

JOURNAL PUBLICATIONS

1. **B. Sajadi**, F. Alijani, D. Davidovikj, J.F.L Goosen, P. G. Steeneken, F. van Keulen, *Experimental Characterization of Graphene by Electrostatic Resonance Frequency Tuning*, Accepted in Journal of Applied Physics. (from this thesis)
2. **B. Sajadi**, F. Alijani, J.F.L Goosen, F. van Keulen, *Effect of Pressure on Nonlinear Dynamics and Instability of Electrically Actuated Circular Micro-Plates*, Submitted to Journal of Nonlinear Dynamics. (from this thesis)
3. **B. Sajadi**, J.F.L Goosen, F. van Keulen, *Effects of Pressure on Electrostatic Instability of Micro-Plates: A Semi-Analytical Approach*, Submitted to International Journal of Mechanical Sciences. (from this thesis)
4. **B. Sajadi**, J.F.L Goosen, F. van Keulen, *Bi-stability of Micro-plates: A Sensitive Mechanism for Differential Pressure Measurements*, [Applied Physics Letters VOL. 111, \(2017\)](#). (from this thesis)
5. **B. Sajadi**, J.F.L Goosen, F. van Keulen, *Capturing the effect of thickness on size-dependent behavior of plates with nonlocal theory*, [IEEE Sensors Journal, VOL. 17, NO. 10 \(2017\)](#). (from this thesis)
6. **B. Sajadi**, J.F.L Goosen, F. van Keulen, *Optimization of Capacitive Membrane Sensors for Surface-Stress Based Measurements*, [International Journal of Solids and Structures, VOL. 115–116 \(2017\)](#). (from this thesis)
7. S.M. Ahmadi, G. Campoli, S. Amin Yavari, **B. Sajadi**, R. Wauthle, J. Schrooten, H. Weinans, A.A. Zadpoor, *Mechanical behavior of regular open-cell porous bio-materials made of diamond lattice unit cells*, [Journal of the Mechanical Behavior of Biomedical Materials, VOL. 34, \(2014\)](#).

CONFERENCE PUBLICATIONS

1. **B. Sajadi**, F. Alijani, J.F.L Goosen, F. van Keulen, *Static and Dynamic Pull-In of Electrically Actuated Circular Micro-Membranes*, [ASME 2016 International Mechanical Engineering Congress and Exposition, Phoenix, Arizona, USA, November 11–17, 2016](#). (from this thesis)
2. **B. Sajadi**, J.F.L Goosen, F. van Keulen, *Membrane Based Surface-Stress Sensors: Sensitivity, Reliability, Precision and Accuracy*, Workshop on Nanomechanical Sensing, Delft, The Netherlands, June 22-24, 2016. (from this thesis)

3. **B. Sajadi**, J.F.L Goosen, F. van Keulen, *Pull-in Instability of Clamped Plates for Pressure Measurements*, Nanomechanical Sensing Workshop (NMC 2015), University of Auckland, Auckland, New Zealand, July 13-16, 2015. (from this thesis)
4. **B. Sajadi**, J.F.L Goosen, F. van Keulen, *Nonlocal Elasticity in Modifying Stoney's formulation*, 11th Annual International Workshop on Nanomechanical Sensing (NMC 2014), Madrid, May 2-4, 2014. (from this thesis)
5. **B. Sajadi**, R.Naghdabadi, M.Asghari, *Analytical study on elastic behavior of Glass fiber reinforced polypropylene with uni-directional alignment*, International Conference on Aerospace, Mechanical, Automotive and Materials Engineering (ICAMAME 2012), Zurich, Switzerland, January 15-17, 2012.
6. S.M. Ahmadi, E. Shirzad, **B. Sajadi**, M. Cheraghi, K. Haghghi, *An Experimental Study on the Kinematics of a Skilled Service in Playing Tennis*, [ASME 2010 International Mechanical Engineering Congress and Exposition, Vancouver, British Columbia, Canada, November 12–18, 2010](#).
7. **B. Sajadi**, R.Naghdabadi, *Dynamics of C_{60} inside Armchair Carbon Nanotubes*, International Congress on Nanoscience and Nanotechnology (ICNN2008), Tabriz, Iran, October 28-30, 2008.

ACKNOWLEDGEMENTS

Foremost, I would like to express my sincere gratitude to my supervisors, Dr. Hans Goosen and Prof. Fred van Keulen for their unsparing help and support to this project. My supervisors consistently allowed this thesis to be my own work, but steered me in the right the direction whenever I needed. Without their participation and input, this research could not have been successfully conducted.

Besides my supervisors, I would also like to thank Dr. Farbod Alijani for his help to my Ph.D. research, for his enthusiasm and passionate participation. Undoubtedly, his inspiration was a great motive for this research.

Moreover, I would like to thank the thesis committee, Prof. F J. Barthold, Prof. M. Amabili, Prof. P. J. French, and Prof. C. Bisagni, for spending a considerable amount of time reading this thesis and for their feedback.

Furthermore, I want to express special thanks to Prof. Peter Steeneken and Dejan Davidovikj for the nice collaboration and providing me with the results of their experimental research, and to Dr. Pierpaolo Belardinelli for helping me with the artwork of the cover of this book.

I would also like to thank my dear colleagues and my friends who made my work as a Ph.D. candidate a lot more enjoyable. They helped me to learn much about different topics in engineering, but also different cultures, different ways of friendship, and most interestingly, different meanings to life.

Finally, I must express my very profound gratitude to my husband, Mohammad, for his unsparing support through the process of researching and writing this thesis, and to my family for providing me with unfailing and continuous encouragement throughout my years of study. This accomplishment would not have been possible without them.

Thank you.

Banafsheh Sajadi